Next Generation Li-S and Li-O_2 Batteries based on Electrode and Electrolyte Design

by

Chun Yuen Kwok

A thesis

presented to the University of Waterloo

in fulfillment of the

thesis requirement for the degree of

Doctor of Philosophy

in

Chemistry (Nanotechnology)

Waterloo, Ontario, Canada, 2021

Examining Committee Membership

The following served on the Examining Committee for this Thesis. The decision of the Examining Committee is by majority vote.

Supervisor:	Linda Faye Nazar
	Professor, University of Waterloo
Internal Member:	Eric Prouzet
	Associate Professor, University of Waterloo
	Holger Kleinke
	Professor, University of Waterloo
	Vivek Maheshwari
	Associate Professor, University of Waterloo
Internal-External Member:	Michael Pope
	Associate Professor, University of Waterloo
External Examiner:	Xueliang Sun
	Professor, University of Western Ontario

Author's Declaration

I hereby declare that I am the sole author of this thesis. This is a true copy of the Thesis, including any required final revisions, as accepted by my examiners.

I understand that my thesis may be made electronically available to the public.

Abstract

Decoupling our reliance on fossil fuel as the primary energy source emphasizes battery technology to store intermittent renewable energy such as solar and wind for sectors including grid energy storage, electric transportation, and machine operation. In view of the limitation in the theoretical energy density presented by lithium-ion batteries, other electrochemical systems are being pursued. Li-S and Li-O_2 batteries are among the strong potential candidates. However, both battery systems are plagued by poor capacity retention, subpar Coulombic efficiency, low rate capabilities, and unsafe operation of lithium anode.

This dissertation document presents strategies to resolve some of the aforementioned problems, from the perspective of electrode and electrolyte design. Considerations of confining polysulfides and stabilizing the cathode architecture for Li-S batteries are discussed. A novel cell design on Li-O_2 batteries that leads to new oxygen electrochemistry is introduced. A new synthesis method to coat a solid-state electrolyte material as a protective layer on lithium metal is proposed. Projects presented in this thesis include:

1. *A holistic view in the fundamental surface mechanism and its correlation to the stability of Li-S cells.* As some metal oxide host materials are known to mediate sulfur conversion via the surface-bound thiosulfate/polythionate complexes, it is worth investigating the condition of the activation for such a process, which can serve as a guide for host material selection. It is revealed that the activation process is triggered by the redox potential of the host material that sits within a targeted window. It is further shown that the capacity retention in Li-S cells is directly correlated to this activation

process, demonstrated by long-term cycling experiments using high surface area oxide cathodes with redox potentials below, above, and within this window.

2. *Uncovering the complex surface chemistry in MXene to entrap polysulfides.* The interactions between MXene and polysulfides are revealed to be a two-step, dual process. Namely, the formation of thiosulfate/polythionate complexes arises from the consumption of surface hydroxyl group on MXene by polysulfides, followed by the reported Lewis acid-base interactions between the underlying Ti atoms and the remaining polysulfides in electrolyte. Carbon nanotubes are further incorporated between MXene layers to support high sulfur loading ($5.5\,\mathrm{mg{\cdot}cm^{-2}}$) Li-S cells by realizing a high-surface-area and conductive network within the cathode composite.

3. *Selecting an appropriate binder material to maintain the architectural integrity of high-loading sulfur cathodes.* Two cross-linked polymers may have very different cycling performances, despite their similarities in polysulfide adsorptivity. A key factor often overlooked is the compatibility between the monomer and cross-linker. Proper cross-linkages are necessary for binders to maintain good polysulfide binding effects and mechanical properties, evidenced by mechanical tests, microscopic images, deep cycling, and impedance studies on sulfur cathodes fabricated with these binders. The optimized cathode architecture enables Li-S cells to feature a low electrolyte/sulfur ratio of 7:1 (µL:mg) yet high areal capacity, up to $5.6\,\mathrm{mA{\cdot}h{\cdot}cm^{-2}}$, at a high sulfur loading of $6\,\mathrm{mg{\cdot}cm^{-2}}$.

4. *A new Li-O_2 battery design that enables a reversible four-electron conversion in oxygen electrochemistry.* By operating the cell at 150 °C and utilizing a bifunctional

metal oxide host that catalyzes O-O bond cleavage on discharge, an inorganic Li-O_2 cell can cycle via a highly reversible four-electron redox conversion that forms crystalline Li_2O as the discharge product. Extensive chemical quantification experiments confirmed that Li_2O oxidation involves a direct transfer of 4 e^-/O_2. A discharge mechanism is also proposed. This work shows that the Li-O_2 battery cycling stability is no longer intrinsically limited once problems revolving around electrolyte, (su)peroxides, and cathode hosts are overcome.

5. *A facile and scalable route for the in-situ formation of a Li anode protection layer.* Lithium phosphorus oxynitride - a class of solid-state electrolyte materials that forms a stable interface with lithium metal - is a promising candidate for protecting lithium anode. Its traditional synthesis route (atomic layer deposition), however, requires complex and stringent conditions. A new synthesis method via solution-mediated chemistry is introduced. The lithium phosphorus oxynitride layer prepared in-situ protects the lithium anode from polysulfide corrosion in practical Li-S cells, leading to an average Coulombic efficiency of at least 80 % without the aid of the conventional $LiNO_3$ electrolyte additive.

Acknowledgements

I would like to send my sincere gratitude to my supervisor and mentor, Dr. Linda Faye Nazar, for her support and guidance during my graduate study. It was a wonderful time to study, conduct research, and dig into the science with her. I have learned how to think, propose and present ideas, execute experimental plans, and write scientifically from her. I would also like to thank Dr. Xiao Liang, Dr. Chun Xia, Dr. Quanquan Pang for their help and guidance in my early career. Extending my gratitude to my Ph.D. committee: Dr. Eric Prouzet, Dr. Holger Kleinke, and Dr. Vivek Maheshwari for their help and guidance on my research, and to Dr. Michael Pope and Dr. Xueliang Sun for being my internal-external member and external examiner, respectively. Their time to participate in my thesis defence is much appreciated.

Aside from my committee members, I want to thank my colleagues in Prof. Nazar's Research Group. Members include Laidong, Andrew, Xiaoqi, Shiqi, Marcus, Ivan, Abhi, Se Young, Marine, Connor, Jaka, Diane, Victor, Momo, Brain, Robert, Russel, He, Elahe, Yverick, Dipan, Guang, Partick, Fabien, Chan Sun, Kern Ho, Zhizhen, Shahrzad, Erika, Ali, Chang, Kavish, Guerman, Lauren,

Furthermore, I would like to thank my mother and father, for bringing me up and supporting me through my studies and life. Together with my lovely sister (Mandy) and my 4^{th} aunt (Kitty) and uncle (Ray) who have always been there for me. Furthermore, I would also like to thank my two best buddies, Dr. Joshua Tyler Cantin and Wing Hong Wong. I would not have been able to complete my Ph.D. degree without all of your help in keeping my sanity together.

Of course, the most important person that I need to thank is my wonderful, beautiful, cute, and smart wife, Gillian, for everything that you have done in the past 6 years. Your love and patience have enabled me to get through many difficulties.

Dedication

This thesis is dedicated to my wife and my two annoying but lovely cats, Dango and Pocky.

MEOW

Table of Contents

List of Tables

List of Figures

List of Abbreviations

AETMAC [2-(acryloyloxy)ethyl] trimethylammonium chloride

AIBN Azobisisobutyronitrile

ALD Atomic layer deposition

ASR Areal specific resistance

BET Brunauer-Emmett-Teller

CE Columbic efficiency

CNF Carbon nanofiber

CNT Carbon nanotube

CV Cyclic voltammetry

DADMAC Diallyldimethylammonium chloride

DEMS Differential electrochemical mass spectrometry

DME 1,2-Dimethoxyethane

DMF dimethylformamide

DMSO Dimethyl sulfoxide

DOL 1,3-Dioxolane

EDX Energy dispersive x-ray spectroscopy

EGDA Ethylene glycol diacrylate

EIS Electrochemical impedance spectroscopy

FTIR Fourier-transform infrared spectroscopy

FWHM Full width half maximum

GC Gas chromatography

HRTEM High-resolution transmission electron microscopy

LAGP Lithium aluminum germanium phosphate

LIB Lithium-ion battery

LiPON Lithium phosphorus oxynitride

LiTFSI Lithium bis(trifluoromethanesulfonyl)imide

MS Mass-spectrometry

OCV Open circuit voltage

OER Oxygen evolution reaction

ORR Oxygen reduction reaction

PHCS Porous hollow carbon sphere

PVDF Poly(vinylidene fluoride)

SEI Solid electrolyte interphase

SEM Scanning electron microscopy

SSE Solid state electrolyte

TEM Transmission electron microscopy

TGA Thermal gravimetric analysis

THF Tetrahydrofuran

XANES X-ray absorption near-edge structure

XPS X-ray photoelectron spectroscopy

XRD X-ray diffraction

Chapter 1

Introduction

1.1 Battery as Energy Storage Device

One of the fundamental laws in the natural world is that energy cannot be created or destroyed, it can only be transferred or converted from one form to another. From the time where humans first harvested energy using fire to keep us warm few million years ago to today where we send spacecrafts to the universes for exploration purposes, the sources of the energy that enable us to do these works remain unchanged and are still fairly limited.[1] That is, chemical energy stored in materials, for example, fossil fuels. By harvesting the chemical energy stored in the bonds in these substances, we obtain mechanical or electrical energy to do work.

While there is absolutely no argument that fossil fuel is our primary energy source today - World Bank estimates fossil fuel accounts for 80 % of the world energy consumption - its greenhouse gases emissions pose a great threat to our environment and

health.[2] A recent report released by the Intergovernmental Panel on Climate Change, United Nation explicitly states that the global temperature could only be stabilized in the next few decades if there are immediate, rapid, and large-scale reductions in greenhouse gas emissions.[3] A fossil fuel-based economy and society is clearly not sustainable. With increasing demands on alternative energy sources such as solar and wind, technologies to convert these renewable energy sources to electricity are hence under intensive developments.[4] However, energy storage technologies that offer high energy and power densities and long service life are required to store these intermittent sources for future use. Rechargeable batteries have conquered in this particular landscape due to easy installation and pollution-free operation. Many rechargeable battery systems, such as lead-acid, nickel-cadmium, nickel-metal hydride, and lithium ion batteries (LIBs), have already served various terrains in the modern human society.[4]

Rechargeable battery is a device that can reversibly convert chemical energy to electrical energy through a controlled redox chemical reaction. In general, a battery consists of two materials that are of different chemical potential energies. The material with higher chemical potential energy is referred to as the positive electrode material (P) whereas the lower one is referred as the negative electrode material (N). As shown in **Figure 1.1**, the two electrodes are separated by an ionic conductive medium called electrolyte, and an electrical insulating material called separator. During battery discharge, the negative electrode material donates an electron (e^-) and a metal cation (M^+, M = Li), serving as the anode. As the metal cation migrates to the positive electrode through the electrolyte under an electrical field, the electron also heads to the same destination through an external circuit to provide electricity. The positive electrode that accepts the

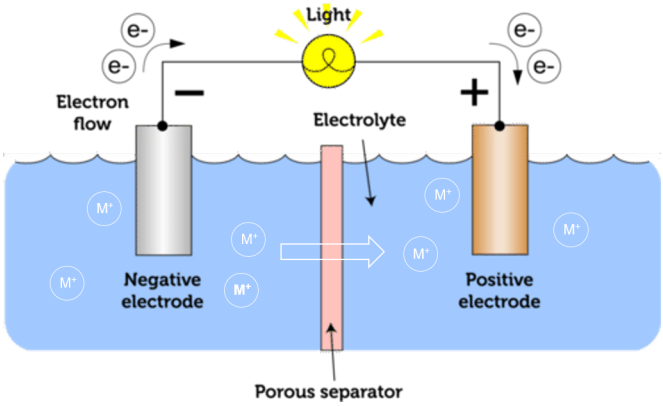

Figure 1.1. Schematic of a battery. Modified from [5].

Li^+/e^- pair is the cathode. The reverse process takes place during charge. The terms positive electrode and cathode will be interchangeably used in this thesis; the same applies to negative electrode and anode. This is to avoid confusion in the nomenclature change between discharge and charge state. The half reactions on discharge are shown in **Equations 1.1** and **1.2**, and the redox state of these substances are labeled in the subscript:

$$\text{Cathode: } P_{ox} + ne^- + nLi^+ \rightarrow P_{red} \tag{1.1}$$

$$\text{Anode: } N_{red} \rightarrow ne^- + nLi^+ + N_{ox} \tag{1.2}$$

which gives rise to the net equation:

$$\text{Net: } P_{ox} + N_{red} \rightarrow P_{red} + N_{ox} \tag{1.3}$$

1.2 Charge Storage Mechanism in Battery

Intercalation and conversion mechanism are the two main methods in battery to store charge (Li^+) in the active material. The electrode material functions as host material to hold the lithium ions in intercalation mechanism, whereas the active material in conversion undergoes a phase transformation during redox.

Intercalation Mechanism

The most acknowledged battery system that follows intercalation mechanism is the Li-ion battery (LIB) whose design is based on a lithium transition metal oxide ($LiCoO_2$ for example) cathode coupled with a graphite anode.[6] As shown in **Figure 1.2A**, lithium ions travel between the two electrode materials during battery operation, much like a *rocking-chair* and hence the nickname. Charging of the cell leads to delithiation of $LiCoO_2$ material as Co^{3+} oxidizes to Co^{4+}. The carbon atoms in the graphite anode is lithiated upon receiving the Li^+/e^- pair. Discharging the cell reverses the aforementioned process. Hence the term *Li-ion* is a reflection of the fact that Li^+, not Li metal, is involved during electrochemical processes (**Equation 1.4**):

$$LiCoO_2 + 6C \rightleftharpoons Li_{1-x}CoO_2 + Li_xC_6 \qquad 1.4$$

Because there is no structural transformation to the active material ($LiCoO_2$ and graphite) during cell operations, these rocking-chair batteries have a long cycle life and low maintenance cost; earning their reputations as the leading technology in the personal

electronics, transportation, and grid energy storage sectors.[6, 7] However, the intrinsic single ion storage mechanism in combination with the high molecular weight in these transitional metal oxide hosts limit the theoretical specific capacity of these LIBs to $\sim$150 mA·h·g^{-1}. As a result, despite their high cell potential of 3.5 V, low specific energy is obtained.[7]

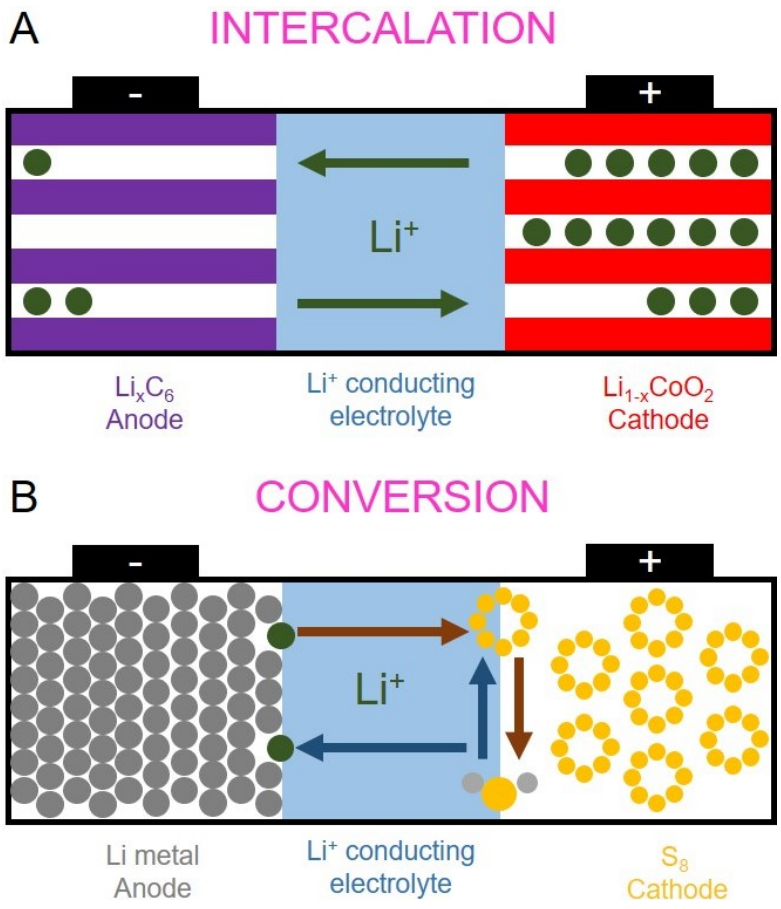

Figure 1.2. Charge storage mechanisms in battery. (A) Li-ion batteries represent intercalation mechanism and (B) Li-S batteries represent conversion. In intercalation mechanism, Li-ion are inserted/withdrawn into a layered structure material whereas conversion chemistry involves the active material transforming to a different phase in redox.

Conversion Mechanism

With the ever-increasing sophistication in portable electronics and demands for longer mileage in electrical vehicles, post LIB technologies that offer higher energy densities are required. The lesson learnt from the development in lithium ion battery technology is that any further large increase in energy density should be achieved through invoking higher ion/electron storage per active material mass, and not cell voltage. In particular, those based on conversion mechanism such as sulfur (Li-S) and oxygen (Li-O_2) electrochemistries show great potentials because of their low molecular weight.[8] However, (de)lithation of these materials changes their phase entirely. For example, in Li-S battery, elemental sulfur (α-S_8) adopts an orthorhombic structure, and the crystal structure of its discharge product (Li_2S) is a cube (**Figure 1.2B**).

Table 1.1 compares the theoretical gravimetric and volumetric energy densities of Li-S and Li-O_2 batteries to other popular electrochemical storage systems, showcasing their advantages. The focus of this thesis is the development of these two battery systems from the aspect of electrode and electrolyte design. The history, current status, and challenges for these batteries will be discussed in the following sections.

Table 1.1. Comparison of the theoretical gravimetric and volumetric energy densities of commercial and in-development battery technologies.

System	**Gravimetric** [$W{\cdot}h{\cdot}kg^{-1}$]	**Volumetric** [$W{\cdot}h{\cdot}L^{-1}$]
Li-S	2500	5200
Li-O_2	3500	6200
C_6-$LiCoO_2$	400	1140
MH-NiOOH	100	430
Pb-PbO_2	170	380

1.3 Li-S Battery

Li-S battery exploits lithium oxidation at the anode and sulfur reduction at the cathode to induce a current on discharge (**Figure 1.3A**). Separating the two electrodes is conventionally a polypropylene separator (Celgard) and a Li^+ conducting electrolyte comprised of 1 M lithium bis(trifluoromethanesulfonyl)imide (LiTFSI) and 2 wt. % $LiNO_3$ dissolved in an equivolume of 1-2,dimethoxyethane (DME) and 1,3-dioxolane (DOL).[9]

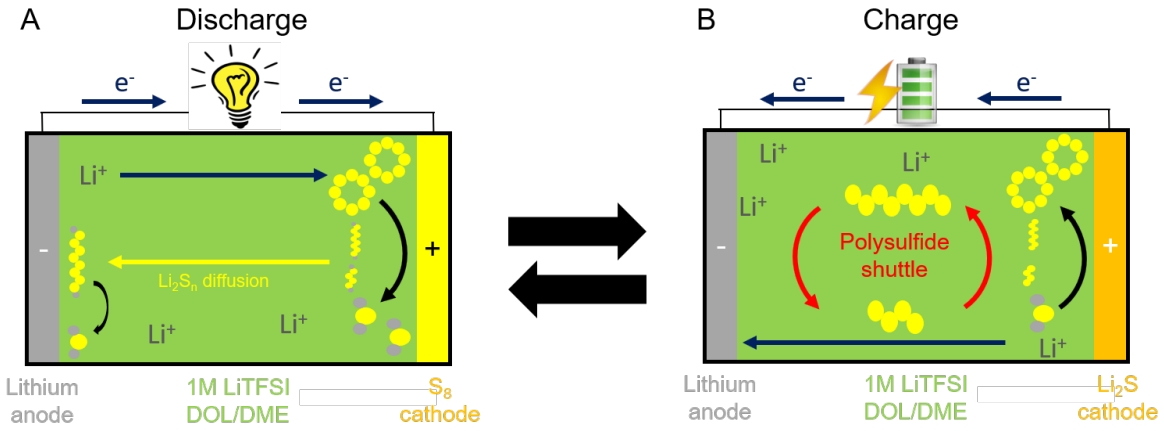

Figure 1.3. Li-S battery based on polysulfide dissolution-precipitation chemistry. (A) Diffusion of polysulfide to anode results in anode corrosion and material loss during discharge. (B) Redox shuttling of polysulfide between cathode and anodes gives rise to poor Coulombic efficiency and precipitation of Li_2S at the exterior of cathode/anode surface.

In Li-S chemistry, the reversible conversion of 16-electron per octasulfur molecule (α-S_8, or 2 electrons per S atom) to form Li_2S results in a cell potential and theoretical

capacity of 2.2 V *vs.* Li/Li^+ and 1675 $mA{\cdot}h{\cdot}g^{-1}$, respectively (1.5):

$$16Li^+ + S_8 + 16e^- \rightleftharpoons 8Li_2S \qquad 1.5$$

However, just as outstanding as the energy density that the Li-S electrochemistry presents (2500 $W{\cdot}h{\cdot}kg^{-1}$), there are several challenges unique to this battery system.[10, 11] Li-S battery is plagued by a convoluted and notorious phenomenon, known as polysulfide shuttle, that found its origin in the formation and diffusion of sulfur redox intermediate species called lithium polysulfides (Li_2S_n, $2 \leq n \leq 8$).[9, 12] Sulfur reduction pathway in DOL/DME involves a two-step process. Lithation of octasulfur results in the formation of high-order Li_2S_n ($4 < n \leq 8$) that are soluble in the ether-based electrolyte, featuring a discharge plateau at 2.3 V. This is supported by the work of Cuisinier *et al.* on probing the sulfur speciation in Li-S battery with respective to its electrochemical profile using operando X-ray absorption near-edge structure (XANES, **Figure 1.4**).[13] In the work, the weight component of each sulfur components (S_8, S_4^{2-}, S_6^{2-}, and Li_2S) was fitted using linear combination fit, and the evolution of polysulfides during the course of (dis)charge is shown in the upper panels of the figure.

The formation of high-order polysulfide is evidenced by detecting the signals that correspond to hexasulfide (S_6^{2-}) and tetrasulfude (S_4^{2-}). As discharge continues, the conversion from S_8 into high-order Li_2S_n ends at a supersaturation point; Li_2S then slowly precipitates out of solution from the low-order lithium polysulfides (Li_2S_n, $2 < x \leq 4$) with a second discharge plateau of 2.1 V (**left panel**, **Figure 1.4**). Li_2S is monotonically consumed and converted back to S_8 via the transformation of the soluble

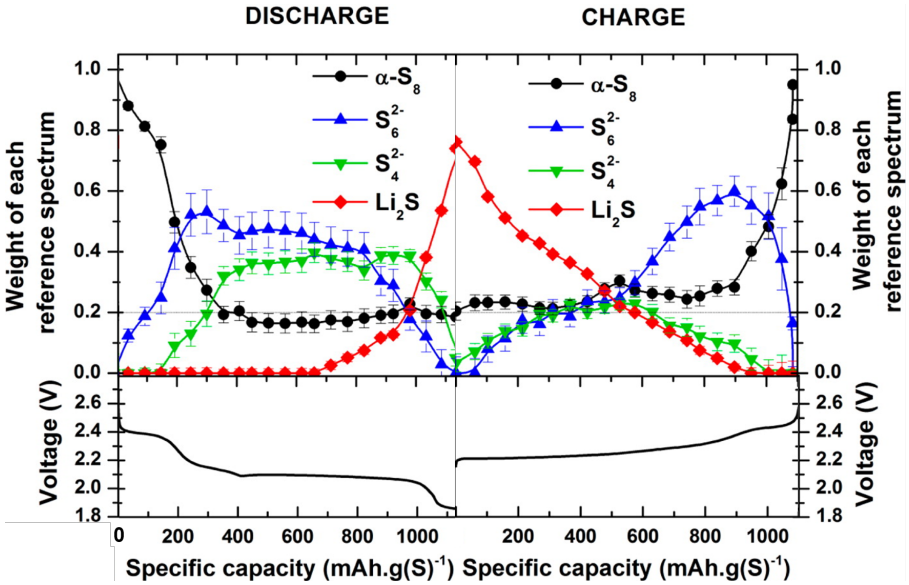

Figure 1.4. Li-S battery redox mechanism. Typical electrochemical profile of a Li-S battery (bottom panels) and its corresponding evolution of sulfur species (S_8, S_4^{2-}, S_6^{2-}, and Li_2S upon discharge (left) and charge (right) at C/10 rate. The top panel shows the linear combination fit for various sulfur species during the course of sulfur redox. Modified from [13].

tetra- and hexasulfides upon charge (**Figure 1.3B** and **right panel**, **Figure 1.4**).

The polysulfide dissolution-precipitation chemistry that enables the current Li-S battery to function is a double-edged sword. These soluble intermediate sulfur species serve as redox mediators to drive their own electrochemical reaction.[14, 15] However, they are highly toxic for cell cyclability because of polysulfide shuttle.[16] Since polysulfides are soluble in glyme, some of these materials can diffuse out of the cathode, migrate to the anode where they are reduced by Li metal to form low-order Li_2S_n (**Figure 1.3A**). The consumption of polysulfide by Li draws additional redox intermediate species (Li_2S_n) into the electrolyte and onto the anode surface. However, the polysulfide concentration gradient between the two electrodes causes some of the Li_2S_n in the electrolyte to diffuse

back to the cathode (**Figure 1.3B**) and are oxidized to long-chain of polysulfides again during charge. This repeating parasitic process, called polysulfide shuttle, continuously occurs in the cell unless polysulfides are properly confined at the cathode. As polysulfide shuttle is driven by the polysulfide concentration gradient between the two electrodes, the most direct consequences include (a) self-discharge and rapid capacity fading; (b) undesired cathode/anode surface passivation due to uncontrolled deposition of discharge products that originate from this unique dissolution-precipitation chemistry; and (c) infinite charge in extreme cases.[16]

Other issues residing the sulfur cathode include the 80 % volume change in the cathode due to the large density difference between sulfur and lithium sulfide ($\rho_{S} = 2.06$ *vs.* $\rho_{Li_2S} = 1.66$ g·cm^{-3}), as well as their electrical insulating nature ($\sigma_{e^-,\,S} = 5 \times 10^{-30}$ & $\sigma_{e^-,\,Li_2S} = 1 \times 10^{-14}$ S·cm^{-1}).[17] The combination of these issues are known to cause (a) sluggish kinetics due to the large nucleation and dissolution energy barriers for S_8 and Li_2S; (b) internal impedance increase in the subsequent cycling due to the uncontrolled deposition of redox end-members at the cathode, leading to high overpotential that is amplified in high current densities; and (c) cathode structural deterioration upon extensive cycling due to material disconnection and delamination from the current collector. For these reasons, polymeric binders and carbon additives are added in the cathode matrix. The following two sections focus on approaches that the Li-S community has taken on these fronts.

1.3.1 Sulfur Host

The principal idea of utilizing host materials at the sulfur cathode is to confine polysulfides in the cathode, to provide the requisite intimate contact for e^- transfer, and facilitate and Li^+ ion egression to both S_8 and Li_2S. Early developments on sulfur host materials have been centered on nanostructured porous carbons, including CMK-3,[18] porous hollow carbon spheres,[19, 20] and multi-modal porous carbons[21, 22, 23], to provide a physical entrapment of polysulfides. Interwoven 3D conductive network formed from 2D graphene,[24, 25, 26] or 1D carbon nanotubes (CNTs)[27]/carbon nanofibers (CNFs)[28] have also been used to serve as a pseudo current collector to improve the energy density at the cell level. However, Li-S cells fabricated from these carbonaceous hosts still suffer from rapid capacity fading over long term cycling ($>$ 200 cycles). This is fundamentally because physical adsorption of polysulfides can only spatially confine the redox intermediates by limiting their diffusion into the electrolyte.[23, 29, 30] As the impregnated sulfur is inevitably accessed by the liquid electrolyte during (dis)charge, the soluble high order polysulfides can still diffuse out of the host materials regardless of pore structures and designs.

Instead, host materials that chemisorb polysulfides show good capacity retention. That is because the lone electron pairs in the polysulfide anion (S_n^{2-}) render the molecule as a soft Lewis base. Polysulfide retention can hence be achieved by the electrostatic or Lewis acid/base interactions between the lithium polysulfide molecule and the surface charge species of the host materials. For example, compositing sulfur with polymeric host materials was advantageous in comparison with simple carbon.[18, 31, 32] This is in

particular the case for electrical conductive polymers, such as polyaniline and polypyrrole, that have conductivities on the range of 1×10^{-2} S·cm^{-1} to 1×10^{2} S·cm^{-1}.[33] The advantages of utilizing polymer as sulfur host materials is threefold. First, polymers are typically synthesized at temperatures below 100 °C which enable sulfur/polymer cathode composite to be fabricated in-situ, in comparison with the carbonization process that is typically conducted at temperature well above 600 °C. Second, the good mechanical resilience in polymer can combat the drastic volumetric variation (80 %) in the cathode, and alleviate the pulverization of cathode materials (S + C + binder) during cycling. Third, the physicochemical properties in polymer can be tailored and optimized for a specific use thanks to the unique chain structures and rich variety of functional groups available.

In fact, studies reveal that nitrogen and oxygen atoms on the functional groups feature higher electronegativities (N: 3.04; O: 3.44 on Pauling scale) and posses extra lone-pair electron (N: s^2p^3; O: s^2p^4) in relation to the adjacent carbon. These factors that enable the polymers to exhibit strong Lewis acid-base interactions with lithium polysulfides.[34, 35, 36, 37]

Table 1.2. The calculated binding energies of Li_2S_n and Li_2S with common functional groups found in polymer. LiS* represents Li_2S_n. Values are tabulated from [38].

Moiety	E_b Li_2S_n [eV]	E_b Li_2S [eV]
Amine	1.29	1.10
Ester	1.26	1.10
Amide	1.23	0.95
Ketone	1.20	0.96
Imide	1.02	0.88
Ether	1.01	0.71
Disulfide	0.85	0.92
Thiol	0.84	0.76
Nitrile	0.77	0.60
Sulfide	0.66	0.87
Fluoroalkane	0.62	0.40
Chloroalkane	0.46	0.26
Bromoalkane	0.42	0.23
Alkane	0.30	0.23

Metal oxides too are attractive host materials because the surface metal and oxygen atoms can engage in monolayered, synergistical electrostatic interactions with polysulfide anions and lithium cations, respectively.[39] The first evidence for the chemical interactions between metal oxides and $Li_2S_n$was provided in the work by Evers *et al.* [40] Pang *et al.* presented an electrical conductive Magnéli phase Ti_4O_7 as the host material that combines good electrical conductivity with strong chemical binding ability for polysulfides. The authors showed Ti_4O_7 engages a chemical interactions with Li_2S_n via a redox chemistry. This is evidenced by a slightly oxidized bridging and terminal sulfur environments in Li_2S_4 when the the molecule contacted with Ti_4O_7 (**Figure 1.5A**).[41] As a result, impressively low capacity decay rate of 0.06 % per cycles for 500 cycles at 2C rate with 60 wt.% sulfur loading was achieved (**Figure 1.5B**).

In comparison with oxides, sulfides bind to polysulfides through a similar concept but offer several key strategic advantages. These include superior sulfiphilicity, electronic conductivities that are comparable to carbons, and good Li^+ ion diffusion properties.[42] These principles have been beautifully exemplified in a recent report by Xue *et al.* that utilized lithiated Mo_6S_8 as both polysulfide adsorbent and an mix conductor to serve as Li^+-ion and electron conducting vehicle to facilitate the sulfur redox process.[43] Pioneered by work on Co_9S_8, Pang *et al.* elucidated how transitional metal sulfides bind to polysulfides through a dual interaction of $Li^+ \rightarrow S^{\delta-}$ (of Co_9S_8) and $S_n^{2-} \rightarrow Co^{\delta+}$.[44] Interestingly, a recent calculation work by Zhou *et al.* suggests sulfides can also lower the overpotential on the initial charge process by improving Li_2S decomposition efficiency.[45]

These early works suggest offering a proper electronic conducting pathway for sulfur reduction is as equally important as polysulfide binding effects in Li-S cells. Recent studies done on a variety of host materials, independently by Tao *et al.* and Peng *et al.*, further confirmed simply confining Li_2S_n at the cathode using polar host material cannot guarantee functional Li-S cells.[39, 46] Because the charge transfer and conversion of high-order Li_2S_n to Li_2S is kinetically sluggish, any delay in this process would cause Li_2S_n accumulation on the cathode surface, leading to film-like Li_2S deposition and deteriorated electrochemical performances. This problem can be further aggravated at a practical sulfur loading due to limited vertical ion and electron transport across the thick electrode, and leading to an overpotential penalty due to activation energy barrier for Li_2S growth (**Figure 1.5C**). This surface chemistry well explained how Li-S cells fabricated with Al_2O_3[39] or $Mg_{0.6}Ni_{0.4}O$[47] could only be served as additives due to their very poor conductivity. In other words, providing

an electron-conduit for Li_2S nucleation is the key for enabling in sulfur electrocatalysis for hosts materials that have exhibit good reactivity with Li_2S_n (bottom-panel, **Figure 1.5C**). After all, the surface bound polysulfide species need to diffuse to an electrically conductive substrate for the electrochemical reaction to proceed. For the same reason, metal carbides[46]/nitrides[48]/borides[49]/phosphides[50] are considered as effective sulfur host materials.[51, 52, 53]

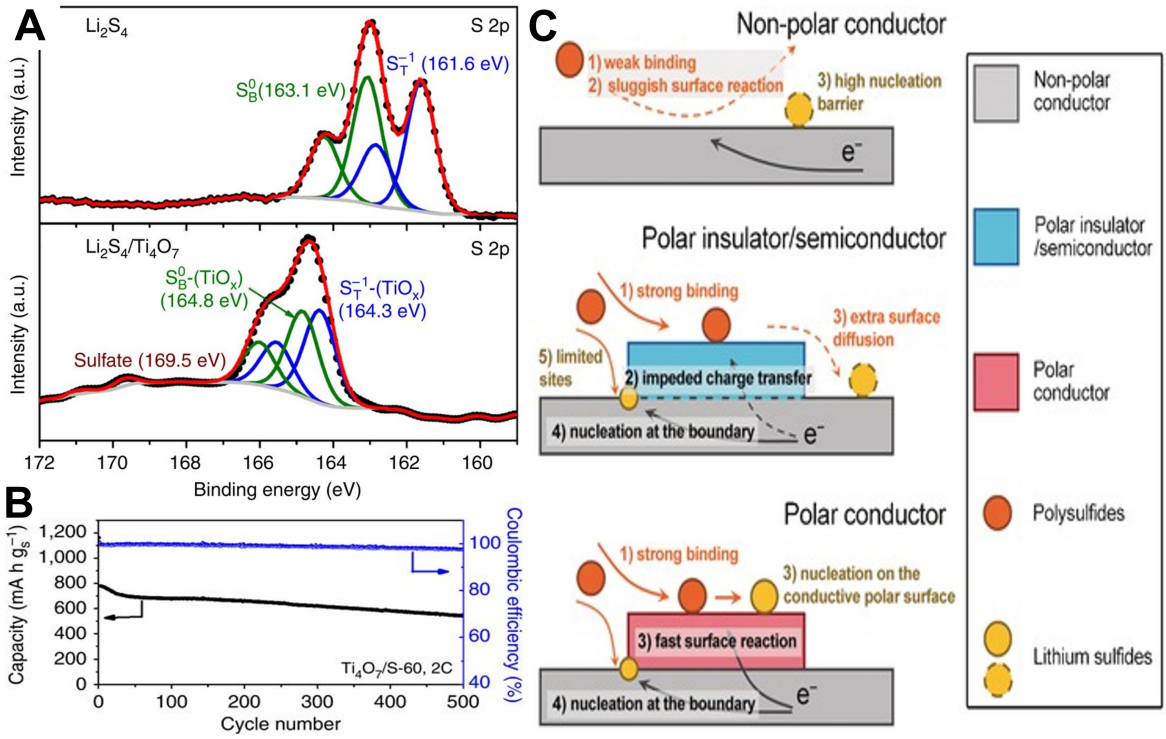

Figure 1.5. Polysulfide chemisorption mechanism in Li-S battery. (A) High-resolution XPS S 2p spectra of Li_2S_4 before (top panel) and after in contact with Ti_4O_7 (bottom panel). (B) High-rate cycle performance of the sulfur cathode fabricated Ti_4O_7 at 2C. (C) Illustration of the working mechanism of the polar conductor as it meets the demand for both adequate binding and fast charge transfer. (A-B) are reprinted from [41] (C) is reprinted from [46].

Aside from the traditional Coulombic/Lewis acid-base interactions, other hosts enable sulfur atoms to be grafted onto its surface. This mechanism provides additional mediation pathway for sulfur redox in Li-S batteries because of the eradication and reconstruction of S-S bonds during cycling. The surface of δ-MnO_2 engages in an unique mechanism – thiosulfate-polythionate conversion.[54].

This process involves a two-step reaction. The surface Mn^{4+} first oxidizes S_n^{2-} and hereby decorate the MnO_2 nanosheet with surface bound thiosulfate ($S_2O_3^{2-}$) intermediates. The remaining high-order polysulfides (S_n^{2-}, $n > 4$) then makes a nucleophilic attack on the $S_2O_3^{2-}$ species to form insoluble polythionate complexes ($[O_3S_2{-}S_n{-}S_2O_3]^{2-}$, **Figure 1.6**). This process continues until all the polysulfides have been consumed. As the catenated sulfur are electrochemically active, the resultant sulfur cathode achieved a low fading rate of 0.036 % per cycles for over 2000 cycles.[54].

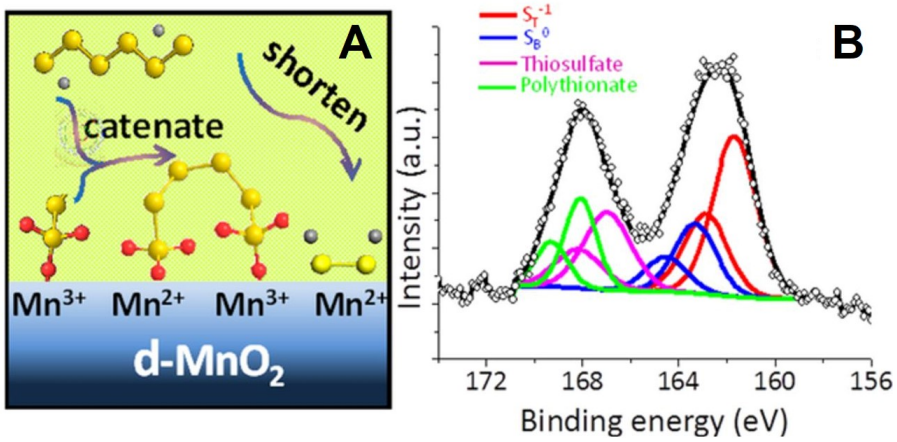

Figure 1.6. Polysulfide redox mediation by thiosulfate/polythionate mechanism. (A) Schematic of polysulfide entrapment and mediation via thiosulfate-polythionate conversion by MnO_2; (B) High resolution S 2p spectrum of Li_2S_4 after contact with MnO_2, showing the appearance of thiosulfate and polythionate. Reprinted from [55].

1.3.2 Polymeric Binder

The cycling stability of Li-S cells is not only not sustained by host materials to retard polysulfide dissolution, but by polymeric binder to combat material delamination and large volume change (80 %) also. Poly(vinylidene fluoride) (PVDF) has been conventionally utilized as a binder in the Li-ion battery technology; however, it lacks the necessary functional groups for polysulfide adsorption, as well as adhesivity and mechanical properties to hold the sulfur cathode components together. In the following, I will briefly provide a basic understanding in the mechanical properties for polymeric binder and some of the recent efforts in using alternative polymers as binders in Li-S technology.

Adhesion between two materials is descried using adhesion joint strength theory developed by Wake *et al.* in 1982, and it comprises of two parameters: mechanical interlocking and interfacial interactions as shown in **Figure 1.7**[56] Mechanical interlocking arises from the solidification of binder solution upon evaporation of the casting solvent, which leads to an embedded polymeric film filling the gaps and pores of the cathode component particles (**Figure 1.7A**). Polyamidoamine dendrimer, for example, follows this mechanism because hyper-branching architecture in the polymer network provides plentiful pore volume for good adhesion towards both the S/C composite and the carbon-coated Al current collector.[57] The resultant sulfur cathodes delivered a high areal capacity of $4.32\,\mathrm{mA{\cdot}h{\cdot}cm^{-2}}$ at a decent sulfur loading of $4.4\,\mathrm{mg{\cdot}cm^{-2}}$. Interfacial interactions, on the other hand, occurs at the binder/material interface, and its mechanism is entirely based on the hydrogen/polar bonding between binder, host materials, and current collector (**Figure 1.7B**). Thus, the same polar functional groups,

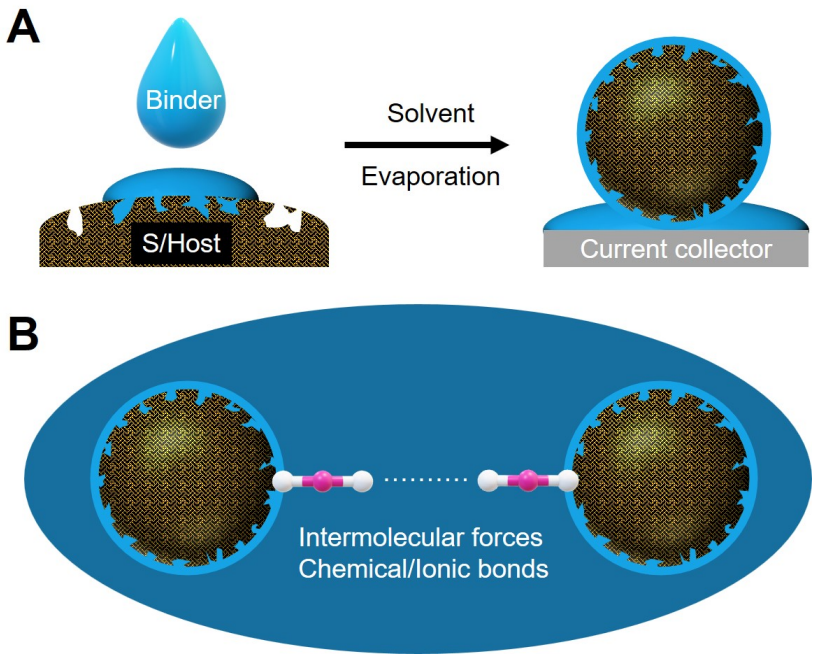

Figure 1.7. Schematic illustration of binding mechanism in polymeric binder: Adhesion provided by (A) mechanical interlocking and (B) interfacial interactions.

such as hydroxyl (–OH); carboxyl (–COOH); amine ($–NH_2$); and amide ($–CONH_2$), that chemisorb polysulfides also promotes material adhesion (**Table 1.2**).[38, 58]

While tuning the polymers' functional group chemistry can improve its adhesivity, the high Young's modulus exhibited by linear polymers cannot provide the desired mechanical strength and flexibility to withstand the large volume change during cycling. In contrast, compositing various binders to construct a 3D network is a much more viable avenue. For example, the confluence of the plasticizer carboxymethyl cellulose and highly elastic styrene-butadiene rubber ensures both uniform material distribution on the cathode surface and the formation of a continuous robust 3D network. Shaibani *et*

al. recently reported an expansion-tolerant architecture using this approach, manifesting a sulfur cathode with loading up of 15 $mg \cdot cm^{-2}$ to exhibit an areal capacity up to 19 $mA \cdot h \cdot cm^{-2}$.[59]

In comparison with polymer blend, however, cross-linking copolymerization poses two advantages. First, covalent bonds are much more resilient to the stress-strain derived from the volume expansion during cycling. Second, cross-linked polymeric binders tend to exhibit superior polysulfide adsorptivity because of the moieties are now freed to engage in electrostatic/polar interactions with the intermediate redox species. Based on this concept, Pang *et al.* copolymerized carboxymethyl cellulose and carboxylic acid together.[60] The in-situ esterification ensures efficient physical/electrical connection between individual cathode component, while maintaining high elasticity to accommodate the large volume expansion (**Figure 1.8A**). SEM analysis revealed a crack-free sulfur cathode was successfully fabricated using this binder, in comparison with that prepared using the standard PVDF materials (**Figure 1.8B**). Using this approach, a Li-S cell with 14.9 $mg \cdot cm^{-2}$ sulfur loading was operable, delivering an areal capacity up to 15.5 $mA \cdot h \cdot cm^{-2}$ (**Figures 1.8C** and **1.8D**).

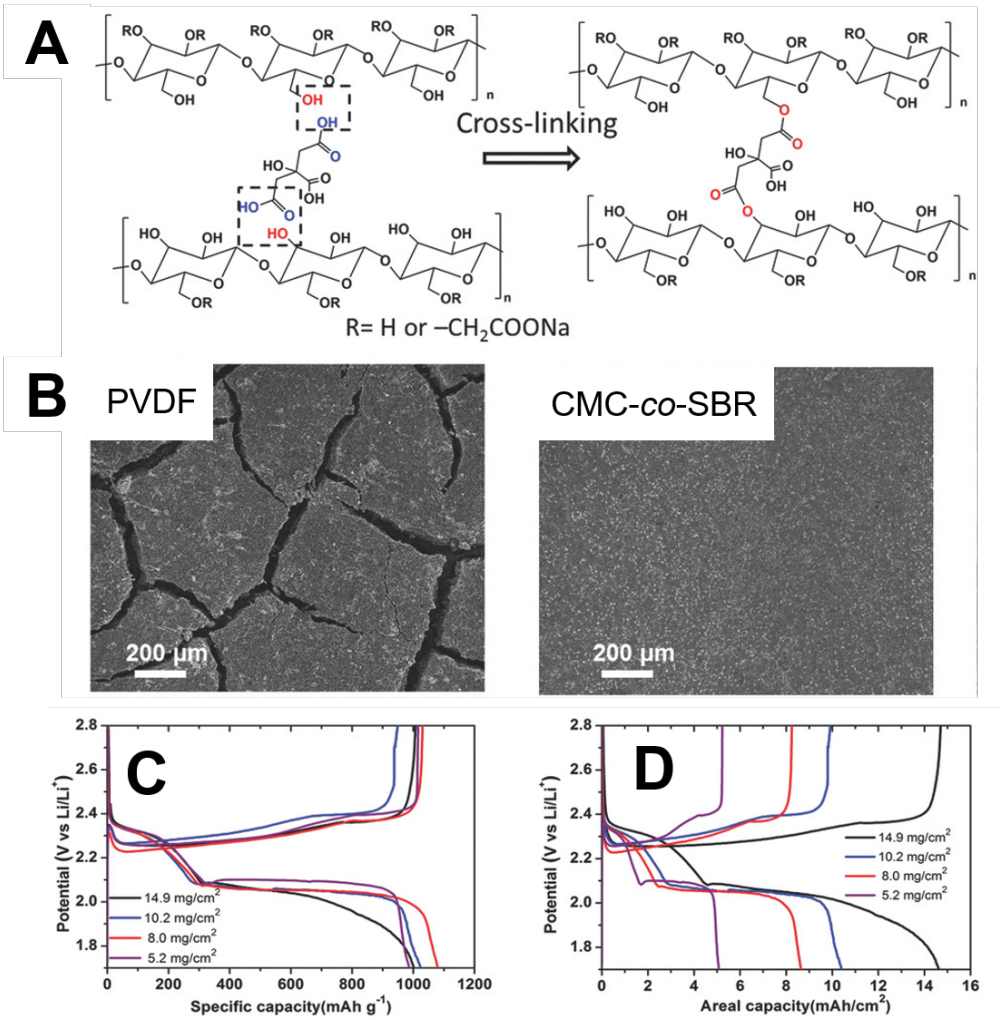

Figure 1.8. Cross-linked sodium carboxymethyl cellulose-critic acid binders for Li-S cell. (A) Schematic of the in-situ cross-linkage. (B) SEM images the sulfur cathodes fabricated using PVDF (left) cross-linked binder (right). Electrochemical profile of the sulfur cathode fabricated with the cross-linked binder with varied sulfur loading as a function of (C) mass specific capacity and (D) areal capacity. Reprinted from [60].

1.4 Li-O_2 Battery

Oxygen - a congener element to sulfur in the periodic table - can also be coupled with lithium metal anode to fabricate what is known as Li-O_2 battery. **Figure 1.9A** shows the configuration of a typical aprotic Li-O_2 battery: a Li anode and a porous carbon cathode, separated by a Li^+ conducting organic electrolyte. The typical electrochemical profile is shown in **Figure 1.9B**.[61] During discharge, molecular O_2 bound on the carbon cathode surface is reduced via one electron transfer to form lithium superoxide (LiO_2) as the intermediate species (**Equation 1.6**). However, the thermodynamic instability of LiO_2 species renders the redox intermediate to either be chemically disproportionated (**Equation 1.7**) or electrochemically reduced (**Equation 1.8**) to form the final product: Li_2O_2. Li_2O_2 is directly oxidized to evolve O_2 on charge (**Equation 1.9**).

$$Li^+ + O_2 + e^- \rightarrow LiO_2 \qquad 1.6$$

$$2LiO_2 \rightarrow Li_2O_2 + O_2 \qquad 1.7$$

$$LiO_2 + Li^+ + e^- \rightarrow Li_2O_2 \qquad 1.8$$

$$Li_2O_2 \rightleftharpoons O_2 + 2Li^+ + 2e^- \qquad 1.9$$

Ever since its concept was established by Abraham *et al.* in 1996,[62] the excitement surrounding aprotic Li-O_2 battery lies at its highest theoretical energy density of $3500\,W{\cdot}h{\cdot}kg^{-1}$ - assuming a 2-electron transfer in O_2/O_2^{2-} redox couple - amongst all

rechargeable battery systems. However, with great advantages there must come great challenges. As the Li-O_2 battery system enjoys the highest energy density (**Table 1.1**), virtually infinite capacity (assuming sufficient supplies of lithium and oxygen), and easy fuel accessibility as oxygen constitutes 20 % of air, this technology faces many unique challenges. First, Li-O_2 cells generally suffer from poor round-trip efficiency (~60 - 70 %). The open circuit potential (OCV) for Li-O_2 cell is 2.96 V *vs.* Li/Li^+. While the

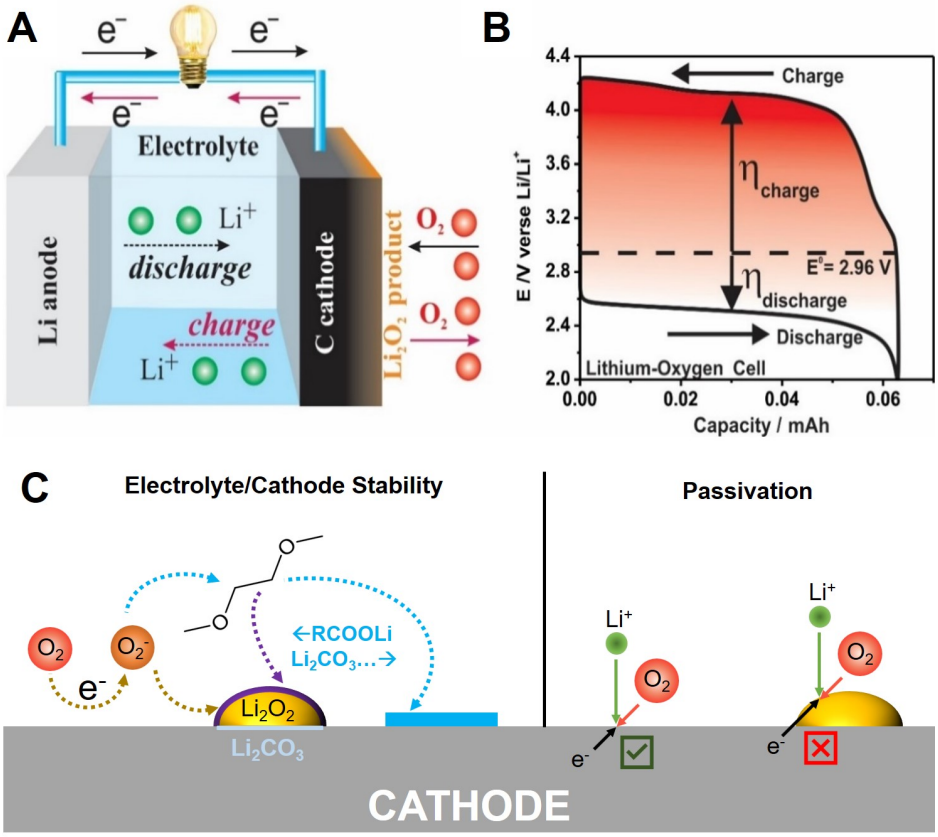

Figure 1.9. Aprotic Li-O_2 battery. (A) Configuration, (B) electrochemical profile, and (C) technical challenges. (A-B) are reprinted from [61].

small activation energy barrier for oxygen reduction reaction (ORR) results in a small discharge overpotential of 200mV, this is nothing in comparison with the large charge overpotential (> 1V) typically observed in oxygen evolution reaction (OER). Second, the cycle life of aprotic Li-O_2 cells is mostly below 100 cycles, significantly lower than that in both Li-S and LIB systems. Third, dissolution of LiO_2 and precipitation of Li_2O_2 at the end of discharge results in cathode passivation. This leads up to cell voltage drop, delivering limited capacity. These three issues arise from the tendency of electrolyte and cathode decomposition by $O_2^{-\bullet}/O_2^{2-}$, and the limited surface area/pore volume of the carbon cathode (**Figure 1.9C**). Details on the origin of these problems and the efforts taken to mitigate them are discussed below.

1.4.1 Electrolyte Decomposition

The largest scientific and technical challenge residing in Li-O_2 technology development is finding a suitable electrolyte to sustain and support the reversible conversion of O_2/O_2^{2-} redox couple. For instance, the donocity of solvents has a large influence on Li_2O_2 growth and oxidation mechanism.[63, 64] To maximize the cell performance, the electrolyte also needs to feature high ionic conductivity and high O_2 solubility and diffusivity - properties shared by many organic solvents. What is not trivial is finding an electrolyte system that is chemically stable towards (su)peroxides.

Because of their popularity in LIB technology, carbonate-based solvents such as propylene carbonate were first employed as the electrolyte in the early stages of Li-O_2 development. However, it later became apparent that carbonates react readily with lithium

peroxide, forming lithium carbonate, acetates, carboxylate etc. as discharge products. Detail analysis by Freunberger *et al.* further points out that the accumulation of such materials blocks the active sites in the carbon cathode over cycling, leading to limited discharge capacity. Moreover, carbonate oxidation during cell charge results in self-polymerization reaction that forms an insulating gel-like layer on the surface of lithium metal anode. At the end of the day, oxygen evolution was never detected when using carbonate electrolytes.[65] Similarly, dimethyl sulfoxide (DMSO) is susceptible to (su)peroxide attack to form dimethyl sulfone as the decomposition product.[66]

Ether-based electrolyte has now become the most commonly used electrolytes in Li-O_2 batteries because of its relatively lower polarity, and Li_2O_2 is found to be the major oxygen reduction product on first discharge. However, the β-hydrogen in the ether backbone can still be abstracted by the superoxide and peroxide moieties (**Figure 1.10A**), triggering a cascade of radical reactions that eventually lead to electrolyte decomposition. This is evidenced by the rapid capacity decay and diminishing Li_2O_2 materials just after several cycles, as well as detection of formates, carbonates, acetates, and polyoxalates.[67, 68] Driving the Li-O_2 cell to a high oxidative potential (>4 V *vs.* Li/Li^+) can remove these undesired products, albeit most aprotic solvent may have been also oxidized at this point. In summary, there is simply no conventional organic electrolyte is truly stable towards lithium superoxide/peroxide.

Clearly, rational design for new solvent molecule and exploration of novel electrolyte systems are priorities for the development of Li-O_2 batteries. Substituting the liable hydrogen atom, which is the starting point of solvent decomposition, is pioneered by Adam *et al.* In that work, they capped all four β-hydrogen in glyme with methyl

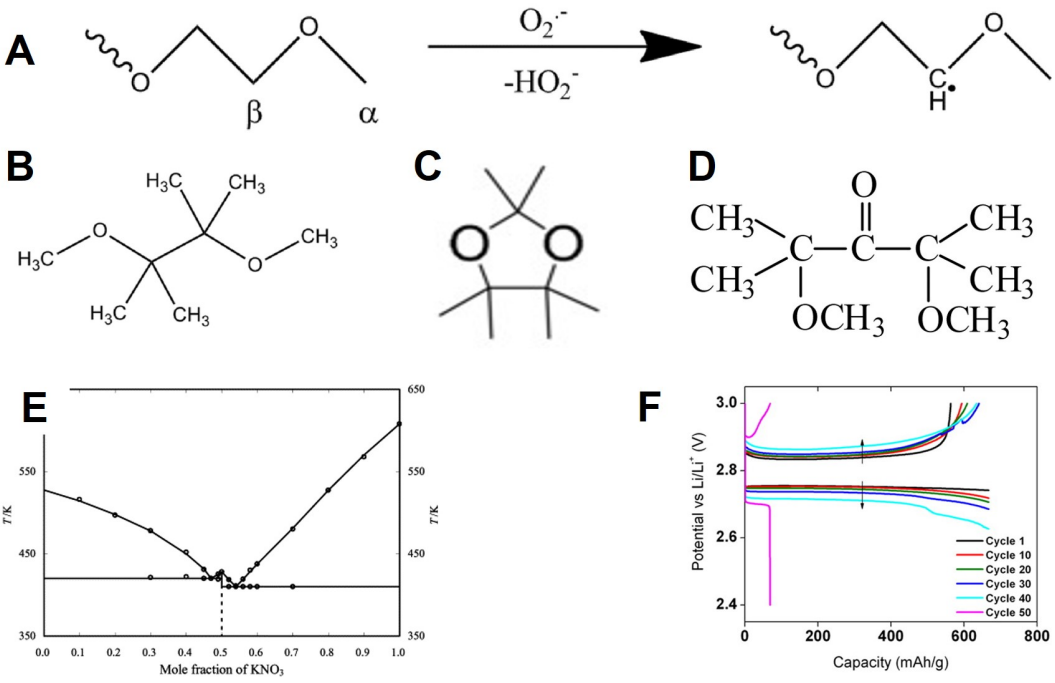

Figure 1.10. Electrolyte challenges in Li-O_2 battery. (A) β-hydrogen abstraction from ether solvent by superoxide. Molecular structures of (B) 2,3-dimethyl-2,3-dimethoxybutane, (C) 2,2,4,4,5,5-hexamethyl-1,3-dioxolane, and (D) 2, 4-dimethoxy-2, 4-dimethylpentan-3-one as stable solvent candidates. (E) Phase diagram of $LiNO_3$-KNO_3 showing the eutectic point. (F) Electrochemical profile of a Li-O_2 battery operating at 150 °C using $LiNO_3$-KNO_3 molten salt as the electrolyte and carbon as the cathode. (A-D) are reprinted from [61], (E) is reprinted from [69], and (F) is reprinted from [70].

group, forming 2,3-dimethyl-2,3-dimethyoxybutane as shown in **Figure 1.10B**.[68] A 10-fold reduction in CO_2 generation and lack of electrolyte decomposition byproducts such as lithium formate, in comparison to glyme, clearly suggest electrolyte decomposition has been suppressed. Such electrolyte designs are further adopted by researchers worldwide. For instance, Huang *et al.* recently synthesized a fully methylated cyclic ether, 2,2,4,4,5,5-hexamethyl-1,3-dioxolane, by replacing all the acidic hydrogen in DOL

with methyl groups (**Figure 1.10C**).[71] The excellent chemical stability of their newly designed electrolyte is evidenced by the lack of CO_2 evolution during charge. Their resultant Li-O_2 cell was able to sustain 157 cycles - a 4-fold improvement in comparison with the conventional DME or DOL electrolyte. Sharon *et al.* too designed 2,4-dimethoxy-2, 4-dimethylpentan-3-one.[72] Essentially it is an acetone-derivative with its hydrogen atoms replaced with bulky methoxy groups (**Figure 1.10D**), although the high reactivity of the carbonyl moieties requires a protected lithium metal anode for the cell to function.

Alternatively, binary or ternary inorganic salts that feature a eutectic point at an evaluated temperature has a long history in Na-S or sodium-nickel-chloride battery systems as electrolyte systems. Girodani *et al.* first proposed $LiNO_3$-KNO_3 eutectic, which presents a melting point of 125 °C (**Figure 1.10E**) as an electrolyte for Li-O_2 cells.[70] At 150 °C, the molten salt presents a high ionic conductivity of 88 $mS \cdot cm^{-1}$. The resultant molten salt Li-O_2 cell thus exhibited a very low discharge/charge overpotential of 50 mV, and a highly reversible ORR/OER process (**Figure 1.10F**). This finding opens a door for the reversible 4-electron transformation in oxygen electrochemistry, which will be thoroughly discussed in **Chapter 6**.

1.4.2 Cathode Corrosion

In Li-O_2 electrochemistry, Li_2O_2 is the electron storage material that gets formed and decomposed in each cycle. In other words, the cathode serves as an electronic conductive matrix for the oxygen reduction & evolution reactions to take place; and yet, it plays

a pivotal role in determining the maximum capacity achievable. The accumulation of Li_2O_2 materials on the electrode/electrolyte interface will eventually occludes additional O_2 from reaching the electrode surface. This in turn curtails Li_2O_2 production, resulting in a voltage drop at the end of discharge. This problem is further amplified by the formation of decomposition products discussed below.

Carbons are considered as the standard cathode materials in Li-O_2 batteries because of their high electronic conductivity, high discharge galvanometric capacity, and low cost.[73] In particular, they adopt a variety of morphologies that are of high surface area and pore volume to support Li_2O_2 formation. However, carbon suffer from Li_2O_2 corrosion, forming an insulating Li_2CO_3 layer at the Li_2O_2/C interface (**Equations 1.10** and **1.11**):

$$C + Li_2O_2 + \frac{1}{2}O_2 \rightarrow Li_2CO_3 \qquad 1.10$$

$$C + 2Li_2O_2 \rightarrow Li_2CO_3 + Li_2O \qquad 1.11$$

The electrode active surface will be covered by the Li_2CO_3 materials over extensive cycling. Using ^{13}C labelled carbon electrode, Thotiyl *et al.* further demonstrated the parasitic product ($Li_2{}^{13}CO_3$) can only be removed through electrochemical oxidization at 4 V *vs.* Li/Li^+ to evolve $^{13}CO_2$, a potential at which most decomposed electrolyte materials are oxidized to evolve CO_2 (**Figure 1.11**) also.[74] However, because CO_2 will be electrochemically deposited back at the cathode surface as Li_2CO_3 on the subsequent discharge procedure, this never-ending parasitic reaction ultimately leads to cathode passivation and early cell death.

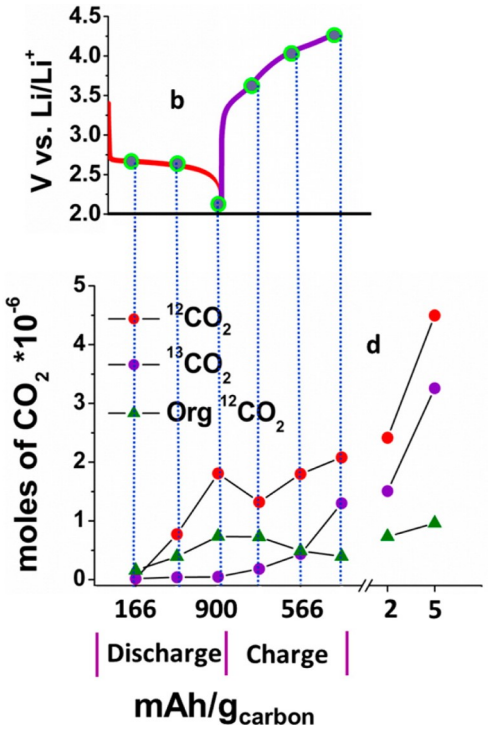

Figure 1.11. Challenges in the carbon cathode of Li-O_2battery. Determination of lithium carbonate amount at different stages of Li-O_2 cell operation based on a carbon cathode and ether electrolyte. Carbonate amount was determined by treatment of the cathode with acid to signal Li_2CO_3, and Fenton's reagent to signal the Li-carboxylate. Reprinted from [74]

Oxidative corrosion-resistant, non-carbonaceous materials with high electronic conductivity are promising alternative cathode materials for aprotic Li-O_2 batteries. Peng *et al.* first reported the use of nanoporous gold cathode for their DMSO-based Li-O_2 battery; the cell retained 95 % of its initial capacity for 100 cycles and CO_2 evolution on charge was significantly reduced.[75] However, the high cost and mass of Au eradicate the key advantages of the high specific energy and cost effectiveness offered by Li-O_2 cells. In search for more practical alternatives, the same research group at the Oxford University came across titanium carbide (TiC). The Li-O_2 cell fabricated with

TiC cathode and DMSO electrolyte achieved Li_2O_2 product with > 95 % purity and a complete oxidation on charge, resulting in a > 98 % capacity retention over the course of 100 cycles.[76] The excellent cyclabilty of the cell is attributed to both the high conductivity of the bulk material and a stable passive oxide layer (TiO_{2-x} that formed on the surface of the TiC upon contact with Li_2O_2). This layer protects the bulk cathode material from further oxidation. A closer examination by Adam *et al.* further revealed the thickness of the surface oxide is critical in enabling good electron and mass transport, as an insulating TiO_2 surface layers on TiC - even as thin as 3 nm - can completely inhibit the charge reaction.[77] TiC nanoparticles lack of such a thick oxide layer which readily facilitate Li_2O_2 oxidation at a much lower charge overpotential. This finding demonstrates a precise control of the surface chemistry at the nanoscale is the key for the fabrication of efficient Li-O_2 cells. I will also demonstrate the importance of surface chemistry on oxygen electrochemistry in **Chapter 6**. Nonetheless, these discoveries led to further investigation on other conductive materials such as Ti_4O_7,[78] RuO_2,[79] and MoS_2.[80] However, their chemically stability against (su)peroxide and electrocatalytic effects remains a topic for debate and research.[63, 81]

1.5 Li Metal Anode

Li-S and Li-O_2 battery requires the use of lithium metal as the anode. In fact, Li metal anode has been long considered as the *Holy Grail* in the battery technology for two reasons. First, as the lightest member of all metals in the periodic table in terms of both molar mass ($6.9\,g{\cdot}mol^{-1}$) and density ($0.53\,g{\cdot}cm^{-3}$), Li metal offers extremely high

theoretical gravimetric and volumetric capacities of 3880 $mA{\cdot}h{\cdot}g^{-1}$ and 2060 $mA{\cdot}h{\cdot}cm^{-3}$, respectively. Second, the high Fermi energy level of Li metal endows an extremely low reduction potential of −3.02 V *vs.* SHE. It is exactly this feature that enables Li-S and Li-O_2 battery systems to exhibit a high voltage and high specific energy. In fact, metallic Li was used in the infancy of rechargeable Li battery research. When Whittingham discovered reversible Li^+ intercalation mechanism in the layered TiS_2 material in 1976, he was using lithium metal as the negative electrode material.[82, 83] However, the chemical and mechanical instability of lithium poses great safety hazard. Most notably is the fiasco by Moli Energy in the late 1980s that eventually led to the total recall of their Li-MoS_2 battery.[84] This technological disaster ultimately allowed graphite to win the competition as the standard anode material in lithium ion battery. However, with LIBs approaching the limit of their capabilities and commercialization of Li-S and Li-O_2 battery technology just around the corner, attempts to stabilize lithium metal during cycling is becoming an important research topic.

1.5.1 Lithium Metal Anode Challenges

As summarized in **Figure 1.12**, the dilemma in using Li metal as anode is fundamentally rooted in: (a) the dendritic growth of lithium metal during charge; (b) the chemical and structural instability of the passivating solid electrolyte interphase (SEI) layer; and (c) lithium corrosion by the crossover of soluble sulfur/oxygen redox species. The origin of these challenges are discussed below.

Similar to most metals, lithium metal tends to deposit in a mossy dendritic form.

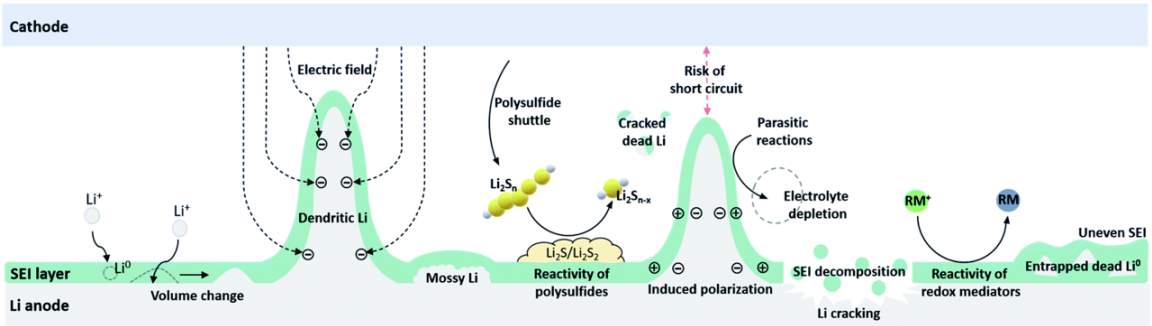

Figure 1.12. Li metal anode challenges. Reprinted from [85]

While there have been many theoretical models proposed, along with extended experimental work and analytical tools, in the past 40 years to describe the onsets and growth of lithium dendrite, [86, 87, 88, 89] the most widely accepted one is the space charge model proposed by Chazalviel in 1990. Essentially, the model states that lithium dendrite formation is triggered by anion depletion near the Li metal surface, which creates a space charge barrier and hence the model name.[90] Chazalviel further ascribes the space charge effect is induced by the concentration gradient of anion ($\frac{dC_a}{dx}$) across the electrode/electrolyte interface. This gradient is influenced by the anion transference number (t_a) and ambipolar diffusion coefficient (D) of the lithium salt in the electrolyte (**Equation 1.12**):

$$\frac{dC_a}{dx} = -\frac{Jt_a}{FD} \tag{1.12}$$

As lithium dendrites grow, they will penetrate through the separator and reach to cathode, thereby internally short-circuiting the cell. The most obvious result is thermal runaway reactions, with the possibility of cell explosion because of the large amount of heat released to the flammable organic electrolyte. In a separate work, Chazalviel

further predicts the maximum current density (J^*) and Sand's time (τ_{Sand}) at which dendrites are expected to form under such diffusion-limited condition: [91]

$$J^* = \frac{2FC_0D}{\tau_a L} \tag{1.13}$$

$$\tau_{Sand} = \pi D \left(\frac{FC_0}{2Jt_a}\right)^2 \tag{1.14}$$

here C_0 refers to the bulk ion concentration; L is the inter-electrode distance, and J is the applied current density.

Another major contributor to lithium anode failure is the instability of the SEI layer that formed as a result of the adverse reactions between the metal and neighboring electrolyte species (both the salt and the solvent).[92, 93, 94] Although the existence of such a passivisation layer may not be all that harmful for the stability of lithium metal if it posses characteristics of resilient mechanical properties, high ionic conductivity and electrical resistance, low solubility in the electrolyte solvent, and a wide electrochemical window. However, often time that is not the case. The non-uniformity and high-porosity of the SEI layer enables the electrolyte species to creep into its defects. In addition, the virtually infinite volume change of Li metal during stripping and plating puts a tremendous mechanical stress on the meta-stable SEI layer that eventually fractures, exposing fresh lithium. The exacerbated reactivity of the newly exposed lithium (either pre-existing or freshly formed dendrite) with the electrolyte leads to eventual *dry-out* of the cell and convert Li dendrites to electrochemically inert (*dead*) Li. To further complicate the problem, the structure and composition of the SEI layer is heavily dependent

on the types of salt and solvent used. This renders analysis and prevention measurements difficult.[95, 96, 97] In summary, the combination of these factors lead to dendritic formation and growth at much lower current density than theoretical $J*$ values. The end result is low Coulombic efficiency, increased cell polarization, and premature cell death.[98, 99]

Lithium metal is also subject to corrosion by the crossed-over sulfur and oxygen redox intermediate species (i.e. Li_2S_n and LiO_2). In Li-S battery, there have been numerous accounts of the existence of reduced polysulfide species on the surface of the anode.[16, 100, 101, 102] The polysulfide shuttle process amplifies Li dendrite formation and electrolyte consumption due to the dynamically broken and reconstructed SEI. This problem is often observed high sulfur loading cells where large capacity is pulled.[60, 103] This problem is exemplified in a recent work by Pang *et al.* where a Li-S cell with sulfur loading of $14.9\,mg{\cdot}cm^{-2}$ exhibited significant voltage fluctuation on charge.[60] The authors further articulated that the side reaction between lithium and polysulfides accelerated the formation of the impeding Li_2S/Li_2S_2 layer, resulting in increasing charge overpotential over deep cycling.

Without getting into the details, although a major concern is the issues related to the use of redox mediator, electrolyte additives, and/or novel electrolyte systems to overcome the some of the hurdles in sulfur and oxygen redox chemistries. For example, the sluggish kinetics in sulfur redox and energy penalty associated with Li_2S nucleation/decomposition calls for high donor number solvents that feature higher solvating capability for polysulfides. However, Li-S cells that employ these high solvating electrolytes, such as DMSO, acetonitrile, and dimethylacetamide, generally suffer from the

poor chemical compatibility between the solvents and lithium metal. While the employment of two-compartment cells that use Li^+ conducting ceramic membrane to isolate the lithium metal offers a solution, this approach clearly defeats the purpose of the original design of a full solution phase reaction for fast kinetics.[104] Similarly, the redox mediators designed to facilitate ORR/OER can cross over to the lithium metal anode due to their mobile nature. A recent work by Ha *et al.* highlights how oxidized redox mediators, formed during Li-O_2 cell charging step, can decomposes the protective SEI lithium oxide layer through the same electrocatalytic mechanism that oxidizes the lithium peroxide at the cathode.[105] The spontaneous electrochemical reaction exposes fresh Li metal to the redox mediator and resulting in direct loss of Li metal. The take home message is that lithium metal surface needs to be well protected before any realization on practical and safe Li-metal batteries.

1.5.2 Approaches in Li Metal Anode Protection

Considerable efforts have been put forward to enable safe operations of lithium metal anode. Modifying lithium surface[106] and accommodating Li deposition using a lithiophilic host material[107, 108] represent some of the strategies to improve the infinite volume expansion or reduce the reactions between electrolyte and lithium metal. Another common approach is tuning electrolyte composition.[109, 110] Because protecting the lithium material from corrosion are more predominate in Li-S and Li-O_2 battery systems, details on methods to purely suppress lithium dendrite formation and improves the stability of SEI are provided in other publications.[94, 111, 112, 113]

Ever since its discovery by Mikhaylik *et al.* in 2008, $LiNO_3$ is an indispensable Li-S electrolyte component because it can form a stable SEI interface.[114] Comprehensive studies show that the protective layer is mainly composed of $LiNO_2$, Li_2O, Li_2SO_3, and Li_2SO_4 materials.[100, 115] Further studies suggest there exists competitive reactions between the nitrates and polysulfides toward Li.[100, 116, 117] The first direct reduction of $LiNO_3$ by Li metal passivates the metal's surface, followed by an oxidation of Li_2S_nthat forms the final protective layer on the Li metal surface. This synergistic effect hence enables rechargeable Li-S cells with a CE close to 100 % to be achieved. However, because of the fragility of this SEI material and the irreversible nitrate reduction at the cathode, the nitrate will eventually be depleted over the course of long-term cycling.[30, 118] In fact, high sulfur loading ($> 2\,\mathrm{mg{\cdot}cm^{-2}}$) cathodes still suffer from a low Columbic efficiency of ∼90 % regardless of the types of host materials.

Surface coating on Li is a popular avenue as it can prevent the metal in directly contacting with liquid electrolyte while mechanically suppressing dendrite formation. In particular, the advantages of employing highly Li^+ conducting solid-state electrolyte (SSE) is three-fold. First, the use of high elastic modulus (1×10^1 to 1×10^2 GPa) SSE enable an uniform Li^+ influx during plating. Second, the theoretical unity value of Li ion transference number in SSE material decrease the ion concentration gradient upon cell polarization. Extended J^* (**Equation 1.13**) and Sand's time (**Equation 1.14**) are therefore typically observed in these systems. In fact, the solvent-in-salt electrolyte systems described in earlier follows a similar concept.[110] Third, and most importantly, the solid-state electrolyte layer protects the lithium metal from corrosion by novel electrolyte or cathode material crossing over.

For example, Yu *et al.* proposed a chemically stable $Li_{1+x}Y_xZr_{2-x}(PO_4)_3$, x = 0 - 0.15 (LYZP) as a protection layer for lithium metal against polysulfide crossover in Li-S batteries. Their catholyte (Li_2S_6) cell maintained a CE close to 100 % without the use of $LiNO_3$ additives for 150 cycles with a low capacity rating rate of 0.07 % per cycle.[119]. Despite their high ionic conductivity and the ability to block material crossover, the installation of solid-state electrolyte onto Li is usually done ex-situ because SSE synthesis usually requires sintering temperature above the melting point of lithium (180 °C). Moreover, the poor contact between the two solid materials leading to high area specific resistance (ASR). Taking the advantages of lithium's high reactivity towards polysulfides yielding Li_2S as well as the solution-mediated reaction between P_2S_5 and Li_2S to form Li_3PS_4; Pang *et al.* proposed to use these two reagent (P_2S_5 and Li_2S_6) as electrolyte additives to form an artificial SEI layer as shown in **Figure 1.13A**.[120] The rapid formation of the Li_3PS_4 on the surface of the Li prevents the metal anode from any undesired parasitic reactions with the electrolyte (1M LiTFSI in DOL/DME) while ensuring intimate contact between the protection layer material (Li_3PS_4) and Li metal. This results in an 8-fold longer Sand time (**Figure 1.13B**), and a dendrite-free Li surface after 100 cycles of plating and stripping at a current density of 1 $mA{\cdot}cm^{-2}$ for 1 $mA{\cdot}h{\cdot}cm^{-2}$ in Li-Li symmetric cells (**Figures 1.13C** and **1.13D**). In a followup work, the authors further infiltrated commercial Li_3PS_4 solid-state material with polydimethylsiloxane. This approach endows the Li protection layer flexibility to accommodate drastic volume change during cell cycling. A stable operation of a Li-$Li_4Ti_5O_{12}$ cell for 2000 cycles with 95.8 % CE was thus achieved (**Figure 1.13E**).[121]

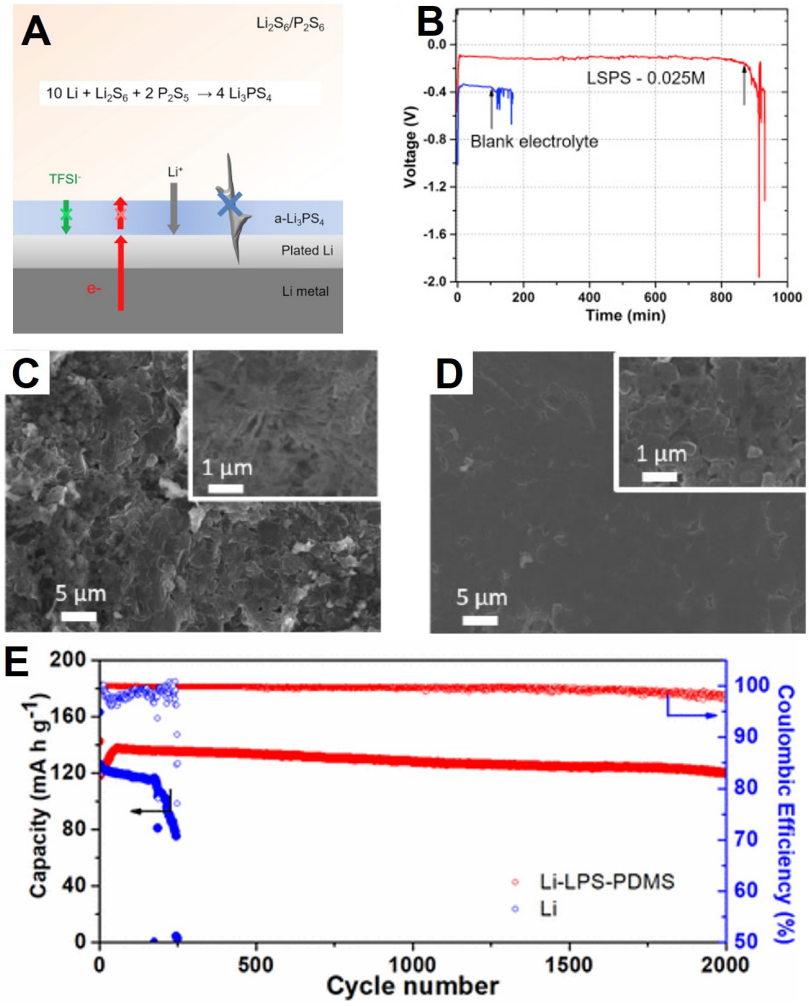

Figure 1.13. Installation of SEI layer for Li anode protection. (A) Schematic Li_3PS_4 artificial solid-state electrolyte layer on Li surface. (B) Evolution of Li-Li symmetric cell voltage upon plating Li on the working electrode at a constant current of 10 $mA{\cdot}cm^{-2}$ in bare Li (blue) and Li_3PS_4 protected Li; black arrows indicate the characteristic Sand time, τ, when dendrite formation starts, as denoted by the voltage divergence. (C-D) SEM images of (C) bare Li and (D) Li_3PS_4 protected Li after 100 cycles of plating/striping. (E) Long-term cycling profile of the $Li_4Ti_5O_{12}$ cathodes coupled with bare Li (blue) or Li–Li_2PS_4-polydimethylsiloxane (red) anodes at a current density of 5C (i.e. 2.1 $mA{\cdot}cm^{-2}$). (A-D) are reprinted from [120] and (E) is reprinted from [121].

1.6 Thesis Motivation

Lithium ion battery technology currently dominates the market as the standard rechargeable battery; however, it is hardly keeping up with future energy density demand. In that regard, Li metal batteries that are based on sulfur (Li-S) and oxygen (Li-O_2) conversion chemistries show great promises because they invoke higher number of electron storage than the transitional metal oxide. Functional Li-S cells based on polysulfide dissolution-precipitation chemistry can now arguably survive 2000 cycles. This is a major accomplishment in comparison with the scenarios in the field a decade ago where only few cycles with low capacity retention rate and extensive overcharge were typically obtained. This is, however, by no means the end of the research road, for some questions in the fundamental sciences and practical challenges remained unresolved. Effectively all non-carbonaceous material exhibit some sort of chemical interactions and electrocatalytic effects toward polysulfides simultaneously. However, fundamental understanding in the mechanism behind in their surface chemistry are still lacking. We still do not know the excellent cyclability observed is the result of simply polysulfide confinement or sulfur mediation by other pathways. New technical challenges residing in the Li-S technology commercialization include low E/S ratio and high sulfur loading. Resolving these two issues require all component in the battery to work cohesively. Furthermore, researchers start to realize the importance of polymeric binder to accommodate the volume change. However, maintaining cathode structural integrity during cycling necessitates the considerations of the polymer binder interactions not only with the cathode materials but also the electrolyte.

The development of the neighbouring Li-O_2 technology is far more challenging. Aside from the convoluted ORR/OER mechanism which is not discussed here, the solution-mediated mechanism for the formation and decomposition of Li_2O_2 is a mixed blessing for the electrochemical performance and longevity of Li-O_2 batteries. On one hand, the formation and dissolution of LiO_2 results in large Li_2O_2 crystal that do not passivate the cathode, thus leading to high discharge capacity and low overpotential. On the other hand, prolonged exposure of electrolyte solution and cathode surface to these reactive oxidative species enhances the probability of a nucleophilic attack, proton abstraction, and corrosion by the same species. Moreover, the surface of the cathode needs to remain electrochemically active at all times in order to maintain good ORR/OER activities during cell operation. At the end of the day, very few materials are stable against the highly reactive (su)peroxide species. In other words, the efforts presented thus far to prevent the accumulation of electrolyte & cathode decomposition products is futile unless one seeks an alternative oxygen electrochemical pathway.

Finally, the success of Li-S and Li-O_2 battery heavily relies a functional lithium anode. Different approaches, including interfacial engineering, *in-situ generation* of SEI on lithium anode using electrolyte additive, and *ex-situ embellishment* of lithium with artificial protection layer, have been attempted to protect the lithium surface from any undesired parasitic reaction and to achieve uniform lithium electrodeposition. However, these strategies are only effective for few hundred cycles and their full cells generally operate at a relatively low current density, because the residing problems of each approach remain unsolved. For instance, the plated lithium in nanostructured host materials still suffer from corrosion from the electrolyte and crossed-over materials, whereas electrolyte

additives can be depleted because of the dynamically broken and reconstructed SEI materials. Solid-state materials that physically protect the lithium anode from parasitic reactions can prevent dendrite propagation. Hence they may be the ultimate solution for Li protection and should be explored if they can be synthesized through a more facile route such as a solution-mediated process.

1.7 Thesis Overview

This thesis encompasses a methodological approach in developing new materials for the fabrication of stable and practical Li-S and Li-O_2 batteries, and uncovering the fundamental driving chemistries/principles that drive their success. This document is broadly separated into four sections, and covers eight chapters.

Chapter 1 and **2** discuss the background information necessary to convey the research content in this thesis. **Chapter 1** provides the general introduction to Li metal batteries. A comprehensive literature review on Li-S and Li-O_2 batteries with focus on cathode and electrolytes design is listed. Furthermore, the theory behind the failure modes in lithium anode and approaches to resolves those issues are discussed. **Chapter 2** provides a brief description on the characterization techniques/tools employed in this thesis. It is meant to provide the reader the theories for the experimental methods used throughout this thesis. Detailed information on exactly how each experiment was designed and conducted for each study can still be found in the experimental section of their respective chapters.

Chapter 3, **4**, and **5** focus on the fabrication of stable sulfur cathodes for Li-S

battery. **Chapter 3** uncovers the criteria required for a host material that enables sulfur redox mediation to follow a catenation process. In this work, Dr. Xiao Liang completed the synthesis of V_2O_5-graphene, VO_2-graphene, and Co_3O_4-graphene; He Huang completed the NiOOH synthesis; and I completed the V_2O_3-graphene synthesis. Dr. Liang and I conducted the XPS experiments and analysis together while I completed the majority of CV studies. The rest of the experiments were completed by me under supervision of Dr. Liang. Dr. Liang and I contributed equally on the manuscript drafting. Part of the results presented in this chapter has been published in the follow study: X. Liang, C. Y. Kwok, F. Lodi-Marazno, Q. Pang, M. Cuisinier, H. Huang, C. J. Hart, D. Houtarde, K. Kaup, H. Sommer, T. Brezesinski, J. Janek, L. F. Nazar. Tuning transition metal oxide-sulfur interactions for long life lithium sulfur batteries: the *Goldilocks* principle. *Adv. Energy Mater.*,6:1501636, 2015. Copyright 2015: WILEY-VCH Verlag GmbH & Co. KGaA, Weinheim.

Chapter 4 details the complex surface chemistry that dictates the interaction between MXene and polysulfides. It is shown that MXene entraps polysulfides via a two-step mechanism. The formation of thiosulfate via consumption of hydroxyl surface groups, followed by Lewis acid–base interaction between the exposed Ti atoms and polysulfides is unravelled. It is further shown that interweaving carbon nanotubes between the MXene layers creates a porous, conductive network with high polysulfide adsorptivity, enabling sulfur hosts with excellent performance even at high loading ($5.5\,mg{\cdot}cm^{-2}$). In this work, Dr. Xiao Liang completed XPS and SEM analysis, and synthesized the CNT-Ti_2C and CNT-Ti_3CN material. I completed the XRD and EIS measurement, prepared the CNT-Ti_3C_2 materials, conducted some the preliminary electrochemical data

on the CNT-MXene composite, and assisted Dr. Liang in assembling high sulfur loading cells. I also took part in the manuscript drafting. Part of the results presented in this chapter has been published in the follow study: X. Liang, Y. Rangom, C. Y. Kwok, P. Pang, L. F. Nazar. Interwoven MXene Nanosheet/Carbon-Nanotube Composites as Li-S Cathode Hosts. *Adv. Mater.*,29:1603040, 2017. Copyright 2017: WILEY-VCH Verlag GmbH & Co. KGaA, Weinheim.

Chapter 5 discusses the importance of an appropriate polymeric binder to achieve long-living and high areal capacity Li-S cells. Through a combination of spectroscopic and electrochemical techniques, it is shown that extensive cross-linkage enables the polymeric binder to exhibit a low degree of swelling as well as high tensile modulus and toughness. These attributes are essential to maintain the architectural integrity of the sulfur cathode during extended cycling. The results of this study published and are reproduced with permission: C. Y. Kwok, Q. Pang, A. Worku, X. Liang, M. Gauthier, L. F. Nazar. Impact of the mechanical properties of a functionalized cross-linked binder on the longevity of Li-S batteries. *ACS Appl. Mater. Interfaces*,11:22481-22491, 2019. Copyright 2019: American Chemical Society.

Chapter 6 details the possibility that the stability of Li-O_2 battery is no longer limited once problems caused by peroxides are resolved. By tuning the thermodynamic and kinetic conditions, the formation of a more stable discharge product, Li_2O instead of Li_2O_2, is made possible. In this work, Dr. Xia Chun completed Li_2O solubility measurement, the quantitative chemical measurement, and some of the in-situ mass spectrometry measurement. The remaining work were completed by me under supervision of Dr. Xia. Dr. Xia and I contributed equally on the manuscript drafting. Part

of the results presented in this Chapter has been published in the follow study: X. Xia, C. Y. Kwok, L. F. Nazar. A high-energy-density lithium-oxygen battery based on a reversible four-electron conversion to lithium oxide *Science*,361:777-781, 2018. Copyright 2018: American Association for the Advancement of Science.

Chapter 7 provides a facile, scalable, route to the in-situ formation of a solid-state electrolyte - lithium phosphorus oxynitride (LiPON) - that protects Li anode from dendrite formation and polysulfide corrosion. The LiPON film was synthesized directly on lithium metal by a solution-mediated process, distinguishing itself from the atomic layer deposition methods.

The final chapter, **Chapter 8**. concludes the entire thesis. This chapter provides some final thoughts of Li-S and Li-O_2 batteries, including their future prospective.

Chapter 2

Experimental Theory

A predictable and controlled alteration and application of materials in a battery system require a comprehensive understanding in their physical, chemical, and electrochemical properties. Moreover, identification and quantification of redox species call for rigorously designed analytical procedures. The theories and protocol behind the methods and techniques used in this thesis are outlined below.

2.1 Physical Characterization Methods

2.1.1 Powder X-ray Diffraction

X-ray diffraction is a technique that exploits the wavelength of X-ray (0.01–10 nm) in the same range as the atomic distances in materials to discern their crystal structure and phase composition. All crystalline materials have periodicity in their atomic structures. The X-ray diffracted off from the specific position of these atoms undergoes a

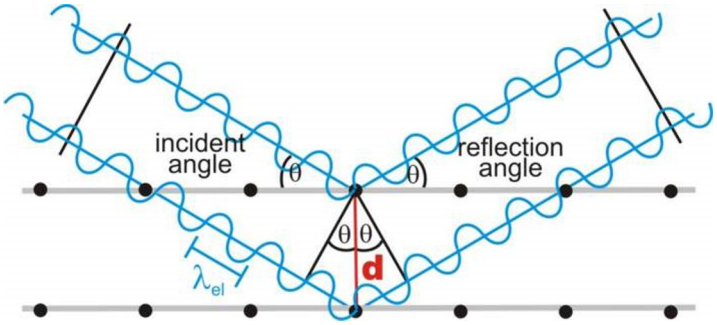

Figure 2.1. X-ray diffraction. Its schematic and the satisfaction of the Bragg equation. Reprinted from [122]

constructive interference in accordance of Bragg's law (**Equation 2.1**):

$$N\lambda = 2d\sin\theta \tag{2.1}$$

where λ and θ are the wavelength and angle of the incident X-ray, respectively; d is the interplanar spacing of the crystal planes; and N is an integer number needed to satisfy Bragg's law. **Figure 2.1** illustrates the condition in which Bragg's law is satisfied. An X-ray, with a known wavelength λ and a particular incident angle θ is scattered off by the atoms centered on a crystal plane d. By geometry, a constructive interference between multiple planes can be established when the optical path length of the scattered X-ray is an integral number equivalent to the incident beam by energy ($N\lambda$). On the contrary, certain crystal planes will not be detected if the diffracted X-ray undergoes destructive interference.

Powder x-ray diffraction assumes all crystal planes have equal probability to be scattered by the incident X-ray. The X-ray source and detector are rotated from $-\theta$ to $+\theta$ with respective to the sample to generate a diffraction pattern containing all

characteristic peaks at the position 2θ. Since the XRD pattern for a particular compound is unique by its crystal structure, the exact phase is identified using a comprehensive database. However, as a structural analysis technique, powder X-ray diffraction does not provide chemical information on the sample.

Scherrer Equation is a handy tool to further estimate the crystal domain size of nanostructed crystal. Using the full-width-half-maximum (FWHM) of the XRD pattern:

$$L = \frac{K\lambda}{\beta \cos\theta} \tag{2.2}$$

where L is the domain size; K is a dimensionless shape factor with a value close to unity; and β is FWHM of the XRD line broadening at a specific angle θ in unit radian.

All XRD patterns in thesis were collected on PANalytical Empyrean X-ray diffractometer operating at 40 kV and 40 mA and using Cu-Kα radiation ($\lambda = 0.154\,05$ nm). The samples were loaded on a zero-background silicon holder. The XRD patterns of all air sensitive samples were collected using a gas-tight sample holder with a Kapton film window.

2.1.2 Electron Microscopy

Electron microscopy is an important characterization tool used in material science to provide high-resolution images. The two main types of electron microscopy used in this thesis are scanning electron microscopy (SEM) and transmission electron microscopy (TEM). As the name suggest, SEM creates an image by detecting the raster-scanned,

scattered electrons, while TEM collects the electrons that are transmitted through the sample to create an image (**Figure 2.2A**). Hence, SEM can provide a 3D mapping on the topology and TEM images are 2D projections of the sample. In either case, their fundamental working principle is similar to that of an optical microscopy, except the incident beam is now electron instead of visible light. High energy electrons (5–20 keV for SEM and 100–400 keV for TEM) are generated through via either thermionic emission or field emission source, which are then focused into a highly collimated beam of a very narrow spot size using magnetic lenses. The above process takes place in an ultrahigh vacuum chamber to avoid electrons from colliding with each other. Finally, the focused beam of primary electrons hit the sample.

The propagation of the primary electron into the sample is limited to several microns because of the random scattering motion and the absorption of primary electrons by

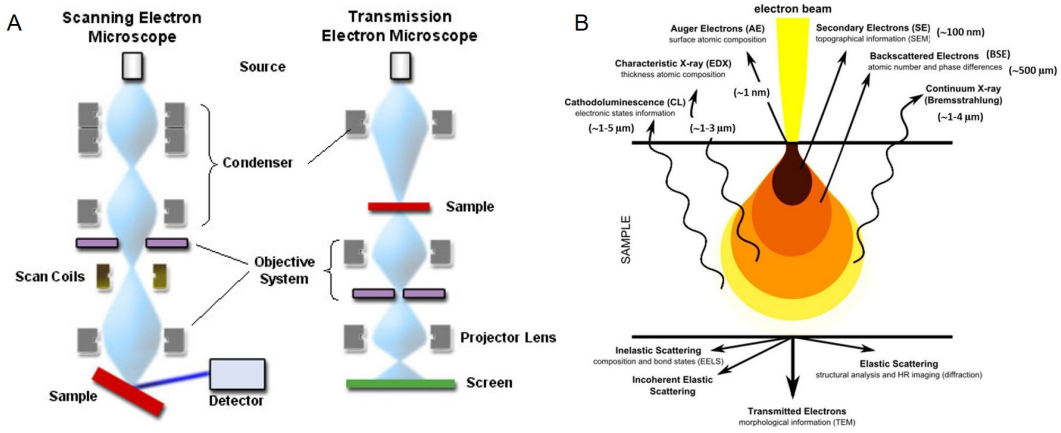

Figure 2.2. Scanning and transmission electronic microscopy. (A) The autonomy of SEM and TEM to showcase the differences in their operating principles. (B) Scheme of the different types of signals (electrons and photons) emitted from different parts of the interaction volume. Reprinted from [123]

the sample's atoms. This gives rise to a tear-shaped interaction volume as shown in **Figure 2.2B** The generation of additional radiations within the interaction volume are the direct result of primary electrons interacting with the electron clouds of the sample's atoms. Hence chemical, structural, and topological information about the specimen can be obtained.

Placing the detectors adjacent to the sample allows the former to pickup secondary electrons, back-scattering electrons and X-ray in SEM. In brief, secondary electrons are generated from the inelastic scattering of the primary electron near the surface of the interaction volume, and these electron provides topology information about the sample. Back scattering electrons, on the other hand, are elastically scattered electrons with higher energy. Because heavier elements can scatter more strongly than lighter ones; back-scattering electron provides excellent elemental contrast. In both cases, a proper electron conduction in the sample is required for the non-primary electrons to escape from the interaction volume. Otherwise, the accumulation of charges around the sample repels the primary beam and causes image distortion. Aside from the scattered electron, the primary electrons injected into the specimen can also generate X-ray that is elemental specific. As a core electron is ejected by the primary electron during inelastic scattering, an electron from the outer shell fills the original orbital and an X-ray is emitted. This technique is known as energy dispersive X-ray spectroscopy (EDX). Because different elements have their own characteristic X-ray, EDX is an excellent tool to identify the geographic location and relative ratio of the elemental composition in a specimen.

With an ultrathin sample ($< 100\,\text{nm}$) and a high-energy electron beam, TEM generates images from collecting the beam transmitted through the specimen. In fact, the

setup and operating principle of a TEM is closer to an optical microscope than SEM. Since the incident electron beam is in high energy, TEM generally provides a much higher resolution image than SEM. Moreover, high-resolution mode (HRTEM) enables direct imaging of the atomic structure of the sample. As the electron penetrates into the sample during imaging, it is attracted by the positive potentials of the atom cores, and thereby channels along the crystallographic lattice. The interaction of the electron across multiple crystallographic lattices thus leads to Bragg diffraction, which is then detected to formulate an image that discerns atomic structure.

All the morphological and elemental analysis of materials was examined on an Zeiss Ultra or LEO 1530 field emission SEM equipped with an EDX detector. Au sputtering may be employed to eliminate surface charging on insulating samples. TEM images were obtained on a JEOL 2010F TEM/STEM or ZEISS Libra 200 MC TEM operated by technicians either at the University of Waterloo or McMaster University.

2.1.3 Infrared and Raman Spectroscopy

Both infrared and Raman spectroscopy utilize the interaction between photon and the molecular vibrations in bonds to provide information on the chemical environment for a particular compound. However, they are based on completely different principles and are often viewed as complimentary techniques.

Infrared spectroscopy exploits on the absorption of a photon energy at the infrared region to excite an electron in a molecule that corresponds to the characteristic of its structure (left, **Figure 2.3**), and Fourier-transform infrared spectroscopy (FTIR) refers

the use of a mathematical function (*Fourier function*) to generate a spectrogram from the raw data. The working principle behind infrared spectroscopy lies within approximating the Hamiltonian of a molecule in its ground state by a harmonic oscillator, where the resonant frequency is dictated by molecular vibrations, as well as the mass of the neighboring atoms and strength of the bond at an equilibrium molecular geometry. Since all of these factors is directly associated with a particular normal mode of motion and bond type, infrared spectroscopy is a powerful technique to identify the existence of a particular bond/interactions. Since FTIR detect bond vibrational change, the molecule itself must exhibit a change in dipole moment in order to be infrared active.

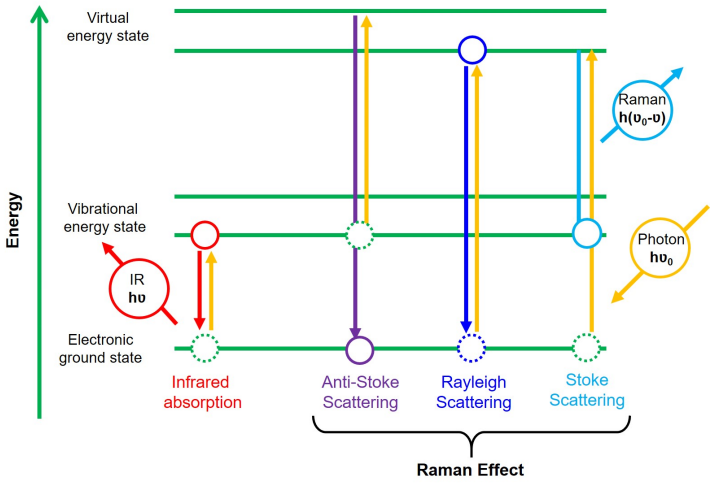

Figure 2.3. Schematic of the orbital transitions in (left) infrared and (right) Raman spectrometry.

Raman spectroscopy (right, **Figure 2.3**), on the other hand, is based on light scattering by the polarizable electron density in a molecule to identify the chemical environment. A focus, monochromatic beam of photon (laser) excites the electron in a molecule from a ground/vibrational states to a virtual energy state for a short period

of time. Upon relaxation, a photon is released if it is elastically scattered (Rayleigh), or inelastically scattered. Rayleigh scattering is trivial to the analysis, and can be filtered by bands; omitting further discussion. Stoke shift takes place if the relaxed state is in a higher energy state than the initial ground state. Conversely, if the final state is lower in energy, the scattered photon will be blue shifted to a higher frequency, which is known as anti-Stokes shift. The energy shift (loss in Stoke and gained in Anti-Stoke) thus must be associated to the vibrational energy of the bond according to the laws of energy conservation. Note though that although Stoke and Anti-Stoke lines are equally distanced from the Rayleigh, only Stoke shifts are measured in Raman spectroscopy because anti-Stoke line is much less intense than the Stokes line. After all, the probably of finding a pre-excited electron orbital is far less likely.

It is worth noting though that while both Raman and IR spectroscopy are considered as a fingerprint technique, prior chemistry knowledge about the sample is necessary for a meaningful analysis. This is because the same chemical environment can have multiple active regions in the spectrogram due to their multiple vibrational modes. FTIR spectra were obtained on a Bruker Tensor 37 spectrometer, and KBr was used as the blending agent. CO_2 and H_2O were removed using the analysis software provided by Bruker. Raman spectra were obtained on a Raman HORIBA HR800 equipped with a green laser ($\lambda = 514$ nm), and the Raman wavelength values were all calibrated using a Si wafer at $520\,\mathrm{cm}^{-1}$.

2.1.4 X-ray Photoelectron Spectroscopy

X-ray Photoelectron Spectroscopy (XPS) is a surface-sensitive technique that characterizes the oxidation state of a particular element in a sample.[124] The working principle is based on the photoelectric effect described by Einstein. An electron if there is a photon (E_{photon}, X-ray in this case) with energy that is grater than its binding energy ($E_{binding}$) to the orbital:

$$E_{binding} = E_{photon} - (E_{kinetic} + \Phi) \tag{2.3}$$

Φ is the work function of the element in the sample and a correction term that accounts for any artifact induced by the instrument. Hence, binding energy is a reflection of the electronic structure of the sample, which provides information on the chemical environment. Aside from oxidation state identification, the intensity ratio between different chemical environments, within the sampe sample, in a spectrogram may also provide an estimation in their relatively quantities. The surface sensitivity in XPS arises from the fact that only photonelectrons that are 1–10 nm deep into the sample can escape and be detected. The rest simply get reabsorbed back to the specimen after ejection despite X-ray beam can penetrate $\sim$1 mm deep.

XPS acquisition in this thesis was performed using a multi-technique ultra-high vacuum Imaging XPS Microprobe system (Thermo VG Scientific ESCALab 250) equipped with a hemispherical analyser (of 150 mm mean radius) by a technician either at the University of Waterloo or University of Toronto. All air-sensitive samples were transported to the XPS chamber under Ar/N_2 environment. All spectra were fitted with Gaussian-

Lorentzian functions and a Shirley-type background using the CasaXPS software. The binding energy values were all calibrated using the C 1s peak at 285.0 eV.

2.1.5 Surface Area, Pore Volume, and Pore Size Determination

The surface area, pore volume, and pore size distribution of sulfur host material were determined on a Quantachrome Autosorb-1 instrument. Samples were degassed at 100 °C under a vacuum line before measurement to remove residual adsorbed water/gas molecules. Both the balance and sample tubes are subject to nitrogen (adsorbate) adsorption/desorption isotherms at 77 K in a liquid nitrogen bath. Any imbalance between the two tubes is caused by the adsorption/desorption of the adsorbate into/out of the the sample, which translates into a differential pressure between the two tubes.[125]

In this thesis, the surface area was determined from the Brunauer-Emmett-Teller method by multi-point analysis and the total pore volume (porosity) was calculated from the volume of nitrogen adsorbed at a relative pressure (P/Po) of 0.99. The pore size distribution was calculated using either Barrett-Joyner-Halenda method or quenched solid state functional theory method.

2.1.6 Thermogravimetric Analysis

Thermogravimetric Analysis (TGA) is an analytical technique that measures the mass changes in a sample as a function of changing temperature. This measurement technique provides valuable information in the physical or chemical properties of the material

in interest. Both the sample and a reference pan are maintained at nearly identical conditions throughout the experiment. This technique is mainly used to determine the weight percentage of sulfur in a sulfur/host composite in this thesis as sulfur sublimes (mass loss) at temperature between 250 and 350 °C. The measurement was conducted on a TA Instruments SDT Q600 at a constant heating rate of 10 °C·min^{-1}.

2.2 Electrochemical Characterization Methods

2.2.1 Galvanostatic Cycling

Galvanostatic cycling refers to an electrochemical method in which a galvanostat station outputs a constant current to an electrochemical device to examine voltage profile change. Here, the current forces the active material in the electrode to be oxidized/reduced as the Li^+ migrates from one electrode to another. In lithium metal batteries, a negative current hence forces the active material in the cathode to undergo reduction, and such process is referred as cell discharge. Conversely, a positive current charges the cell. One complete cycle thus refers to one full discharge procedure followed by a charge procedure. A (dis)charging procedure is considered completed when certain amount of charges (Li^+/e^- pair) has passed from one electrode to another, or a voltage cut-off limit is reached.

Galvanostatic cycling is the most important and universal technique used by battery chemists to examine and understand the electrochemical performance of a battery. On one hand, this technique mimics actual battery operating conditions, where a constant

power is drawn/input into the battery system. On the other hand, it presents a clear metric to gauge the maximum number of Li^+ that can be invoked into/out of the active material. An electrochemical profile thus encompasses the voltage profile change as a function of capacity. Through careful analysis of this profile, one can deconvolute the thermodynamics/kinetic information in the battery system.

Galvanostatic cycling was conducted using a Arbin Instruments BT2000 battery cycler or Bio-logic VMP3 potentiostat/galvanostat cycler at a specified current density or C rate within a specific voltage window detailed in the respective chapters.

2.2.2 Cyclic Voltammetry

Cyclic voltammetry (CV) is another common electrochemical technique to study reaction kinetics and reversibility. The voltage is swept back and forth at a fixed voltage rate and the current is measured. One important information that can be drawn from a CV profile is the onset potential of a half reaction. This is determined by drawing a tangent from the current up(down)swing as the voltage in(de)creases, and then interpolate that line back to when the current equals to zero. Similarly, current maxima is reached when rate of the half reaction is no longer limited by the thermodynamic parameter (i.e. the potential of the electrode) but by material diffusion instead.

All CV experiments detailed in thesis were conducted using a Bio-logic VMP3 potentiostat/galvanostat cycler.

2.2.3 Electrochemical Impedance Spectroscopy

Impedance describes an obstruction of electron flow in a circuit. A high impedance battery typically exhibits characteristics of high overpotential, low specific capacity and energy density achievable, and low rate capability. It is therefore important to examine and understand the origin and evolution of impedance over the course of long-term cycling. The non-linearity nature of battery components calls for electrochemical impedance spectroscopy (EIS). By applying a sinusoidal potential excitation to a system (**Equation 2.4**), the output response is an alternating current that can be analyzed as a sinusoidal function of the same frequency but shifted in phase (**Equation 2.5**) due to the dynamic electrochemical process. Using Euler's relationship and Ohm's law, the expression of the impedance is written as **Equation 2.6**.

$$E_t = E_0 \sin \omega t \tag{2.4}$$

$$I_t = I_0 \sin \omega t + \Phi \tag{2.5}$$

$$Z_\omega = Z_0(\cos \Phi + i \sin \Phi) \tag{2.6}$$

where (ω) is the frequency; Φ is the phase shift; $i = \sqrt{-1}$; and Z_0 is the amplitude of the impedance. Nyquist plot is the most common presentation of such data in the battery field, which plots the real ($Z_0 \cos \Phi$) *vs.* the imaginary ($Z_0 \sin \Phi$)) components of $Z(\omega)$. A typical Nyquist plot encompasses one or more semicircles at high frequencies, followed by an inclined tail known as the Warburg impedance at low frequency. The

mid-high frequency domains provide information on the charge transfer processes at the electrolyte, electrode, and their interfaces, and the Warburg impedance corresponds to the unrestricted ion diffusion to a large planar electrode and may provide information on the overall electrolyte resistance. Because EIS is a technique that characterizes an electrochemical process in terms of electrical measurements, deconvoluting the various signals at different frequencies requires fitting the Nyquist plot with an equivalent electrical circuit model in order to understand the contribution from each interface or bulk process. The circuit elements used to construct the model is a combination of resistor, capacitors, and inductors. Each element in the model should have a corresponding electrochemical meaning in the battery system.

The EIS measurements were carried out on VMP3 potentiostat/galvanostat station with EIS/Z capabilities (Bio-Logic Science Instruments).

2.3 Analytical Chemistry Techniques

2.3.1 Polysulfide Adsorptivity

The polysulfide adsorptivity of any given material can be determined by electrochemically titrating the residual Li_2S_n in solution after contacting with the materials.[126]. Sample solutions were prepared by stirring a known concentration of probe lithium polysulfides, typically Li_2S_4 or Li_2S_6, with a known mass of material in glyme. The mixtures were stirred overnight and the supernatant was collected after centrifugation. Oxidation titiration was then performed on the supernatant to measure the total number of

electron transfer required to oxidize the remaining polysulfide to elemental sulfur. From there, the amount of polysulfide left in the supernatant was determined by extrapolation from a calibration curve, and the polysulfide adsorptivity by a material is ultimately determined by subtracting the starting amount with the adsorbed amount.

Lithium tetrasulfides and hexasulfides powders were synthesized by allowing elemental sulfur to react with lithium triethylborohydride (1 M, Sigma-Aldrich) in anhydrous tetrahydrofuran (THF, Sigma-Aldrich) in the appropriate stoichiometric ratio. The resultant solution was vacuum-dried, followed by a final wash with toluene to isolate the powders. The lithium polysulfide powders were finally collected by vacuum drying in a Büchi vacuum oven at 60 °C.

2.3.2 Differential Electrochemical Mass Spectroscopy

Differential Electrochemical Mass Spectroscopy (DEMS) is a combinatory technique of electro- and analytical chemistry that enables operando gas analysis in electrochemical cells.[127] The fast response time (on the orders of seconds) and high sensitivity for analyte (ppm scale) in mass spectrometry allows the rates of formation of gaseous or volatile products to be quantified in real time. By relating these data to the electrochemical profile of the battery, insights on electrochemical mechanism/process can be elucidated. Since this technique heavily relies on mass spectrometry, its basic principles and operation are discussed below, followed by brief introduction on the home-made DEMS system used in my thesis.

Mass spectrometry is an analytical technique that separates, identifies, and analyzes

the per-vaporized materials based on their mass-to-charge (m/z) ratio. **Figure 2.4A** shows a typical setup for quadrupole mass spectrometer.

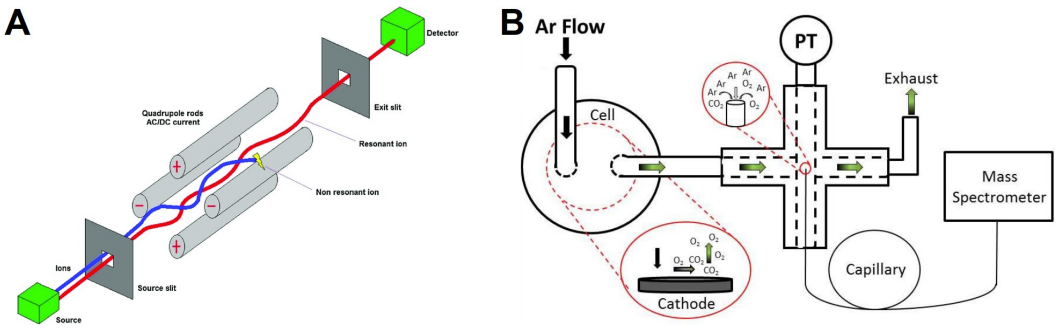

Figure 2.4. Schematics of differential electrochemical mass spectrometry. (A) quadrupole mass spectrometer and (B) design of the in-house DEMS instrument. (A) is reprinted from [128] and (B) is reprinted from [129].

Ionization of the analyte is done by electrons generated from thermionic emission of tungsten filament.

$$AB + e^- \longrightarrow AB^+ + 2e^- \qquad 2.7$$

Beyond the ionizer is a focus plate that pulls the ion-species (analyte) into the quadrupole where they are being analyzed. The analyzer used in this thesis (**Figure 2.4A**) consists of four cylindrical rods that are geographically parallel and electrically set opposite each other. An oscillating electrical field is generated by applying radio frequency with a direct-current offset voltage between one pair of rods versus the other. The lateral forces resulting from this electrical field cause the ions (AB^+) to separate according to their m/z ratio. Only the ions with the proper m/z ratio under a given voltage bias can travel through the entire length of the quadrupole and reach to the detector (represented

by the red-line in **Figure 2.4A**), whereas other ions simply collide with the rods (blue-line). Finally the ions are collected using a continuous dynode electron multiplier that allows the target materials to be detected.

The DEMS system used in thesis is a home-made instrument designed and constructed by Dr. R. Black in the Nazar Research Group. Details on its design can be found in his Ph.D. thesis (**Figure 2.4A**).[129] A continuous flow ($5\,\mathrm{mL{\cdot}min^{-1}}$) of Ar (5.0, Praxair) was used to sweep the gases into the mass spectrometer. Because the direct output of the DEMS instrument is ion current with unit of ampere, a mathematical transformation is needed to convert the raw data to useful information: rate and number of moles of gas. This is done with the aid of a calibration curve, and it assumes that the ion (AB^+) current detected by the mass spectrometer follows a linear regression model with the concentration of target gas in accordance to **Equation 2.8**:

$$I_{MS} = F_{MS} \times \dot{n}_{gas} + b_{MS} \tag{2.8}$$

where I_{MS} is the measured ion current; F_{MS} is the calibration factor ; $\dot{n}_{gas}$ is the rate of gas detected; and b_{MS} is the background. A calibration curve is established by running the target gas at a known but varying concentrations to measure its current response in the mass spectrometer. From there, F_{MS} and b_{MS} are obtained. Since the home-made DEMS instrument measures the flow of gas, rather than the number of moles of gas, the ion current respond is a function of time. With prior knowledge on the total flow rate of the gases into the chamber ($5\,\mathrm{mL{\cdot}min^{-1}}$) and ideal gas law, the gas evolution rate from

the sample can be calculated using **Equation 2.9**:

$$\dot{n}_{gas} = \frac{dn_{gas}}{dt} = \frac{P\dot{V}}{RT} \tag{2.9}$$

where P is the pressure of the outlet gas (1 atm); $\dot{V}$ is the volumetric flow rate of the target gas expressed in $\mathrm{mL{\cdot}min^{-1}}$; R is ideal gas constant ($82.05\,\mathrm{mL{\cdot}atm{\cdot}K^{-1}{\cdot}mol^{-1}}$); and T is the temperature of the gas (298 K). Integrating that equation yields the total number of evolved gas (**Equation 2.10**):

$$n_{gas} = \int_{t_i}^{t_f} \frac{dn_{gas}}{dt} dt \tag{2.10}$$

where t_i and t_f are the initial and final time of measurement, respectively.

All DEMS experiments conducted in this thesis was performed using a modified Swagelok-type cells.

2.3.3 Ultraviolet-Visible Spectroscopy

Ultraviolet-visible spectroscopy is an analytical technique that utilizes a molecule's ability to absorb photon with energy in the UV-vis region (200 - 700 nm) to quantify its concentration in a solution. The principle behind this technique lies within the molecule that contains bonding and non-bonding (n) electrons absorbing the photon energy to enter higher anti-bonding molecular orbitals as shown in **Figure 2.5**. The shorter the energy gap the longer the wavelength of the photon absorbed. The combination of these transitions leads to characteristics absorbance wavelength of the molecule in interest.

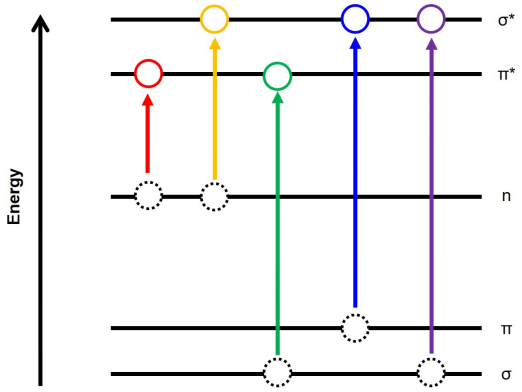

Figure 2.5. Schematic of the orbital transitions in ultraviolet-visible spectroscopy.

With the knowledge of the characteristic absorbance wavelength of a given material, Lambert-Beer law (**Equation 2.11**) is applied to determine the concentration of the absorbing species in solution.

$$A = \epsilon C_{analyte} l \tag{2.11}$$

where A is the measured absorbance which is the fraction of the intensity of light that has been transmitted in comparison with its incident; l is the path length through the sample (1 cm); $C_{analyte}$ is the concentration of the absorbing species; and ϵ is the molar attenuation coefficient. Here, ϵ describes how strongly does a chemical species absorbs a photon energy in order to excite its electron in a given solvent. The Lambert-Beer law thus relates the light attenuation with the analyte concentration. To remove any uncertainty or variability between instruments, a calibration is necessary to relate the specific change of absorbance in response to concentration.

All UV-vis spectra collected in this thesis were performed on a Cary 300 Bio UV-visible spectrometer.

Chapter 3

Elucidating the Thiosulfate/Polythionate Activity in Transitional Metal Oxides

3.1 Introduction

Retarding polysulfide dissolution and controlling Li_2S depositions are keys to achieve stable Li-S cells cycling. As discussed **Section 1.3.1**, sulfur cathodes fabricated with nanostructured porous carbon host materials demonstrate capacity improvement over the first hundred cycles but still suffer from significant capacity decay upon long term cycling due to the weak interaction between polysulfides and carbon. Host materials that interact with polysulfides through chemical interactions are much more promising. Materials including doped-carbon,[36] organic frameworks,[130] and MXene nanosheets[131] show excellent cycling performance because of their strong Lewis acid-base interactions with lithium polysulfides. There exist polar metal oxides/sulfides/borides such as TiO_2,[40] Ti_4O_7,[41] Co_9S_8,[44] MgB_2,[49] etc. that adsorb polysulfides on their inher-

ently sulfophilic surfaces while spatially control the electrodeposition of Li_2S at the end of discharge.

The work by Liang *et al.* in *Nat. Commun.* opened another gateway for polysulfide mediation pathway. First reported on δ-MnO_2 nanosheets, these materials extend the cycling performance of the Li-S battery to more than 2000 cycles.[54] The lack of colouration in the electrolyte upon cycling clearly showcases the soluble polysulfides do not form in significant concentrations. It was proposed in the original report that the operating principle of δ-MnO_2 to retard polysulfide dissolution is not driven by chemisorption but by conversion to thiosulfate/polythionate complex instead. XPS evidence shows that the surface Mn(IV) oxidizes the soluble S_n^{2-}, thereby decorating the MnO_2 nanosheet surfaces with functional $S_2O_3^{2-}$ groups. The thiosulfate anchors higher-order polysulfides (S_n^{2-}, $n \geq 4$) by catenating them into the S-S bond of the thiosulfate ($S_2O_3^{2-}$) to create intermediate surface-bound polythionate complexes (O_3S_2-S_{n-1}-S_2O_3) as shown in **Figure 3.1**. The sulfur catenation process locks the polysulfides on MnO_2, providing an interface for Li_2S electrodeposition. Because the surface polythionate complex can be reversibly recovered on oxidation, evidenced by XPS, and it remains electrochemical active in the subsequent charge procedure.

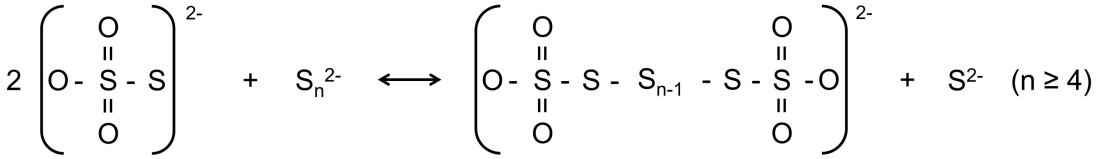

Figure 3.1. Schematic equation of the thiosulfate-polysthionate conversion.

Clearly, the generation of thiosulfate species on the surface of the host materials by

reaction with lithium polysulfides is vital to the retention of the latter species at the cathode upon cycling. In this chapter, I explore the surface science and electrochemistry of transition metal oxides that determine the metrics necessary to activate thiosulfate formation, and provide new insights of the surface reactivity. It is speculated that the principle which drives thiosulfate formation (and generation of a polythionate complex) is the redox potential of the transition metal oxide hosts compared to that of the Li_2S_n, where the latter lies in the range of 2.1 V $< E^\circ \leq$ 2.4 V.[13] Materials with too low of potentials do not react and serve only to bind polysulfides via typical chemisorption; and those with potential above certain limit over-oxidize polysulfide to form the electrochemical inactive sulfate surface group. To prove this concept and establish the *Goldilocks* principle, Li_2S_4 - a probe specie that represents a polysulfide of average depth of discharge - is allowed to react with a wide variety of commercial and home-made bulk metal oxides of varying redox potentials, as measured by CV. XPS studies are then conducted to determine whether reaction occurred, and what surface species resulted. To further correlate this finding to Li-S cell performance, several selected high-surface area metal oxides were utilized as sulfur cathodes. Unsurprisingly, only the metal oxides that are within the optimal range displayed very good cycling performance, whereas oxides that fall outside the targeted redox range showed inferior Li-S cell performance.

3.2 Experimental Methods

3.2.1 Preparation of Vanadium Oxide-Graphene

A series of graphene supported vanadium oxides were prepared as sulfur host materials by first synthesizing a generic VO_x, ($2 < x \leq 2.5$) material on graphene using hydrothermal technique followed by annealing. Briefly, 50 mg of graphene (ACS Material) was dispersed in ethanol by sonication, and then 4 mL of vanadyl triisopropoxide (Sigma-Aldrich) was added while the mixture was stirred. The suspension was sealed in an autocleave and transferred to a thermostatted oven at 160 °C for 24 hours. The black-coloured product was washed in ethanol, dried at 60 °C overnight, and finally annealed at 300 °C in air for 30 min (V_2O_5-graphene) or 400 °C in Ar for 10 h (VO_2-graphene) or 600 °C in H_2/Ar for 4 h (V_2O_3-graphene).

Sulfur was melt-diffused into each respective vanadium oxide-graphene materials with 75 wt. % of sulfur by mixing the host materials with elemental sulfur and then heated under ambient atmosphere at 160 °C for 12 hours.

3.2.2 Preparation of Co_3O_4-Graphene

Graphene supported cobalt trioxide was also synthesized in a similar fashion as that of the vanadium oxide, except the precursor is cobalt(II) acetate.[132] Here, 4.8 mL of 200 mM cobalt(II) acetate (ACS, Sigma-Aldrich) was added dropwise into 96 mL of a predispersed graphene ethanol suspension, followed by the addition of 4.8 mL of water.

The suspension was transferred to a 120 mL autoclave and heated at 80 °C for 10 hours while vigorously being stirred. The autoclave was then heated at 150 °C for three hours in an oven. The product was washed with ethanol and water, and further annealed at 300 °C for 4 h in air to yield the final product.

3.2.3 Preparation of NiOOH

NiOOH was prepared by a one-pot hydrothermal method.[133] Namely, 20 g of nickel sulfate hexahydrate was dissolved into 50 mL of DI water at room temperature. In a separate beaker, 9 g of NaOH pellets was dissolved in a 50 mL of sodium hypochlorite solution, and this solution was added dropwise to the nickel sulfate solution where a black precipitate is afforded. The final product was filtered, washed with water, and vacuum dried.

3.2.4 Preparation of Li_2S_4 Contact Experiment

For this comprehensive XPS study: NiO, CoO, Co_3O_4, Cu_2O, and CuO were purchased from Sigma-Aldrich, while NiOOH, MnO_2, V_2O_5, VO_2, and V_2O_3 were synthesized in the lab as described above. All metal oxide materials were vacuum dried at 80 °C for 24 hour prior to use. In an Ar-filled glovebox, 20 mg metal oxide and 1 mmol Li_2S_4 were stirred in 5 mL glyme for 6 hours. The powder for XPS analysis was collected by centrifugation followed by drying under vacuum overnight. Only the peak positions of the lower binding energy components of the sulfur $2p_{3/2}$ and metal $2p_{3/2}$ spin orbital doublets in the XPS spectrum are given, following convention.

3.2.5 Determining the Onset Potentials For Metal Oxides

The onset redox potentials for each metal oxides were identified using cyclic voltammetry. To prepare the electrode, each metal oxide was mixed with Super P and PVDF at a weight ratio of 8:1:1 in dimethylformamide (DMF) solvent. The slurry was casted on P50 (Fuel Cell Earth) carbon paper and dried at 60 °C overnight. Coin cells were assembled with Li foil as a counter and reference electrode using 1 M LiTFSI in an equivolume of DOL/DME electrolyte. The CV tests were collected at a scan rate of $0.05\,\mathrm{mV{\cdot}s^{-1}}$.

3.2.6 Electrochemical Studies on Li-S Coin Cells

Sulfur electrodes were prepared by casting a DMF slurry containing the S-metal oxide-graphene, Super P and PVDF in 8:1:1 weight ratio on a P50 carbon paper. The sulfur loading on the electrodes were between 1.2 and 1.5 $\mathrm{mg{\cdot}cm^{-2}}$. The electrodes were dried in a 60 °C oven overnight prior to use. The coin cells (2325) were assembled by using the conventional Li-S electrolyte, and Li as the counter/reference electrode in an Ar-filled glovebox.

3.3 Redox Reactions between Lithium Polysulfides and Metal Oxides

Metal Oxides with a Low Redox Potential

Co_3O_4 falls into this category, providing an illustrative example. Its redox potential of ~1.11 V *vs.* Li/Li^+, determined by CV measurement (**Figure 3.2A**), lies below the polysulfide window of $2.1 \leq E^\circ \leq 2.4$ V *vs.* Li/Li^+. Hence, it cannot engage in a redox reaction with lithium polysulfides. Accordingly, the ratio of the Co^{3+} and Co^{2+} peaks in its XPS Co 2p spectrum (**Figures 3.2B** and **3.2C**) remains unchanged upon contact with Li_2S_4, and the peaks in the sulfur 2p core spectra show only the features of the adsorbed polysulfide (**Figure 3.2D**). Li_2S_4 exhibits the expected 1:1 ratio of *bridging* (S_B^0, 163.7 eV) and *terminal* (S_T^{-1}, 161.9 eV) sulfur environment.[41, 54, 131] Other metal oxides (NiO and CoO) also do not undergo reaction with Li_2S_4 to form thiosulfate/polythionate because their redox potentials are too below the desired 2.1 V (**Figure 3.2**). The results on the XPS and CV studies are summarized in **Table 3.1**. It is worth noting though that this result does not necessary mean these metal cannot participate other mechanisms to entrap polysulfides at the cathode. In principle, Cu_2O and V_2O_3 should also fall into this category, but the ease of oxidation means that their surfaces are usually covered by a higher native oxide as discussed in the following section.

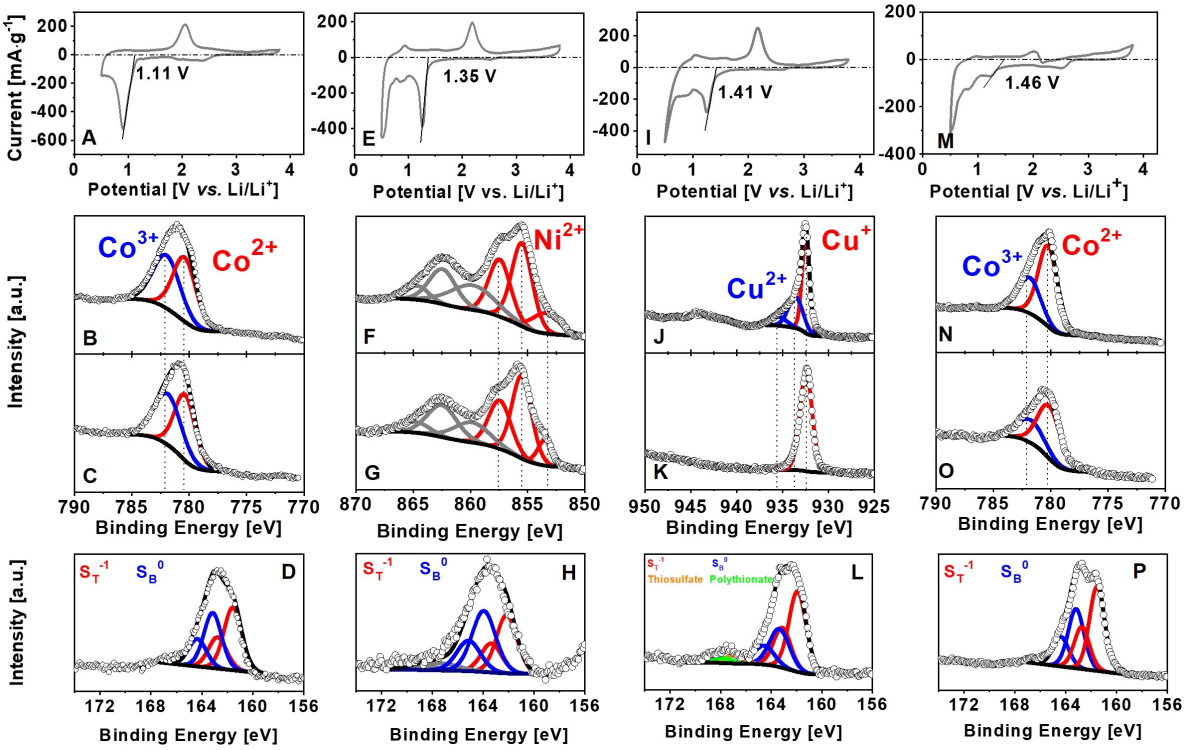

Figure 3.2. Metal oxides incapable of engaging the thiosulfate/polythionate formation. CV profiles of (A) Co_3O_4; (E) NiO; (I) Cu_2O; and (M) CoO. XPS spectra of these materials and the composite recovered from their interactions with Li_2S_4 for (B-D) Co_3O_4; (F-H) NiO; (J-L) Cu_2O; (N-P) CoO. (B) Co 2p in Co_3O_4; (C)Co 2p in Co_3O_4-Li_2S_4; and (D) S 2p in Co_3O_4-Li_2S_4. (F) Ni 2p in NiO; (G) Ni 2p in NiO-Li_2S_4; and (H) S 2p in NiO-Li_2S_4. (J) Cu 2p in Cu_2O; (K) Cu 2p in Cu_2O-Li_2S_4; and (L) S 2p in Cu_2O-Li_2S_4. (N) Co 2p in CoO; (O) Co 2p in CoO-Li_2S_4; and (P) S 2p in CoO-Li_2S_4. Due to the surface oxidation of CoO to Co_2O_3, the XPS spectra for CoO shows both Co^{3+} and Co^{2+} environment. Similarly, the surface oxidation of Cu_2O results in XPS spectra for Cu_2O showing both Cu^{2+} and Cu^{+}.

Metal Oxides that Form Thiosulfate via Redox

These encompass materials where concomitant reduction of the surface metal oxide and oxidation of Li_2S_4 occurs (**Table 3.1**, materials between the two the dotted lines). Both MnO_2 and graphene oxide demonstrate this behavior, as previously reported.[54] The re-

dox potential of CuO, 2.53 V (**Figure 3.3A**) lies just at the lower end of the target range. Its XPS Cu 2p spectrum shows only Cu^{2+} as a classic multiplet (**Figure 3.3B**).[134, 135] Upon contact with Li_2S_4, the surface is partially reduced to Cu^+ (**Figure 3.3C**). This occurs in concert with the oxidation of sulfur species to thiosulfate (167.2 eV), which can be expressed as:

$$10Cu^{II}O + Li_2S_4 \longrightarrow 4Cu_2^{I}O + Cu_2^{I}(S_2O_3) + Li_2S_2O_3 \qquad 3.1$$

Polythionate is likely formed by subsequent reaction of polysulfides with the anchored thiosulfate group (**Equation 3.1**), which appears in the S 2p core spectrum at 168.2 eV (**Figure 3.3D**) along with the bridging and terminal sulfur contributions from the lithium polysulfides.[41, 54, 131] It worth noting that species such as tetrathionate may also form via direct oxidation of polysulfides with the host, but it would be indistinguishable from polythionate (and this would not explain the presence of the thiosulfate groups on the surface). The residual Li_2S_n are due to incomplete reaction, in part because the surface area of the bulk metal oxide is low. VO_2, with a redox potential of 2.79 V (**Table 3.1**) undergoes the same redox upon contact with Li_2S_4. It exhibits a lower Li_2S_n fraction (**Table 3.1**) - hence more complete reaction - owing to its higher surface area, as described fully in the following section.

Metal Oxides with a High Redox Potential

When oxides exhibit a very high redox potential > 3.4 V *vs.* Li/Li^+ - potential above the target window - oxidation of Li_2S_n to higher oxidation states of sulfur is predicted. This

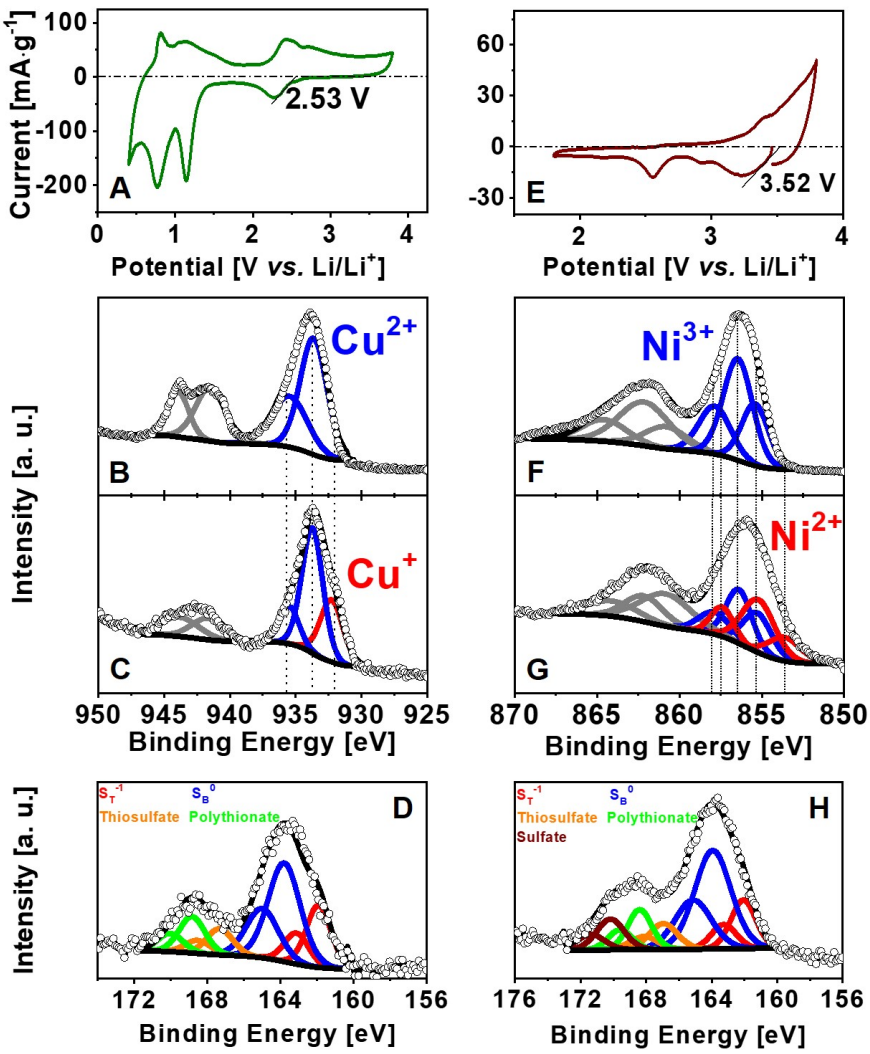

Figure 3.3. Metal oxides capable of transforming polysulfides to thiosulfate/polythionate. CV profiles of (A) CuO and (E) NiOOH. XPS spectra of these materials and the composite recovered from their interactions with Li_2S_4 for (B-D) CuO and (F-H) NiOOH. (B) Cu 2p in CuO; (C)Cu 2p in CuO-Li_2S_4; and (D) S 2p in CuO-Li_2S_4. (F) Ni 2p in NiOOH; (G)Ni 2p in NiOOH-Li_2S_4; and (H) S 2p in NiOOH-Li_2S_4. The Cu 2p and Ni 2p spectra appear as a classic multiplet arising from *shake-up* satellite peaks.

is demonstrated by nickel peroxide and V_2O_5 (**Table 3.1**). NiOOH is best represented as $Ni_2O_3 \cdot 2\,H_2O$ or β-$NiOOH \cdot H_2O$.[136, 137] CV measurement on the material indicates this hydroxyoxide has a redox potential of 3.52 V *vs.* Li/Li^+ (**Figure 3.3E**). The main peak of the Ni $2p_{3/2}$ XPS multiplet spectrum exhibits a binding energy of 856.7 eV, indicative of Ni (III) environment (**Figure 3.3F**).[138] Contact with Li_2S_4 results in reduction of the metal (**Figure 3.3G**), similar to Cu^{II} to Cu^{I} in CuO. The low surface area of NiOOH, as in the case of CuO ($\sim$20 $m^2 \cdot g^{-1}$), means that only partial reduction is observed. Owing to the very high redox potential of the Ni^{3+}; however, this is accompanied by oxidation of lithium polysulfides not only to thiosulfate/polythionate, but also to sulfate (SO_4^{2-} at 170.2 eV; S 2p XPS spectrum in **Figure 3.3H**). The oxidation of sulfur to its highest oxidation state (S^{6+} in sulfate) is driven by the high oxidation potential of the metal. Oxides that can oxidize sulfur have high polysulfide adsorptivity and exhibit stabilized cycling.[126] The formation of sulfate is triggered by high redox potential metal oxides; however, has detrimental effects on the long term performance of Li-S batteries. This will be demonstrated in the following section for V_2O_5 (redox potential of about 3.40 V, **Table 3.1**).

Table 3.1. Redox potentials of metal oxides and the valence change of metal and sulfur upon Li_2S_4-metal oxide reaction, measured from XPS and CV experiments.

Metal Oxide	Redox Potential [V]	Metal Valence Change	Fraction in S 2p spectra [%]			
			Polysulfide 161.9/163.7 eV	Thiosulfate 167.2 eV	Polythionate 168.2 eV	Sulfate 170.2 eV
Co_3O_4	1.11	-	100	-	-	-
V_2O_3	1.11	Surface $V^{4+} \rightarrow V^{3+}$	76	10	14	-
NiO	1.35	-	100	-	-	-
Cu_2O	1.41	Surface $Cu^{2+} \rightarrow Cu^{+}$	89	6	5	-
CoO	1.46	-	100	-	-	-
CuO	2.53	$Cu^{2+} \rightarrow Cu^{+}$	74	11	15	-
VO_2	2.79	$V^{4+} \rightarrow V^{3+}$	67	24	9	-
MnO_2	3.05	$Mn^{4+} \rightarrow Mn^{3+,2+}$	54	20	26	-
V_2O_5	3.40	$V^{5+} \rightarrow V^{4+,3+}$	32	38	22	8
NiOOH	3.52	$Ni^{3+} \rightarrow Ni^{2+}$	65	10	13	12

3.4 High Surface Area Metal Oxides: Maximizing Contact for Cathodes

A high surface area modification of each of the three different classes of metal oxides were supported on graphene (**Figure 3.4**), in order to maximize the interaction of the metal oxide and polysulfides in practical Li-S cells, and to confirm the Goldilocks concept. Three nanocrystalline vanadium oxides, V_2O_5, VO_2, and V_2O_3 were synthesized by annealing a precursor - VO_x supported on graphene (VO_x-graphene, x = 2 - 2.5) - in different atmospheres to control the oxidation state.[139] The precursor was prepared by hydrothermal hydrolysis of vanadyl isopropoxide in the presence of graphene. The as-synthesized VO_x-graphene has a surface area of $103\,m^2 \cdot g^{-1}$ as determined by the N_2 isotherm (**Figure 3.5A**). Annealing the VO_x-graphene materials at 400 °C in Ar resulted in VO_2-graphene, while at 300 °C in air forms V_2O_5-graphene; and 600 °C in H_2/Ar for V_2O_3-graphene. HRTEM (**Figures 3.4E** to **3.4G**) and XRD patterns (**Figure 3.5B**)

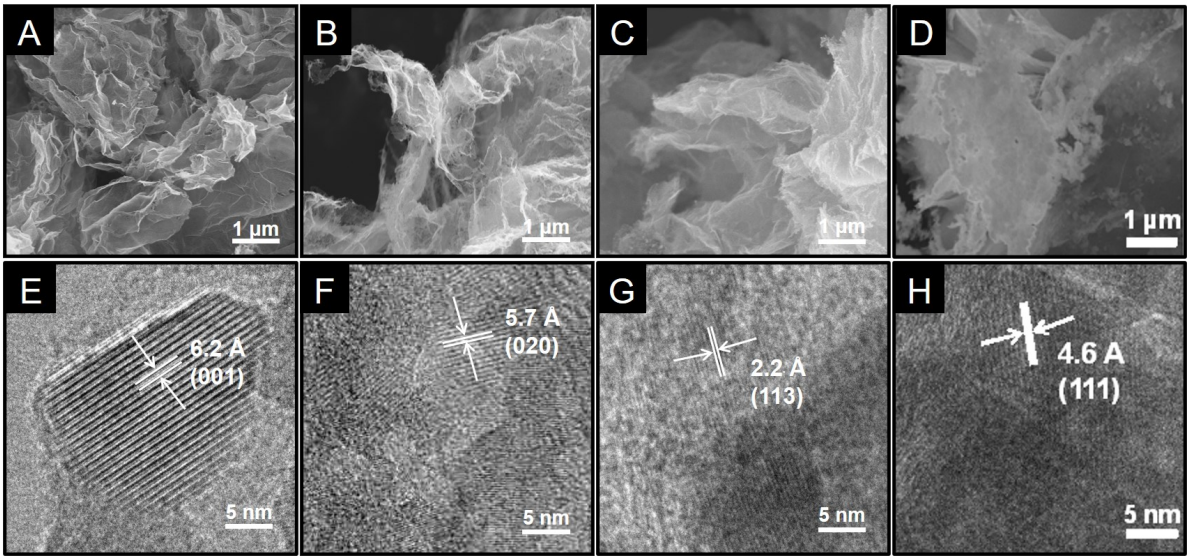

Figure 3.4. SEM and TEM analysis of the graphene-supported metal oxide materials SEM images of (A) VO_2-graphene; (B) V_2O_5-graphene; (C) V_2O_3-graphene; and (D) Co_3O_4-graphene. HRTEM images of (E) VO_2-graphene showing VO_2 nanocrystals, with index to the (001) lattice planes of the oxides; (F) V_2O_5-graphene showing V_2O_5 nanocrystals, with index to the (020) lattice planes of the oxides; (G) V_2O_3-graphene showing V_2O_3 nanocrystals, with index to the (113) lattice planes of the oxides; (H) Co_3O_4-graphene showing Co_3O_4 nanocrystals, with index to the (111) lattice planes of the oxides.

confirmed that the targeted processing conditions resulted in the formation of VO_2, V_2O_5 or V_2O_3 nanocrystals on the graphene sheets. The surface oxidation states of these materials were determined by XPS analysis (**Figure 3.6**). The V 2p spectrum of VO_2 was fit by V^{4+} at 516.3 eV, with a small contribution (∼28 %) of V^{3+} at 515.0 eV.[140] The major surface component on V_2O_5-graphene is V^{5+} (517.6 eV) with a small V^{4+} contribution.

Interestingly, the V_2O_3-graphene contains considerable V^{4+} on its surface owing to its extreme oxygen sensitivity (**Figure 3.6J**). Thus, although it exhibits a low bulk

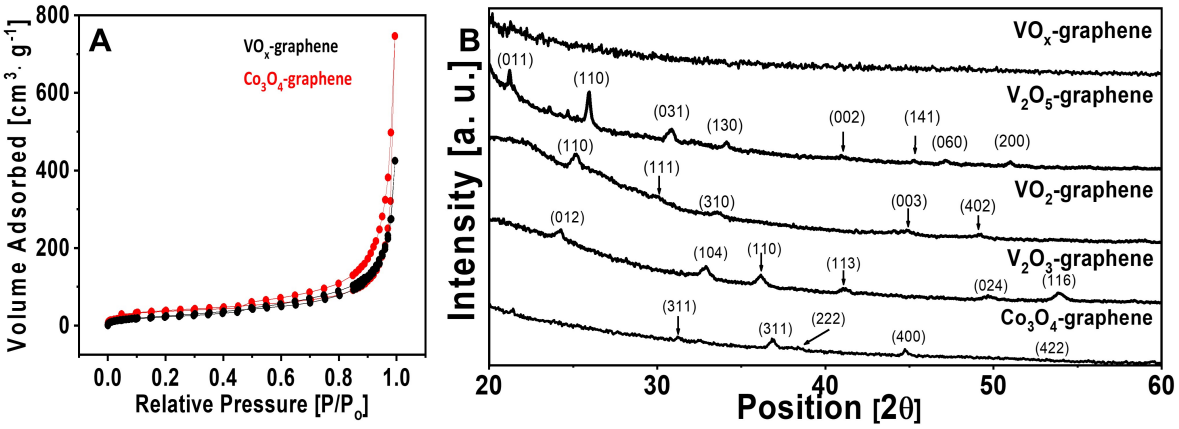

Figure 3.5. Surface area and XRD analysis of the metal oxide-graphene materials. (A) N_2 absorption/desorption isotherms of VO_x-graphene and Co_3O_4-graphene from which the BET surface area was calculated. (B) XRD patterns of VO_x-graphene, VO_2-graphene, V_2O_5-graphene, V_2O_3-graphene, and Co_3O_4-graphene. All patterns are indexed to their respective JCPDS files.

redox potential of 1.11 V (**Figure 3.6I**; note that the small feature at 2.5 V is related to the reduction of native VO_2), the material behaved like VO_2 with respective to surface reactivity with Li_2S_4 (**Figures 3.6K** and **3.6L**). This result also accounts to why Cu_2O, low redox potential metal oxide, is also able to convert polysulfides to thiosulfate/polythionate (**Figures 3.2I** to **3.2L**). A search for an alternative low redox potential (< 2.4 V) oxide for the full cell electrochemical studies (next section) suggested Co_3O_4, which exhibits the same bulk redox potential as V_2O_3 but lacks a higher-oxide native film owing to the large potential jump in accessing Co^{4+}. Supported Co_3O_4 was synthesized by the hydrolysis of cobalt acetate in the presence of graphene.[132] SEM and HRTEM images also show Co_3O_4 nanocrystals uniformly anchored on the graphene surface (**Figures 3.4D** and **3.4H**). BET analysis reveals a high surface area of 120 $m^2 \cdot g^{-1}$

(**Figure 3.5A**), very comparable to that of the supported vanadium oxides. The air stability of Co_3O_4-graphene demonstrated by XPS (**Figure 3.6N**) shows a $Co^{3+/2+}$ ratio exactly the same as that of the bulk oxide (**Figure 3.2B**).

The redox potential of these supported vanadium oxides determined by CV measurements (**Figures 3.6A**, **3.6E** and **3.6I**), are summarized in **Table 3.1**, along with that of Co_3O_4−graphene (**Figure 3.6M**). To confirm the reactivity of these high surface area oxides, they were also contacted with Li_2S_4. The S 2p spectrum of the Co_3O_4-graphene (**Figure 3.6P**) Li_2S_4 material exhibits no change, as did that of the bulk Co_3O_4 (**Figure 3.2D**). For VO_2, the expected changes were observed in the XPS spectra (**Figure 3.6H** and **Table 3.1**). A considerable amount (28 %) of V^{4+} on the surface is reduced to V^{3+}, and the average valence decreases from +3.7 to +3.4 (**Figures 3.6F** and **3.6G**). This corresponds to the concurrent appearance of thiosulfate/polythionate in **Figure 3.6H**. V_2O_5 too shows a dramatic reduction of the vanadium sites, evidenced by the disappearance of the V^{5+} spin orbit doublet and strong increase in V^{4+} and V^{3+} contributions (**Figures 3.6B** and **3.6C**). Quantification by integration reveals a decrease in the surface valence from +4.8 to +3.4, accompanied by thiosulfate/polythionate in the S 2p spectrum (**Figure 3.6D**). The presence of inactive sulfate (S^{6+}, as for NiOOH described earlier) indicates that V_2O_5 oxidizes the lithium polysulfides beyond thiosulfate.

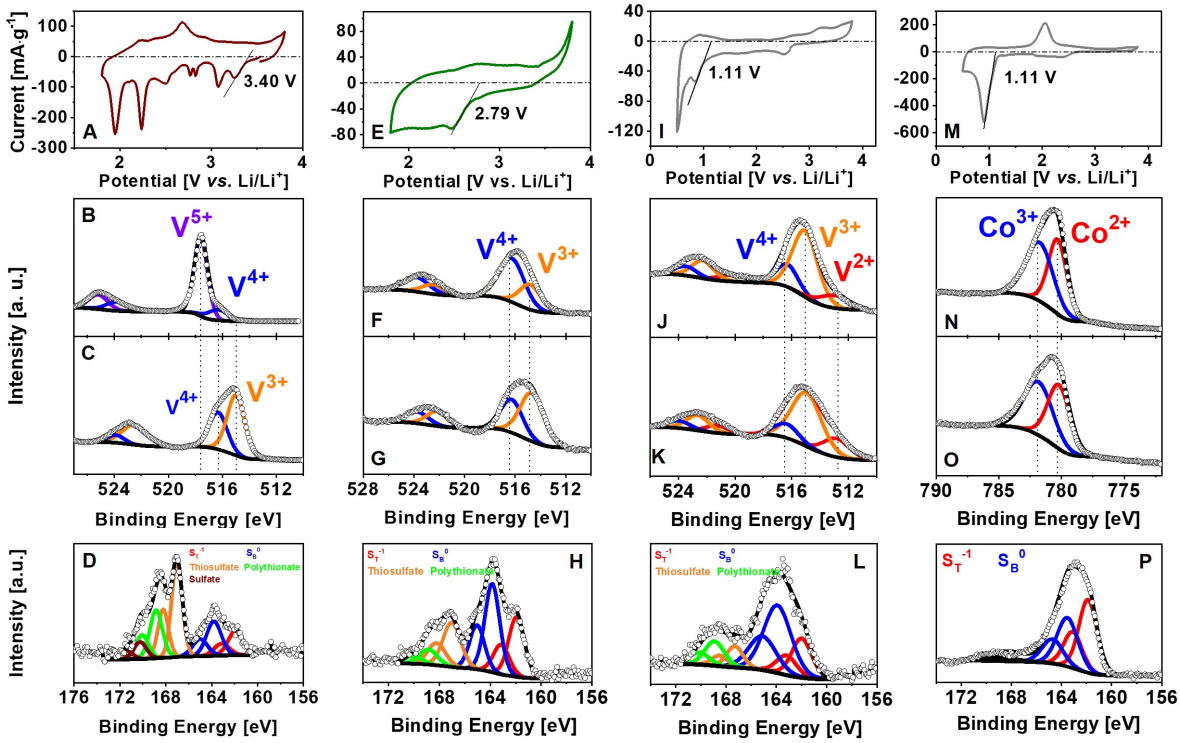

Figure 3.6. Surface chemistry of graphene-supported metal oxides with polysulfide. CV profiles of (A) V_2O_5; (E) VO_2; (I) V_2O_3; and (M) Co_3O_4. XPS spectra of these materials and the composite recovered from their interactions with Li_2S_4 for (B-D) V_2O_5-graphene; (F-H) VO_2-graphene; (J-L) V_2O_3-graphene; (N-P) Co_3O_4-graphene. (B) V 2p in V_2O_5; (C) V 2p in V_2O_5-Li_2S_4; and (D) S 2p in V_2O_5-Li_2S_4. (F) V 2p in VO_2; (G) V 2p in VO_2-Li_2S_4; and (H) S 2p in VO_2-Li_2S_4. (J) V 2p in V_2O_3; (K) V 2p in V_2O_3-Li_2S_4; and (L) S 2p in CoO-Li_2S_4. (N) Co 2p in Co_3O_4; (O) Co 2p in Co_3O_4-Li_2S_4; and (P) S 2p in Co_3O_4-Li_2S_4.

Overall, the reaction between metal oxides and lithium polysulfides can be divided into three categories based on the *Goldilocks* principle summarized schematically in **Figure 3.7**. With this classification, one can narrow the scope and target those metal oxides that can form thiosulfate/polythionate surface species. This include oxidized carbonaceous materials, such as graphene oxides that operate by a similar mechanism as shown by Liang *et al.* in his original report.[41] Such materials strongly inhibit polysulfide diffusion into the electrolyte and play a key role in stabilizing capacity over ultralong cycling, as demonstrated in the next section.

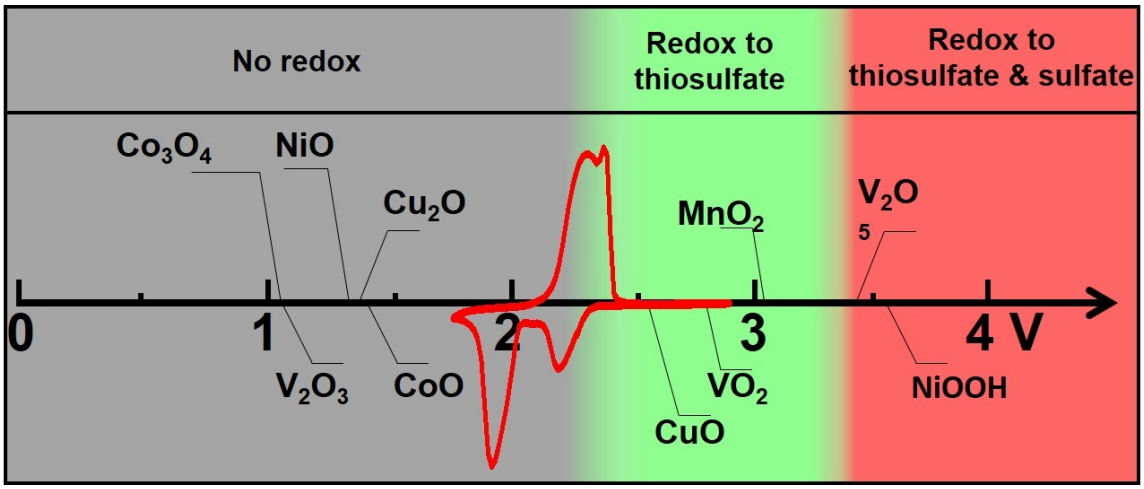

Figure 3.7. Surface chemical reactivity of different metal oxides with Li_2S_n as a function of redox potential versus lithium. Superimposed in red is a cyclic voltammogram of a typical Li-S battery.

3.5 Metal Oxide Behaviour in Li-S Cells: Proof of Concept

To test the theory proposed above, and probe the effects of redox potential of the transition metal oxide host on the electrochemical performance of Li-S cells, elemental

sulfur was melt diffused into each metal oxide-graphene host material via heat treatment at 160 °C for 12 h, with a target composition of 75 wt. % S in the composites. SEM and EDX analysis in **Figure 3.8** reveal that the sulfur was uniformly distributed on the metal oxide host materials. TGA confirmed the sulfur loading (**Figure 3.8D**) was 75 wt. %. Sulfur cathodes based on these metal oxides were subjected to cycling in coin cells. During the first activation cycle at a current rate of C/20, S-Co_3O_4-graphene, S-VO_2-graphene, and S-V_2O_5-graphene exhibit discharge capacities of 1141, 1180, and 1205 $mA{\cdot}h{\cdot}g^{-1}$, respectively (**Figure 3.9A**). All cells show a typical two-plateau discharge curve corresponding to the successive reduction of sulfur, and a charge curve showing re-oxidation of Li_2S_n to sulfur.[13] Cells with S-V_2O_5-graphene positive electrodes display reversible capacity above 2.4 V (i.e. above the Li_2S_n redox) and below 2.0 V (i.e. below Li_2S_n redox) during discharge and charge. This is due to the lithiation/delithiation of the V_2O_5 host, which is consistent with the CV measurements in the absence of sulfur.

Long-term cycling at C/2 provides insight into the effects of the formation of thiosulfate/polythionate and sulfate on the performance of the cells. Over the first 150 cycles, the cells based on S-V_2O_5-graphene and S-VO_2-graphene exhibit similar capacity retention of 76 % and 74 % (**Figure 3.9B**). However, their behaviour diverged after this point The more pronounced capacity decay on continued cycling of S-V_2O_5-graphene is ascribed to the gradual consumption of active polysulfides and formation of inactive sulfate groups by the electrochemically recovered higher vanadium species (i.e. +4.5) during cells that were charged to 3 V. This is revealed in the difference in the capacity of the two discharge plateaus of the S-VO_2- and S-V_2O_5-graphene electrodes at the 140^{th} cycle. When the polysulfides are further oxidized to the electrochemically inert

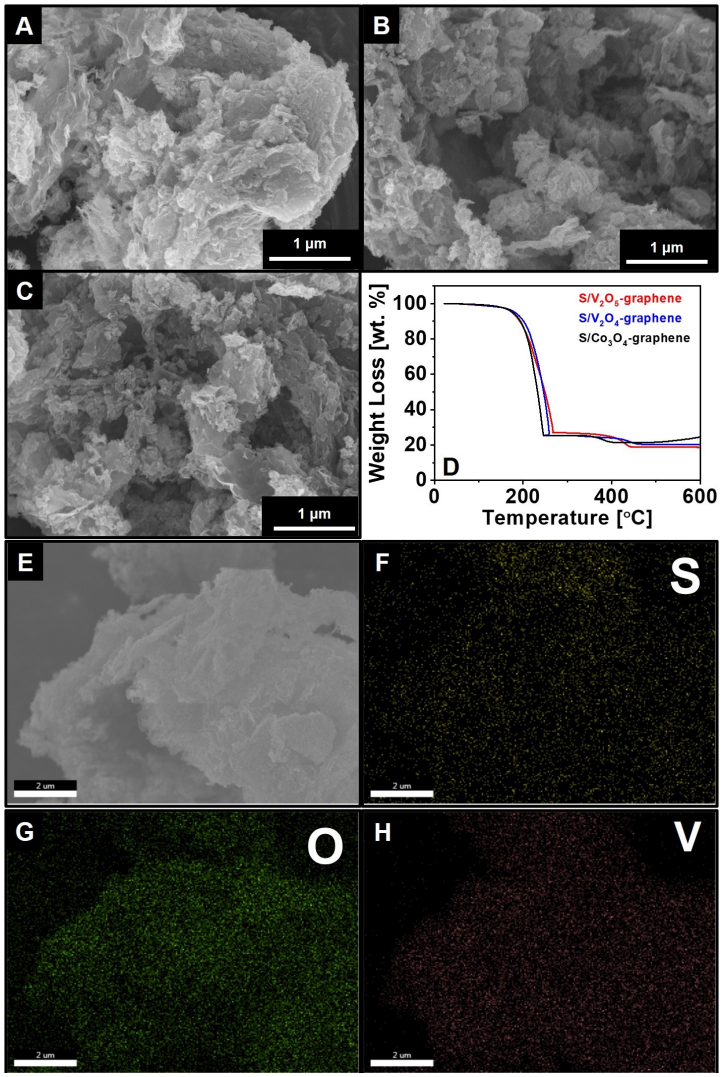

Figure 3.8. Physical characterization of the sulfur infused graphene-supported metal oxides (S-M_xO_y-graphene). SEM images of (A) S-V_2O_5-graphene; (B) S-VO_2-graphene, (C) S-Co_3O_4-graphene. (D) TGA profiles of the same materials, showing a sulfur content of ∼75 wt .%. EDAX analysis of S-VO_2-graphene. (E) SEM image and elemental mapping of (F) S; (G) O; and (H) V.

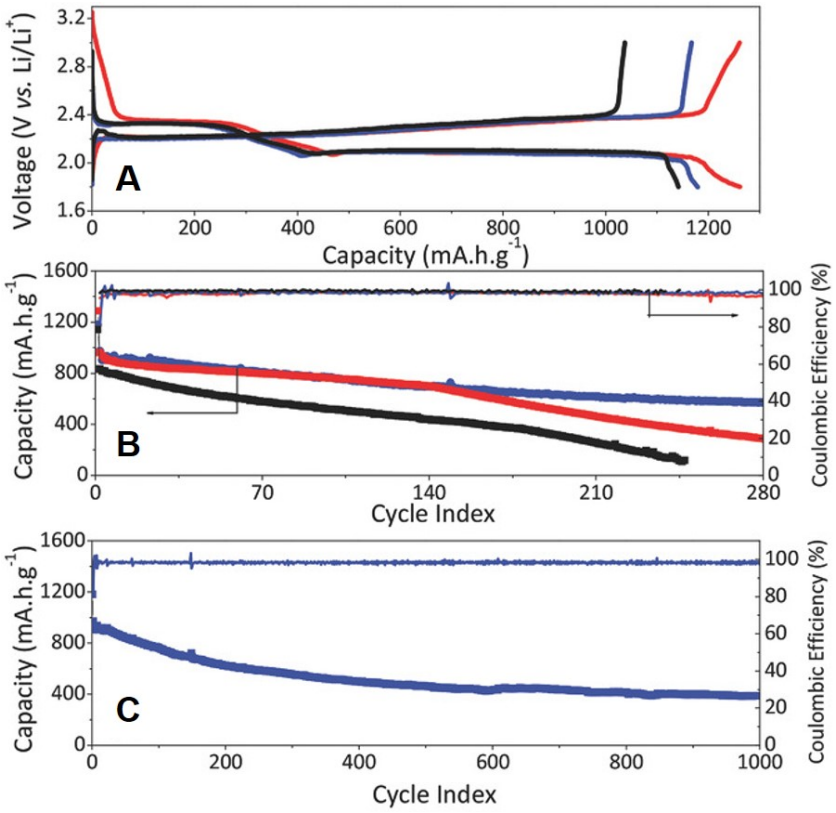

Figure 3.9. Electrochemical performance of the Li-S cells fabricated with the metal oxide-graphene materials. (A) Electrochemical profile of the sulfur cathodes fabricated with V_2O_5-graphene (red), VO_2-graphene (blue), and Co_3O_4 (black) at C/20, (B) comparison of the cycling performance at C/2. (C) long term performance of Li-S cells using VO_2-graphene as host material at C/2

sulfate species by V_2O_5, the accumulation of the electrochemical inactive sulfate groups will block the host surface and lead to poor long term cycling performance. The S-VO_2-graphene electrode stabilizes at 400 $mA{\cdot}h{\cdot}g^{-1}$ up to 1000 cycles corresponding to a decay rate of 0.058 % per cycle (**Figure 3.9C**). In contrast, under exactly the same cell conditions, Co_3O_4-graphene exhibits significant polarization after 200 cycles and faster decay

(0.34 % per cycle over 250 cycles) due to the absence of thiosulfate/polythionate groups (**Figure 3.9B**). Unlike S-VO_2-graphene, the Co_3O_4-graphene cells cannot sustain long term cycling, and typically failed after 250 cycles. This is also reflected by the initial charge/discharge curve of the Co_3O_4 cell, where over 110 $mA{\cdot}h{\cdot}g^{-1}$ irreversible capacity is exhibited during the charge process. Although vanadium oxides and cobalt oxide are both semiconductors, the much higher electronic conductivity of VO_2 may also play a role in the improved performance.[141] Since VO_2 undergoes a transition to a metallic state at 68 °C, this also allows for the possibility of reducing the transition to room temperature by elemental doping, making it even more attractive as a candidate for the sulfur host material.[142]

3.6 Conclusion

A holistic view on the ability of transition metal oxides to chemically adsorb polysulfides via the thionsulfate/polythionate mechanism was shown in this chapter. The underlying principle that drives this reaction, revealed by a combination of XPS and CV studies, indeed lies within the redox potential of lithium polysulfides. Materials with a redox potential that lies below the targeted window such as Co_3O_4 or NiO show no redox reaction with lithium polysulfides, although their strong beneficial surface polar and/or acid site interactions still exist that can mitigate polysulfide dissolution. A more effective mechanism is one exhibited by metal oxides that can engage in surface redox chemistry with polysulfides. Those with a redox potential in a target window ($2.4 < E^\circ \leq 3.05$ V) such as VO_2-graphene (2.79 V), which has a redox potential similar to that reported for

MnO_2 nanosheets (3.05 V), oxidize polysulfide to form thiosulfate/polythionate groups chemically bound to the reduced metal oxide surface. These are retained on cycling because they are ultimately reduced on full reduction to Li_2S, and then regenerated on charge, as previously reported.[41] Promising electrochemical results are established with cells using S-VO_2-graphene as a cathode host that show an initial discharge capacity of 1180 $mA{\cdot}h{\cdot}g^{-1}$ at C/20 and a decay rate of 0.058 % per cycle over 1000 cycles. Materials that lie too high in redox potential (>3.05 V) overoxidize polysulfides to a mixture of sulfate and thiosulfate. This is well exhibited by V_2O_5-graphene, which is able to repetitively oxidize polysulfides to electrochemically inactive sulfate groups, exhibited poorer cycling performance due to its higher redox potential (3.4 V). This new understanding allows us to realize a long-life Li-S battery by exploring new materials with suitable redox potentials to form surface bound thiosulfate/polythionate mediators and by optimizing their structure to facilitate better contact with lithium polysulfides.

Chapter 4

Exploration of Dual-Polysulfide Entrapment in MXene/CNT Composites

4.1 Introduction

To resolve the toxic polysulfide shuttling problem, researchers explored a wide range of promising approaches over the past years, including physical confinement by porous carbon frameworks,[23] chemisorption by polar materials,[39] and redox mediators that follow thiosulfate/polythionate conversion mechanism.[54] Although they all demonstrate remarkable Li_2S_n capabilities, taking the full advantage of the interactions requires an ultra-high surface area host material with more than one polysulfide entrapment pathways.

In this chapter, I demonstrate that MXene - a large family of 2D early transition metal carbides/carbonitrides - binds to polysulfide through a dual thionsulfate activation, followed by Lewis-acid-base mechanism. Originated from its parent layered MAX

phase ($M_{n+1}AX_n$, M = early transition metal, A = IIIA/IVA elements, and X = C or N), MXenes are produced by selectively etching the A atoms followed by delamination of the sheets in a polar solvent, as first reported by Naguib *et al.* [143] In fact, MXene nanosheets are best known for their high electrical conductivity and the abundant functional surface groups. The unique structure in MXene enables the material to promote polysulfide chemisportion on their *acidic* Ti sites, as elucidated by Liang *et al.* in 2015.[131]

However, recent reports on MXenes reveal that the material takes a general chemical formula: $M_{n+1}X_nT_x$ where T is the surface-terminated functional groups (OH, O, etc.) when delaminated.[144, 145] The work by Liang *et al.* - indicating polysulfides can be oxidized to thiosulfate by the hydroxyl groups on graphene oxide - led to a logical assumption that the thiosulfate/polythionate mechanism is also applicable to delaminated MXene nanosheets. Using Ti_2C, Ti_3C_2, and Ti_2CN as model systems, I study the surface reactivity of these titanium-based MXene phases upon contact with polysulfides species using XPS. This *dual* mode behaviour - thiosulfate/polythionate conversion and Lewis acid-base interaction - provides an unique mechanism to entrap polysulfides, and enables improved cycling performance in the resulting Li-S batteries. CNT is further incorporated into the MXene phase to improve the conductivity across the nanosheet planes and prevent restacking of the delaminated MXene nanosheets. It is further revealed that improving the electrical conductivity of the host material is important to endow good kinetics during deep cycling. The resultant Li-S cell thus not only exhibits an ultra-low decay rate of 0.043 % per cycle over 1200 cycles but also stable cycling performance with a practical high sulfur loading up to 5.5 $mg \cdot cm^{-2}$.

4.2 Experimental Methods

4.2.1 Preparation of MXene

The MAX parent phases (Ti_3AlC_2 and Ti_3AlCN) were prepared by solid state reaction at high temperature, as described elsewhere,[143, 146] where as Ti_2AlC was obtained from Sigma-Aldrich. All materials were sieved (325 mesh) prior to use. Exfoliation of the MAX phases were carried out by HF etching as previously reported.[131] To delaminate the MXenes, 300 mg of the etched MXene materials were stirred in 5 mL DMSO at room temperature for 18 h. The mixture was then centrifuged (10 kRPM, 10 min) and the DMSO supernatant was decanted to leave a residue, to which 100 mL water was added. After 4 h of sonication, centrifugation was carried out again (2 kRPM, 6 min) and the supernatant was collected. The delaminated MXene phases (d-MXene) were finally obtained by filtration.

4.2.2 Preparation of S-CNT-MXene Composites

In a typical procedure, d-MXene and CNT were stirred in 10 mL chlorosulfonic acid (99 %, Sigma-Aldrich) for 12 h. The suspension was then filtered on an anodic aluminum oxide membrane (Watman) and dried at 80 °C. Sulfur was subsequently melt-diffused (160 °C, 12 h) into the CNT-MXene composite at an appropriate weight ratio. The sulfur and carbon content in the composite was determined by TGA, and the results are summarized in **Table 4.1**.

Table 4.1. Composition percentage in the S-CNT-MXene composite.

Material	Fraction of Material [wt. %]		
	S	**CNT**	**MXene**
S-CNT-Ti_3C_2	79	10	11
S-CNT-Ti_3CN	83	10	17
S-CNT-Ti_2C	83	20	7

4.2.3 Electrode Preparation

Electrodes for Li-S batteries were fabricated by mixing the S-CNT-MXene composite with Super P carbon and PVDF binder in DMF in an 8:1:1 weight ratio, the slurry was then cast onto P50 carbon paper. The sulfur content on the *low*-sulfur loading electrode was 1.5 $mg{\cdot}cm^{-2}$. Higher sulfur loading of 3.6 and 5.5 $mg{\cdot}cm^{-2}$ were evaluated on the S-CNT-Ti_3C_2 composite. Typical Li-S electrolyte formulation was used, and all the electrochemical studies were conducted in a 2325 coin cells with a Celgard 3501 separator.

4.3 *Dual* Interactions between MXene and Polysulfides

MXene (Ti_3C_2 and Ti_3CN) were mixed with Li_2S_4 in DME, and the resulting solid was collected and subjected to XPS analysis to understand the surface chemistry between them. As shown in the top panel of **Figure 4.1A**, pristine Ti_3C_2 exhibits the characteristic Ti-O (459.3 eV) and Ti-C bonds (454.7 eV), similar to that of the Ti_2C MXene nanosheets reported previously.[131] Similarly, Ti-N (456.1 eV) and Ti-C (454.6 eV) bonds are identified in the pristine Ti_3CN materials (top panel, **Figure 4.1B**).[147] Upon

contact with Li_2S_4, there is an additional peak in the Ti 2p spectra that is indicative of a Ti-S bond at ∼455.6 eV for both materials (Li_2S_4-MXene; bottom panels, **Figures 4.1A** and **4.1B**). The Ti-S bond was originally ascribed to the strong Lewis acid-base interaction which involves unoccupied orbitals of the surface Ti atoms (Lewis acid) and the electronegative terminal sulfur atoms in polysulfide anions (Lewis base).[131]

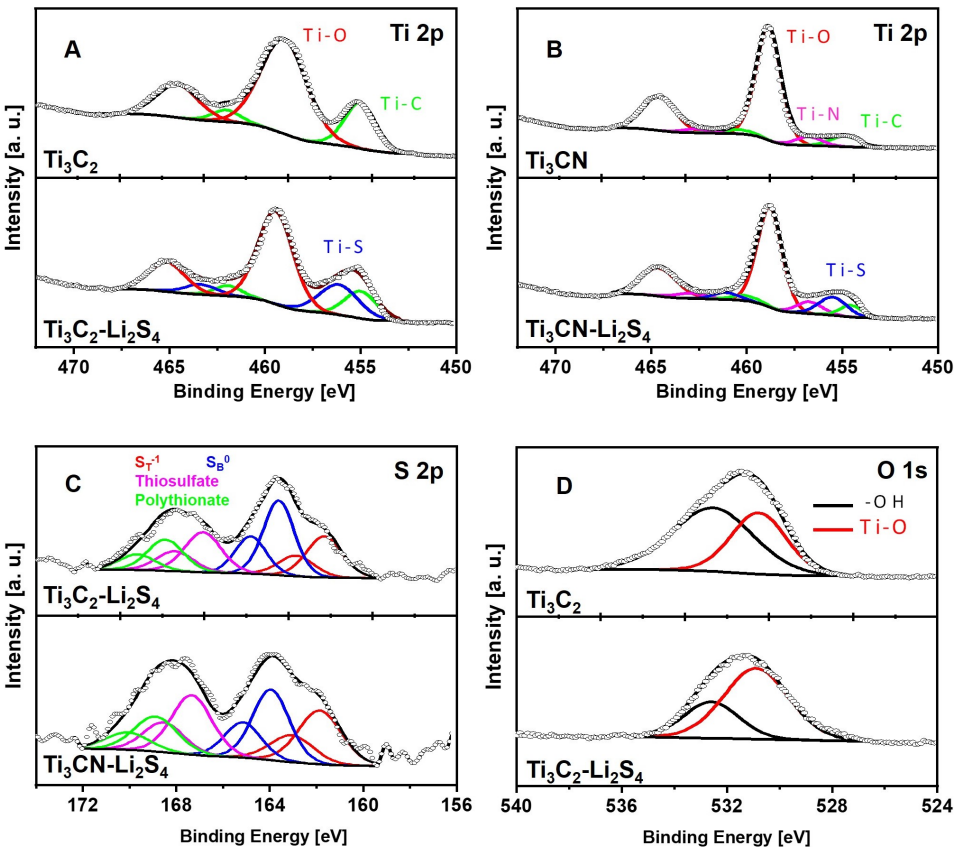

Figure 4.1. XPS study to elucidate the interaction mechanism between MXene and Li_2S_n. (A) Ti 2p spectra of Ti_3C_2 (top panel) and Ti_3C_2-Li_2S_4 (bottom panel); (B) Ti 2p spectra of Ti_3CN (top panel) and Ti_3CN-Li_2S_4 (bottom panel); (C) S 2p spectra of Ti_3C_2-Li_2S_4 (top panel) and Ti_3CN-Li_2S_4 (bottom panel); and (D) O 1s spectra of the Ti_3C_2 (top panel) and Ti_3C_2-Li_2S_4 (bottom panel).

However, the corresponding S 2p spectra shows features of thiosulfate (167.2 eV) and polythionate complexes (168.2 eV), alongside with the residual Li_2S_n as demonstrated by the terminal (S_T^{-1}, 161.9 eV) and bridging (S_B^0, 163.7 eV) sulfur environment (**Figure 4.1C**). It worth mentioning though that the peak corresponding to Ti-S overlaps with the S_T^{-1} due to their similar binding energies (162.3 ± 0.2 *vs.* 161.9 eV). The existence of the thiosulfate/polythionate in **Figure 4.1C** suggests MXene mediates polysulfide conversion process via sulfur catenation process. However, M-C and/or M-N bonds are amongst the strongest known and should not subject to reactions with polysulfides upon contact.[148] Indeed, there is no shift Ti-C and Ti-N bind energies as shown in bottom panels, **Figure 4.1A** and **4.1B**. Instead, the XPS O 1s spectra of the Li_2S_4-Ti_3C_2 suggests the terminal hydroxyl group on the surface of MXene serve as the reaction site for the thiosulfate conversion process. This is evidenced by the decreased Ti-OH fraction (532.2 eV) in comparison to that of the pristine (65 *vs.* 35 %, **Figure 4.1D**).[149] This mechanism is similar to that of the graphene oxide reported by Liang *et al.* in *Nat. Commun.*, where the conversion of the oxygen groups to thiosulfate surface-bound species is induced by polysulfides reducing the surface terminal hydroxyl group.[54]

In conclusion, interaction between MXene and polysulfides follows a two-step process as illustrated in **Figure 4.2**. The hydroxyl terminal groups on MXene first undergo redox reaction with polysulfides to form the surface thiosulfate groups,[54] exposing the underneath Ti atoms. These exposed and metastable Ti atoms then readily accept electrons from polysulfides in the electrolyte and form Ti-S bonds by Lewis acid-base interactions.

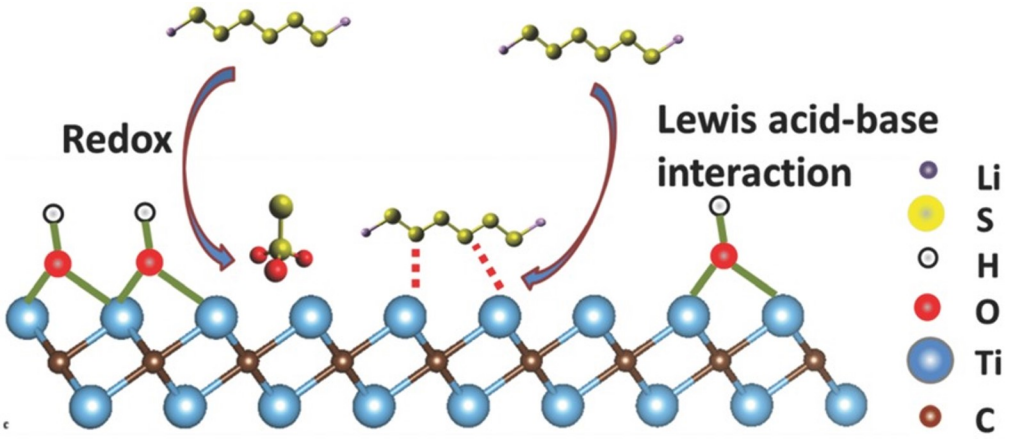

Figure 4.2. Schematic demonstration of the two-step interactions between a representative hydroxyl-decorated MXene phase and polysulfides.

4.4 Optimizing MXene Architecture using CNT Exfoliators

MXenes adopt a 2D nanosheets architecture, and were prepared by etching the Al layer via HF, followed by a delamination process using DMSO as originally proposed by Gogoski *et al.* [149] Successful removal of the Al layer to form MXenes is evidenced by the change in their XRD pattern as shown in **Figures 4.3A** and **4.3B**. Meanwhile, the crystal structures of the MXene materials remain intact after delamination. SEM analysis (**Figures 4.3C** to **4.3F**) reveal significant re-stacking of the nanosheets - despite delaminated MXene nanosheets are expected to have high surface area - due to the van der Waals forces attraction forces between them. This is confirmed by their low surface areas, measured by N_2 isotherm technique and summarized in **Figure 4.4A**. These values are not exceptional compared to some of the recently reported mosoporous materials.[20, 26] Since constructing high surface area host material is important to maximize the *dual* thiosulfate-polythionate/Lewis-acid-base chemisorption towards Li_2S_n, a

porous MXene architecture is thereby fabricated by sandwiching the nanosheets using CNT.

Multiwalled CNTs with an overage diameter of 8 nm were used in this study. Chlorosulfonic acid was chosen as the dispersing solvent for the CNT infiltration.[150] Utilizing Ti_2C as the representing MXene, the stability of the MXene material in super acid was confirmed by XRD analysis, which revealed no change in the nanosheet crystallinity after soaking the material in the acid medium for 12 h (**Figure 4.4B**). The Ti 2p (**Figure 4.4D**) and O 1s XPS spectra (**Figure 4.4E**) of the same materials further support there is no alternation in the surface chemical environment. This is particularly important to ensure that the surface dual-interaction mechanism is not compromised by the chorosulfonic acid. In general, for MXene with formula $M_{n+1}X_n$, a greater n leads to a higher M-C bond energy.[144] Thus, Ti_3CN and Ti_3C_2 would also be stable in the acid. Indeed, the XRD patterns comparison between CNT-MXene and their delaminated MXene counter part (**Figure 4.4F** and **4.4G**) confirmed that is the case. It worth noting though that the slightly weakened and broadened diffraction reflections in these diffractograms may imply better delamination of the nanosheets by the CNTs.

The SEM image in **Figure 4.4C** shows that the CNTs are very well dispersed in the MXene nanosheets. The surface area of the CNT-MXene composites are summarized in **Figure 4.4A**, illustrating significant surface area increase. In fact, the increase in surface area of the MXene-CNT composite exceeds the weighted sum of the pristine MXene and CNTs ($350\,m^2 \cdot g^{-1}$) phases for all three cases. In other words, carbon nanotubes serve as excellent exfoliators to prevent the delaminated MXene nanosheets from restacking, resulting in large internal porosity within the composite. Owing to the

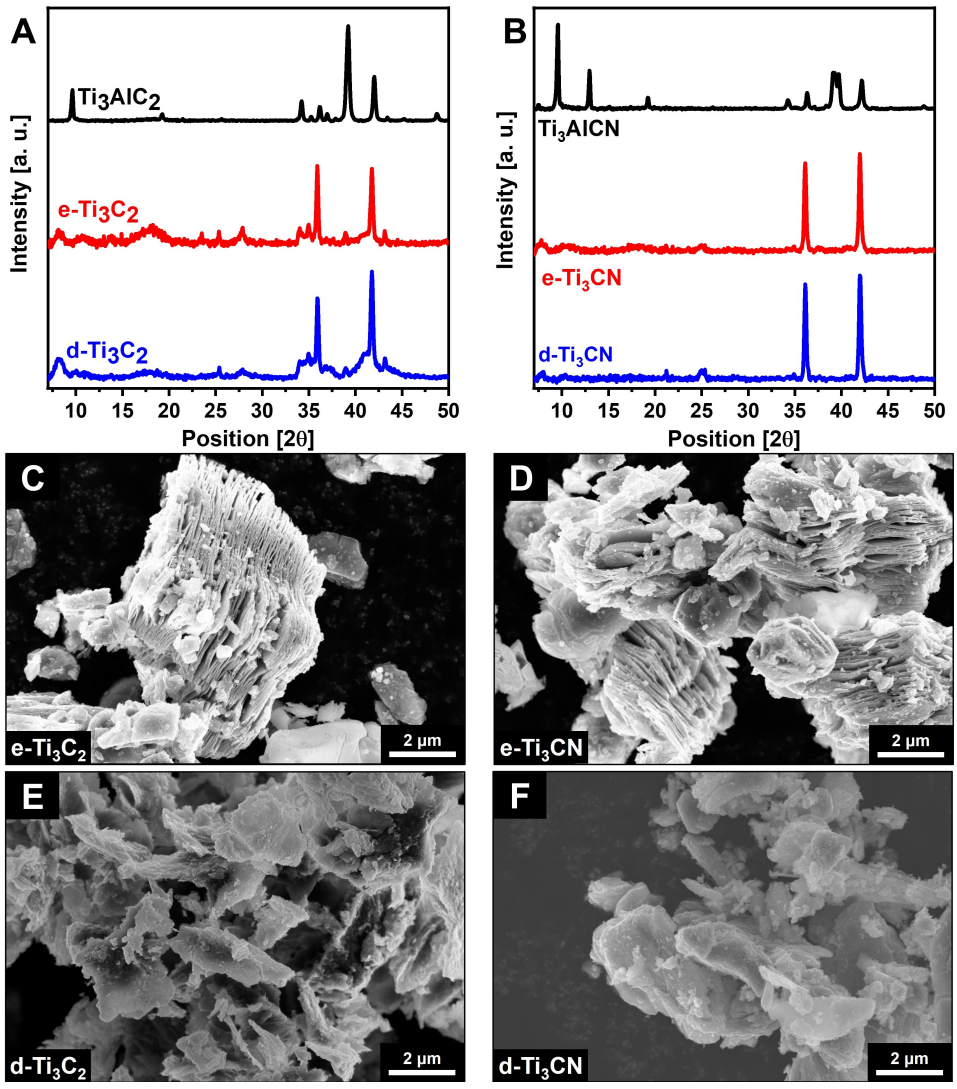

Figure 4.3. SEM and XRD analysis the parent MAX phase, etched-MXene, and delaminated-MXene. (A-B) XRD pattern of the MAX phases (black), etched MXene (e-MXene, red), delaminated MXene (d-MXene, blue) for (A) Ti_3C_2 and (B) Ti_3CN. SEM images of the MXene phases and the corresponding delaminated MXene (C) e-Ti_3C_2; (D) e-Ti_3CN; (E) d-Ti_3C_2; and (F) d-Ti_3CN.

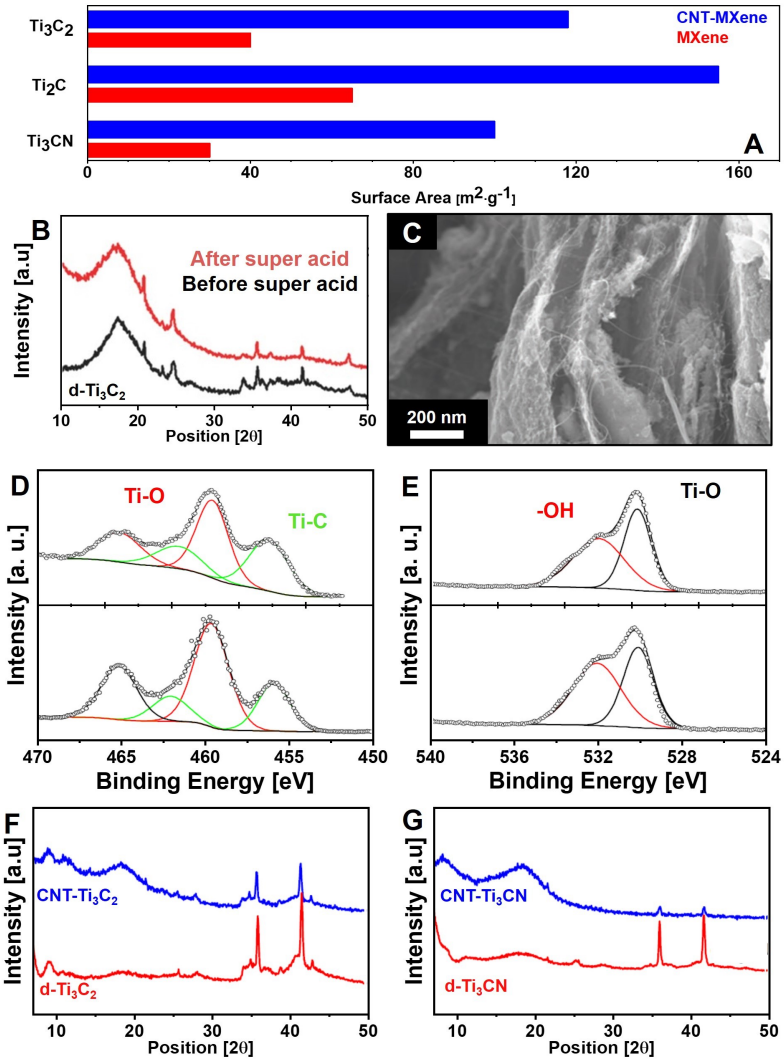

Figure 4.4. Comparison of the etched MXene nanosheets and CNT-MXene composites. (A) Surface area measured by the 5 point BET method. (B) XRD patterns of the Ti_2C nanosheets before and after immersion in chlorosulfonic acid; the broad feature at 18° is from the grease used to attach the sample. (C) SEM image of the CNT-Ti_3C_2 composite. (D) Ti 2p and (E) O 1s XPS spectra of the Ti_2C material before (top panel) and after (bottom panel) dispersed in the super acid. (F-G) Comparison of the XRD patterns of the MXene and CNT-MXene, showing no crystalline structure damage by the acid.

enhanced surface area and porosity, high sulfur content in S-CNT-MXene was achieved by melt diffusion without any significant sulfur aggregation as shown in **Figure 4.5A - 4.5C**. The thermogram in **Figure 4.5D** further confirms the sulfur loading in the CNT-MXene composite to be around 79 - 83 wt. %. The additional weight loss at around 580 °C is the oxidation of the CNT exfoliators. The exact value for each components is summarized in **Table 4.1**

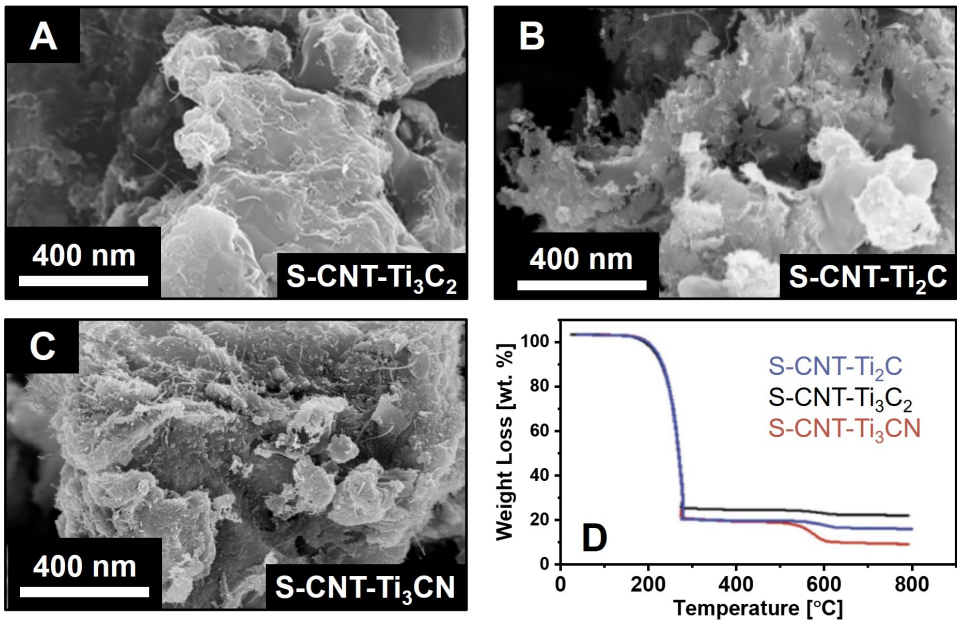

Figure 4.5. SEM and TGA analysis of the S-CNT-MXene cathode composite. SEM images of (A) S-CNT-Ti_3C_2, (B) S-CNT-Ti_2C, and (C) S-CNT-Ti_3CN composite material. (D) TGA analysis of these composites detailing the sulfur content.

4.5 Electrochemistry of CNT-MXene Sulfur Electrode

Li-S cells were assembled to evaluate the effects of the dual polysulfide entrapment mechanism and the improved electrical conductivity by CNT in these materials. A low sulfur loading (1.5 $mg{\cdot}cm^{-2}$) and a relatively high E/S ratio of 13:1 ($\mu L{\cdot}mg^{-1}$) was first employed to enable a fair comparison with the previously published work by Liang *et al.*[131] An initial discharge capacity of 1240, 1216, and 1263 $mA{\cdot}h{\cdot}g^{-1}$ are obtained at C/20 for the S-CNT-Ti_2C, S-CNT-Ti_3C_2, and S-CNT-Ti_3CN electrodes, respectively (**Figure 4.7A**). These sulfur electrodes display a similar capacity retention in their long-term cycling at C/2 rate: retaining $\sim$450 $mA{\cdot}h{\cdot}g^{-1}$ after 1200 cycles, corresponding to a decay rate of 0.043% per cycle (based on the first discharge capacity at C/2). The excellent cycling observed can be ascribed to the improved electronic conductivity and porous structure on the overall cathode composite due to the incorporation of CNTs Compared to the previous study on S-Ti_2C without any CNT,[131] improved electrochemical performance is observed, while both the sulfur content in the composite (83 vs 70 wt. %) and active material areal loading in the electrodes (1.5 *vs.* 1.0 $mg{\cdot}cm^{-2}$) of the S-CNT-MXenes were increased, owing to their more conductive and porous structure. In fact, EIS measurement of the representing Li-S cells fabricated with S-CNT-Ti_3C_2 sulfur electrode showcases stable and low resistance compared to that of the CNT-free sulfur electrode. (**Figure 4.6**).

Achieve high sulfur loading cell is critical in unlocking the high energy density proposed by Li-S cells. The electrochemical performance of the sulfur cathode fabricated with CNT-Ti_3C_2 at various sulfur areal loading were examined to demonstrate the ad-

vantages of the nanostructured host material (**Figure 4.7B** and **4.7C**). Here, a low E/S ratio of 7:1 was employed to minimize the weight contribution from the electrolyte and thereby maximize energy density at the cell level. All cells were conditioned at C/20 for the first cycle. Although there is a sulfur utilization penalty associated with increasing sulfur loading, the areal capacity in high sulfur loading cells remains competitive (**Figure 4.7B**). For instance, the cell at a loading of 1.5 $mg{\cdot}cm^{-2}$ exhibits a much higher initial discharge capacity than the cell with a 5.5 $mg{\cdot}cm^{-2}$ (1216 *vs.* 910 $mA{\cdot}h{\cdot}g^{-1}$). However, the areal capacity of the latter cell is at least three times higher than the lower loading cell (1.8 *vs.* 5.5 $mA{\cdot}h{\cdot}cm^{-2}$). Furthermore, no obvious polarization increase upon higher sulfur loading is observed based on the discharge/charge curves (**Figure 4.7B**). Deep cycling of the thick electrodes (3.6 and 5.5 $mg{\cdot}cm^{-2}$) at a C/5 rate shows capacity fading for the first 50 cycles followed by very stable capacity retention over 250 cycles (**Figure 4.7C**). The excellent performance of the high loading electrodes emphasizes the collective importance of high conductivity, high surface area, and the effective polysulfide chemical adsorptivity in sulfur hosts.

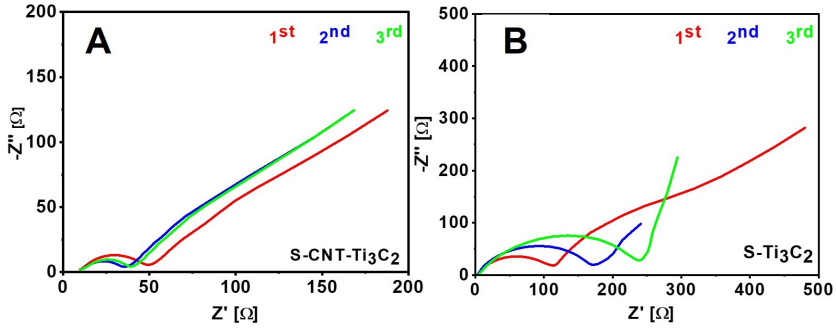

Figure 4.6. EIS measurement of the sulfur cathodes fabricated with MXene and CNT-MXene composite after discharge. (A) CNT-Ti_3C_2 and (B) Ti_2C after discharge.

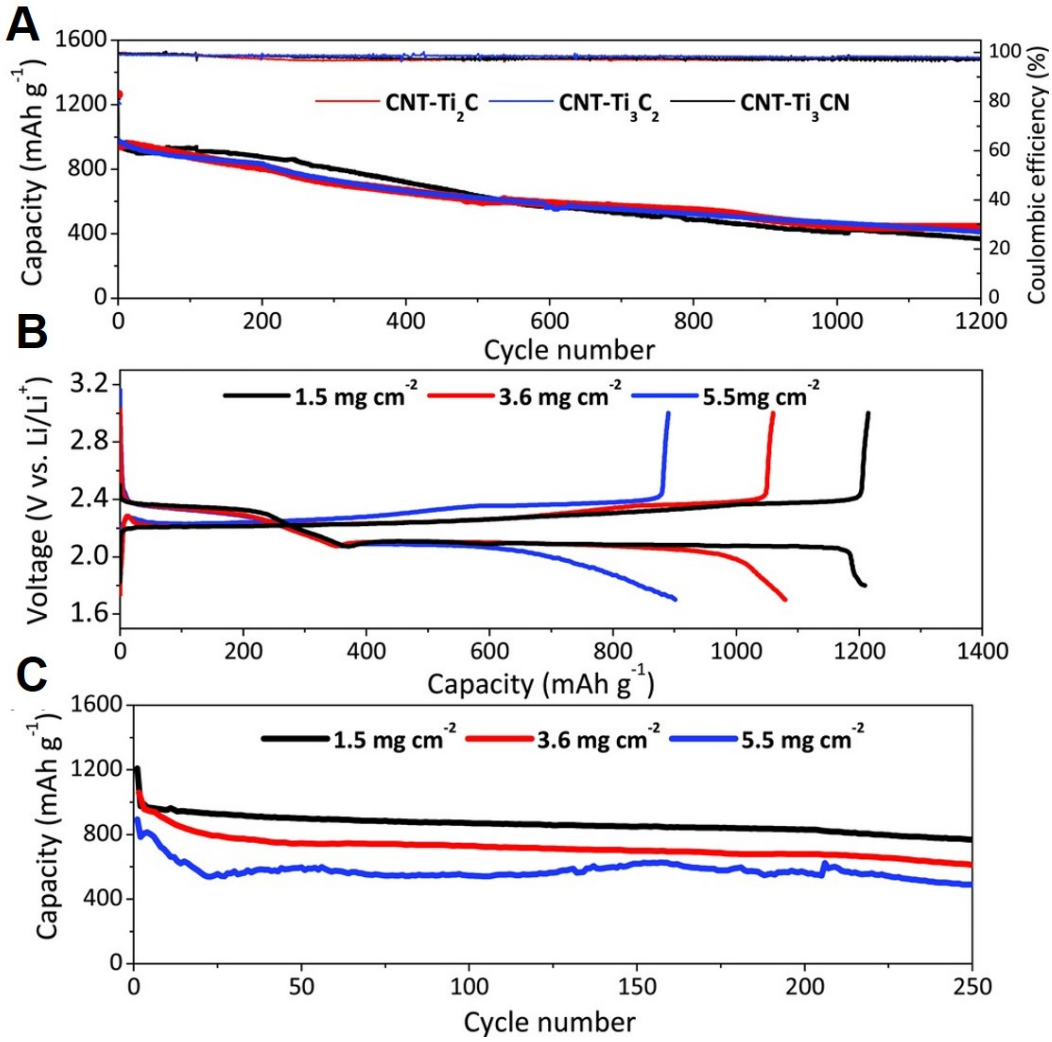

Figure 4.7. Electrochemical performance of the Li-S cells fabricated with the CNT-MXene composite as sulfur host. (A) Long-term cycling of CNT-Ti_2C (red), CNT-Ti_3C_2 (blue), and CNT-Ti_3CN (black) sulfur cathodes at an areal sulfur loading of 1.5 mg·cm^{-2} and C-rate of C/2. (B) First cycling profile of the CNT-Ti_3C_2 host material at a variety of sulfur loading. (C) Long term cycling performance of these cells at C/5 rate.

4.6 Conclusion

The dual interfacial interaction between the metallic MXene and polysulfides is presented. This interaction is achieved by the cleavage of the Ti-OH bond via the formation of thiosulfate, and thereby exposes the underlying Ti atoms to enable a strong Lewis acid-base interactions with polysulfides. The formation of thiosulfate/polythionate groups on the MXene nanosheets shows that the surface hydroxyl moities are subject to redox activity with polysulfides, similar to previously studied metal oxides and graphene oxide.[54] Interweaving CNTs between the MXene layers further creates a high surface area, porous, electronically conductive framework to enable high polysulfide adsorption, evidenced by the excellent long-term cycling performance and fading rates as low as 0.043 % per cycle for up to 1200 cycles in the resultant Li-S cells. This new finding provides a deeper understanding of the surface interactions between host materials and polysulfides to stable cycling performance at practical high loading electrodes.

Chapter 5

Understanding the Mechanical Properties of Functionalized Cross-Linked Binders on Li-S Batteries

5.1 Introduction

With the advancement in sulfur host materials to capture lithium polysulfides, fabricating a high areal capacity and stable-cycling Li-S battery still remains a major challenge. Low-sulfur loading ($< 2\,\mathrm{mg{\cdot}cm^{-2}}$) Li-S cells are often reported, whereas achieving high-sulfur loading cells with a practical electrolyte/sulfur ratio is critical to maximize cell energy density. While constructing 3D carbon network enables very high-sulfur-loading cathode achievable, the large voids in these structures requires excessive use of electrolyte (e.g. $>$ 20 µL of electrolyte per mg of sulfur in the cathode) to fully wet the electrode, and thus compromising the overall energy density. Casting active materials

on the current collector by a traditional slurry process is a more viable avenue, as it maximizes the packing efficiency and is commensurate with current industrial protocols. However, this process requires the use of functional binders to provide an elastic interface for the essential cathode components to prevent them from delaminating from the cathode over extensive cycling.

Binders are polymers that hold the critical components in the electrode together during battery operation. Their primary functions in Li-S batteries are to (a) bridge individual particles together with the current collector; (b) assist the carbon additive to maintain electronic contact upon cycling; (c) facilitate Li^+ transport at the electrode-electrolyte interface; and (d) provide chemical interactions against polysulfide dissolution. As discussed briefly in **Section 1.3.2**, PVDF is conventionally used due to its excellent thermomechanical properties and adhesion to the cathode materials in lithium ion batteries. However, as Li-S chemistry is haunted by polysulfide dissolution, it is highly desirable to instead arm the binder with active functional groups to anchor these intermediates. Thankfully, the same functional groups that provide material adhesivity also demonstrate polysulfide adsorptivity. This was demonstrated in early studies, which showed that such modified binders exhibit improved cyclability in comparison with PVDF.[151, 152, 153] The performance enhancement was attributed to amine, hydroxyl, carboxyl, and carboxylic groups as moieties. Nonetheless, the binding energy of these functional groups is still too weak to suppress polysulfide shuttling,[38] and the sulfur loading in these reports was far too low for any practical applications. Only recently have a few studies focused on designing new binder systems for thick electrodes, exemplified by polyamidoamine dendrimers,[57] CMC/SBR,[59], and cross-linked elastomeric

carboxymethyl cellulose.[60] Cationic polyelectrolyte binders are gaining popularity in recent years for their effectiveness at restricting polysulfide diffusion, benefited from the strong electrostatic interactions.[154] In parallel, researchers are starting to recognize the importance of the mechanical properties of binders to maintain the structural integrity of multicomponent sulfur cathodes, although there is still a lack of understanding on the impact of the binder's characteristics in addressing the continuous volume expansion/contraction experienced during Li-S cell cycling, and its interactions with other cell components such as electrolyte. For example, an early work by Park *et al.* noted preserving the strong interactions between the polymer and lithium polysulfides is strongly correlated with the electrolyte (i.e. DOL/DME) uptake by polymeric materials.[155]

In this chapter, I described a new class of ammonium chloride-based cross-linked binder that not only strongly interacts with lithium polysulfides contribute to greatly suppressed polysulfide shuttling but also has optimal interfacial and mechanical properties to allow stable cycling of high-sulfur loading cathodes. The strong charge-transfer interactions between the ammonium cation and polysulfide anion, as well as the consequent molecular reorganization of these species are demonstrated by spectroscopic and electrochemical studies. More importantly, I correlated the electrochemical performance of sulfur cathodes with the mechanical properties of three different polymeric binders, including one similar in chemical functionality but with inferior mechanical properties. The study showed that cross-linked polymers with a low swelling ratio and a high tensile strength, Young's modulus, and toughness are critical for delamination tolerance. Furthermore, excellent compatibility of the polymer binder with the selected casting solvent allows the utilization of a conventional slurry process to construct mechanically

stable electrodes.[59, 60] Using this approach, a high-sulfur loading (6.0 mg·cm^{-2}) Li-S cell utilizing a low electrolyte/sulfur ratio of 7:1 (µL:mg) can operate for 300 cycles with a low capacity fade rate.

5.2 Experimental Methods

5.2.1 Preparation of Poly(AETMAC-*co*-EGDA) Cross-Linked Polymer

Free-radical polymerization was employed to cross-link [2-(acryloyloxy)ethyl] - trimethylammonium chloride (AETMAC) and ethylene glycol diacrylate (EGDA) at 80 °C in dry ethanol. The molar ratio between the monomer and the cross-linker was maintained at 4:1. AETMAC (80 wt . % in H_2O, Sigma-Aldrich) containing 600 ppm monomethyl ether hydroquinone inhibitor was first passed through aninhibitor-remover column (Sigma-Aldrich) twice prior to use. Next, 804 mg of the purified AETMAC aqueous solution, 157 mg of EGDA (90 % technical, Sigma-Aldrich), 39 mg of Azobisisobutyronitrile (AIBN, 99 %, recrystallized, Sigma-Aldrich) and 4 g of dry ethanol (Fisher Scientific) were introduced into a 50 mL round-bottom flask. The flask was sealed with a rubber septum, and the mixture was stirred rapidly for 15 min. After a clear solution was obtained, the mixture was purged gently with dry nitrogen for additional 10 min before placing the flask in an oil bath (80 °C) on a stir plate. The stirred reaction was terminated after 12 h, and the cross-linked polymer was recovered by precipitation in acetone (ACS, Sigma-Aldrich). Finally, the cross-linked polymer was filtered and rinsed

with cold isopropanol (anhydrous, Sigma-Aldrich) to remove any unreacted precursors.

5.2.2 Preparation of Poly(DADMAC-*co*-EGDA) Cross-Linked Polymer

The free-radical cross-linking polymerization between diallyldimethylammonium chloride (DADMAC) and EGDA was achieved in a similar manner to the experimental procedure described above. However, the copolymerization temperature for poly(DADMAC-*co*-EGDA) was set to 60 °C, and the molar ratio of monomer to cross-linker was 2:1. In a typical procedure, a mixture of 604 mg of DADMAC (97 % AT, Sigma- Aldrich), 353 mg mg of EGDA, 44 mg of AIBN, and 4 g of anhydrous ethanol in a 50 mL round-bottom flask was used for the reaction. The flask was sealed with a rubber septum, and the mixture was stirred for at least 15 min to allow dissolution of the reactants; the solution was then purged gently with dry nitrogen for 10 min. The flask was placed in an oil bath (60 °C), and the mixture was stirred for 12 h, although the contents turned cloudy 10 min after the start of polymerization. Finally, the cross-linked polymer was filtered and rinsed with cold isopropanol to remove any unreacted precursors.

5.2.3 Preparation of the Porous Hollow Carbon Sphere Sulfur Host

The host material was synthesized as previously reported.[19] Typically, 23 mL ammonia aqueous solution (28 wt. %, Sigma-Aldrich) was added to a mixture of 80 mL deion-

ized water and 620 mL anhydrous ethanol. After the mixture was stirred for 30 min at 30 °C, 21 g tetraethyl orthosilicate (Sigma-Aldrich) was added to the solution drop wise. A separate solution containing 3.29 g resorcinol (ACS, Sigma-Aldrich) and 480 µL poly(DADMAC) aqueous solution (7 wt. %) dissolved in 4.85 g formaldehyde (37 wt. % in H_2O, Sigma-Aldrich) was added to the silica solution. The entire mixture was stirred at 30 °C for 24 h and maintained at 100 °C for another 24 h in a Teflon-lined autoclave under static condition. The brown solid was then collected by centrifugation (10 kRPM, 5 min) and dried at 90 °C for 12 h. Carbonization of the material was conducted at 750 °C, at a heating rate of 3.75 °C·min^{-1} under Ar flow for 1 h. The silica core was etched away by treating the material in 0.1 M HF for 12 h. The solids were then filtered, rinsed with excessive water, and dried at 90 °C for 12 h before use. Finally, elemental sulfur was melt-diffused into the porous hollow carbon spheres (PHCSs) at 160 °C for 12 h to afford the S-PHCS composite. The sulfur content was determined by TGA to be 75 wt. %.

5.2.4 Preparation of the Li_2S_4-Homopolymer Mixture.

All of the solid materials were vacuum-dried in a Büchi vacuum oven at 60 °C for 24 h prior to use. In an Ar-filled glovebox, 20 mg of homopolymer and 20 mg of Li_2S_4 were stirred in 2 mL of DME for 6 h. The material for FTIR analysis was collected by centrifugation (10kRPM, 10 min) followed by vacuum drying at room temperature for 12 h.

5.2.5 Mechanical Test

The P50 carbon paper samples with the cathode composite material (S-PHCS + Super P + CNT + binder) coated in the same manner as for electrode preparation were cut into 3" × 1" rectangular shapes and mounted via grip heads. Mechanical tests were carried out on an universal macrotribometer (UNMT-2MT, Centre for Tribology, Inc.) with a 10 kg load cell. The force and displacement were controlled by a step-motor at a pull rate of 0.01 $mm \cdot s^{-1}$

5.2.6 Electrode Preparation

The electrodes were prepared from a water/dimethylformamide (6:4) slurry containing 80 wt. % S-PHCS, 5 wt. % Super P, 5 wt. % 8 nm multiwall carbon nanotubes, and 10 wt. % polymeric binder onto P50 carbon paper. Only dimethylformamide was used when PVDF is served as a binder. The sulfur loading on these electrodes was either 3.5 or 6.0 $mg \cdot cm^{-2}$. The electrodes were dried in a 60 °C oven for 24 h before they were transferred to an Ar filled glovebox. Li-S coin cells (2325) were assembled using lithium foil as anode/reference electrode. Typical Li-S electrolyte formulation was used, and the electrolyte/sulfur ratio was maintained at 7:1 in all electrocemical studies. CV and EIS studies where conducted at a scan rate of 0.1 $mV \cdot s^{-1}$ and amplitude of 10 mV in the frequency range of 200 mHz to 500 kHz, respectively.

5.3 Physical Characterization of the Cross-linked Polymers

Two highly cross-linked polymers based on ammonium chloride functional groups were prepared via radical polymerization. EGDA was used as the cross-linking agent to copolymerize with either AETMAC or DADMAC monomers (**Figures 5.1A** and **5.1B**) to fabricate the 3D polymeric network; these are referred to as poly(AETMAC-*co*-EGDA) and poly(DADMAC-*co*-EGDA), respectively. The two cross-linked polymers have similar functional groups in their subunits that regulate lithium polysulfide transport in the electrolyte. However, they exhibit very different mechanical properties due to differences in the reactivity of the monomers with EGDA, which controls the density of the cross-linked network. The density was optimized with respect to their electrochemical performance as binders in Li-S cells. Successful cross-linking copolymerization was confirmed by the insolubility of the products in water, unlike the monomers which are highly soluble. Moreover, the FTIR spectra of the poly(AETMAC-*co*-EGDA) (top-panel, **Figure 5.1C**) shows absence of alkene (C=C or =CH) bands signatures. This suggests a complete conversion of the precursor monomer, where the residual monomers were washed away in the purification steps. Instead, the spectrum exhibits ester (1736 cm^{-1}) and C-N (1655 and 3435 cm^{-1}) moitiés. Furthermore, compared with the FTIR spectrum of the physical mixture of poly(AETMAC)-poly(EGDA) homopolymer material (bottom-panel, **Figure 5.1C**), the band attributed to the C-N stretching vibration in the secondary amine group and the C=O stretching band in the ester group are shifted from 3429 to 3435 cm^{-1} and 1732 to 1736 cm^{-1}, respectively, indicative of strong bonding interactions within the functional groups due to

copolymerization linkage.[156] Similarly, the successful cross-linking of DADMAC by EGDA to form poly(DADMAC-*co*-EGDA) was also confirmed by FTIR (top-panel, **Figure 5.1D**). Peaks attributed to poly(DADMAC-*co*-EGDA): are ester C=O (1734 cm^{-1}) and C-N (1639 and 3439 cm^{-1}) groups. The characteristic peaks ascribed to the C-N and C=O groups in poly(DADMAC-*co*-EGDA) are also significantly shifted compared to their homopolymer mixture (bottom-panel, **Figure 5.1D**).[157]

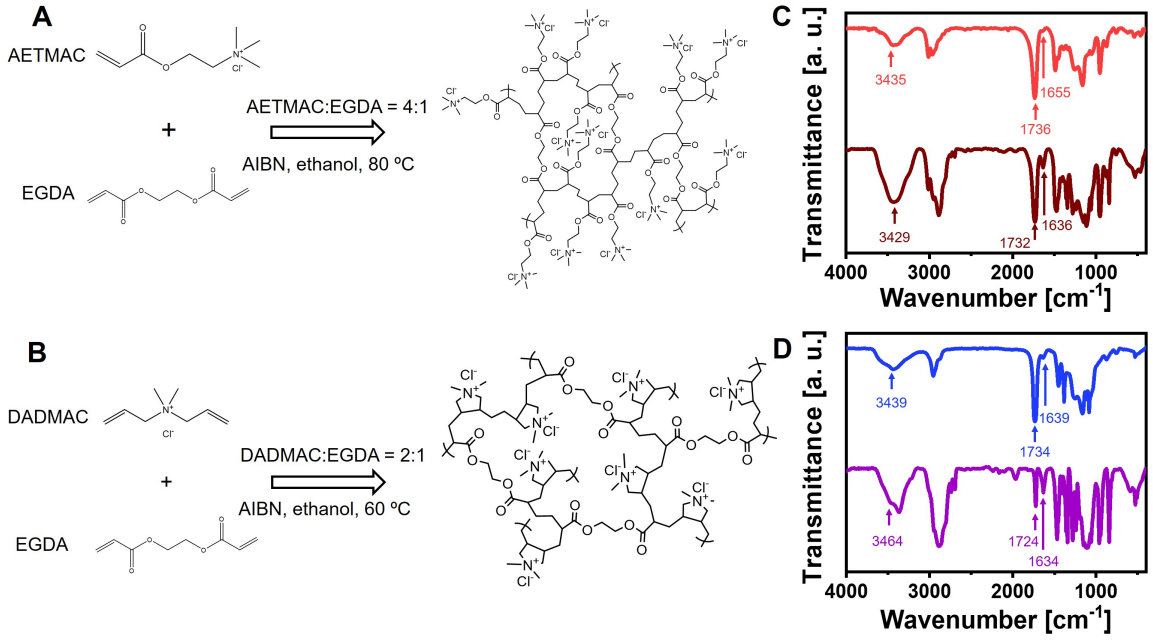

Figure 5.1. Synthesis of cross-linked polymers via radical polymerization. Schematic representation of the cross-linker (EGDA) reacting with (A) AETMAC and (B) DADMAC to form a three-dimensional polymeric network. FTIR transmission spectra for (C) poly(AETMAC-*co*-EGDA) and (D) poly(DADMAC-*co*-EGDA), respectively, to confirm cross-linking: the cross-linked polymer (top-panel) and physical mixture of their homopolymer counterparts (bottom-panel).

5.4 Chemical Interactions between Polymers and Polysulfides

The interactions between the functional groups in the polymer binders and lithium polysulfides (as represented by Li_2S_4) were examined by FTIR spectroscopy to elucidate the mechanism of the charge-transfer binding effect. The N-C moieties (3400 and 1640 cm^{-1}) and the ester C=O moieties (1700 cm^{-1}) are potential indicators of this process. Homopolymers were mixed with Li_2S_4 dissolved in DME, and the solids were extracted for the FTIR analysis. The FTIR spectra obtained for the pristine homopolymer and Li_2S_4, as well as the homopolymer-Li_2S_4 mixtures with poly(AETMAC), poly(DADMAC), poly(EGDA), and PVDF are compared in **Figure 5.2**. Homopolymers were used in this analysis to ensure that the interactions observed in the FTIR spectra are only attributed to specific functional groups. The pristine poly(AETMAC) in **Figure 5.2A** exhibits a sharp peak at 1638 cm^{-1} and a broad band at 3425 cm^{-1}, corresponding to the unsaturated primary amine and C-N stretching vibrations in the secondary amine group.[156] Upon contact with Li_2S_4, these peaks shifted to much lower wavenumbers of 1622 and 3400 cm^{-1}, and their intensity significantly decreased. Similarly, for poly(DADMAC), these bands also shifted by about 10 cm^{-1} (from 1636 to 1628 cm^{-1} and from 3447 to 3412 cm^{-1}) when blended with Li_2S_4 (**Figure 5.2B**).[157] In addition, the rearrangement of the sulfur chain in the polysulfide is observed, signified by a shift in the symmetrical S-S band from 484 to 453 and 449 cm^{-1} in the poly(AETMAC)-Li_2S_4 and poly(DADMAC)-Li_2S_4 materials, respectively.[40, 158] All these molecular rearrangements, delineated by the shifts in their respective FTIR spectra, indicate that charge transfer takes place between the ammonium cations and the

polysulfide anions.[159] The acidic character of the ammonium cations enables their direct electrostatic binding to the polysulfide anions.[160] This interaction causes the original C-N and S-S bond lengths to increase as a result of bond weakening. Thus, a red-shift in their FTIR spectra (middle panel, **Figures 5.2A** and **5.2B**) is observed.[32] However, no shifts in vibrational modes associated with carbonyl groups is observed, likely because the carbonyl groups instead bind to lithium ions via the oxygen empty 2p orbital. Such indirect interactions do not disturb the S-S and C=O bonds,[38, 155] as seen in the invariant sharp peak ascribed to the ester C=O bond in poly(AETMAC) (1736 cm^{-1}, **Figure 5.2A**) or poly(EGDA) (1726 cm^{-1}, **Figure 5.2C**). Of course, the fluoride group in PVDF (**Figure 5.2D**) cannot engage in any interactions with lithium polysulfide. Accordingly, the PVDF-Li_2S_4 materials show only features characteristic for polysulfide and a C-F asymmetric stretching band (1402 cm^{-1}).[161]

In light of the interactions described above, I further examined the polysulfide adsorptivity of these binders via a facile titration technique: electro-oxidization of polysulfides.[126] Although lithium polysulfides are known to disproportionate in glyme, Li_2S_4 and Li_2S_6 are the most prevalent soluble species during sulfur redox and were hence selected as representative probe molecules.[154, 162] Each binder material was accurately weighed into a stock solution of Li_2S_4 or Li_2S_6 in DME. The supernatant was then collected and subjected to electrochemical titration of the remaining Li_2S_n in the solution. Prior knowledge of the concentration in the stock solution of Li_2S_4 and Li_2S_6 enables the determination of the amount of Li_2S_n removed from the supernatant via adsorption onto the binder materials.

The Li_2S_4 and Li_2S_6 adsorptivity measurement results for PVDF, poly(DADMAC-

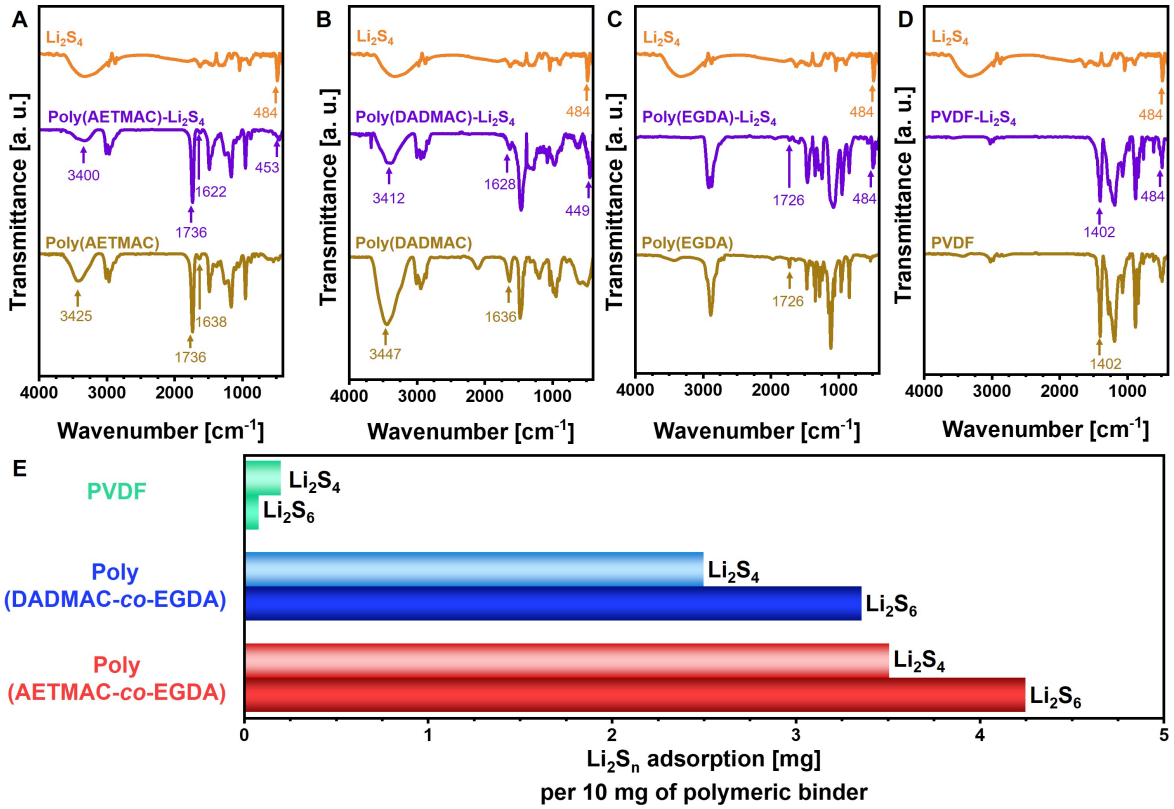

Figure 5.2. Chemical interactions between functional groups present in the binders and lithium polysulfide. FTIR spectra to probe the interactions between the functional group in each homopolymer and Li_2S_4 for (A) poly(AETMAC); (B) poly(DADMAC); (C) poly(EGDA); (D) PVDF. (E) Summary of calculated polysulfide adsorptivity per 10 mg of PVDF (green), poly(DADMAC-*co*-EGDA) (blue), and poly(AETMAC-*co*-EGDA) (red). The lighter colour bar represents Li_2S_4 and the darker colour represents Li_2S_6.

co-EGDA), and poly(AETMAC-*co*-EGDA) are summarized in **Figure 5.2E**. Unsurprisingly, PVDF adsorbs much less polysulfides compared with the two cross-linked polymers. These results are in strong agreement with the FTIR analysis, showing there are no chemical interactions between the fluoride moieties and lithium polysulfides.[163] On the other hand, the ammonium subunits in both poly(AETMAC-*co*-EGDA) and

poly(DADMAC-*co*-EGDA) network engage in acid-base interactions with the polysulfide anions. It is speculated that the polysulfide adsorptivity of these polyelectrolytes could be further enhanced via ion exchange of Cl^- for an even more weakly associated counter anion to reduce interactions with the cationic subunit in the network.[164, 165] Nonetheless, both of these cross-linked polymer binders exhibit comparable polysulfide adsorptivity to some cathode host materials that have demonstrated a superior ability to readily bind polysulfides.[9] Further correlation can be drawn between Li_2S_n adsorptivity on the cross-linked polymers and the chain-length of the polysulfides. Both poly(AETMAC-*co*-EGDA) and poly(DADMAC-*co*-EGDA) have higher affinity toward the higher order hexasulfide than the tetrasulfide. Poly(AETMAC-*co*-EGDA) features the highest adsorptivity (4.25 mg Li_2S_6 per 10 mg of polymer). Recent work by Li *et al.* also showed that lithium ions are less tightly bound to the terminal sulfur anions in high-order polysulfides.[154] My experimental results complement well with their computation.

5.5 Electrochemistry of Thin Electrodes

The effects of these binders in the Li-S cells were examined using PHCSs as sulfur hosts. SEM (**Figure 5.3A**) and TEM (**Figure 5.3B**) analysis confirm that the nanoparticles were homogenous with average size of ~200 nm. The specific surface area of the PHCSs, measured by nitrogen adsorption analysis, is 593 $m^2 \cdot g^{-1}$ with a pore volume of 1709 $cm^3 \cdot g^{-1}$ (**Figures 5.3C** and **5.3D**).[19] These high surface area carbon spheres enable a large fraction of sulfur to be loaded in the cathode, while maintaining good

electronic conductivity. Sulfur was loaded into these spheres via melt-diffusion at 160 °C. SEM image (**Figure 5.4A**) shows that sulfur is uniformly distributed to afford the composite material S-PHCSs, and no bulk sulfur deposits are visible. TGA in **Figure 5.4B** further confirms the sulfur loading to be 75 wt. %, and shows two regions of sulfur loss. The 70 wt. % sulfur loss below 280 °C is attributed to sulfur in the mesoporous shell and near the inner surface. At 300 °C, an additional 5 wt. % loss is attributed to sulfur confined deep in the interior structure of the carbon spheres.[19] The weight loss at around 625 °C is due to oxidation of the carbon framework that makes up PHCSs.

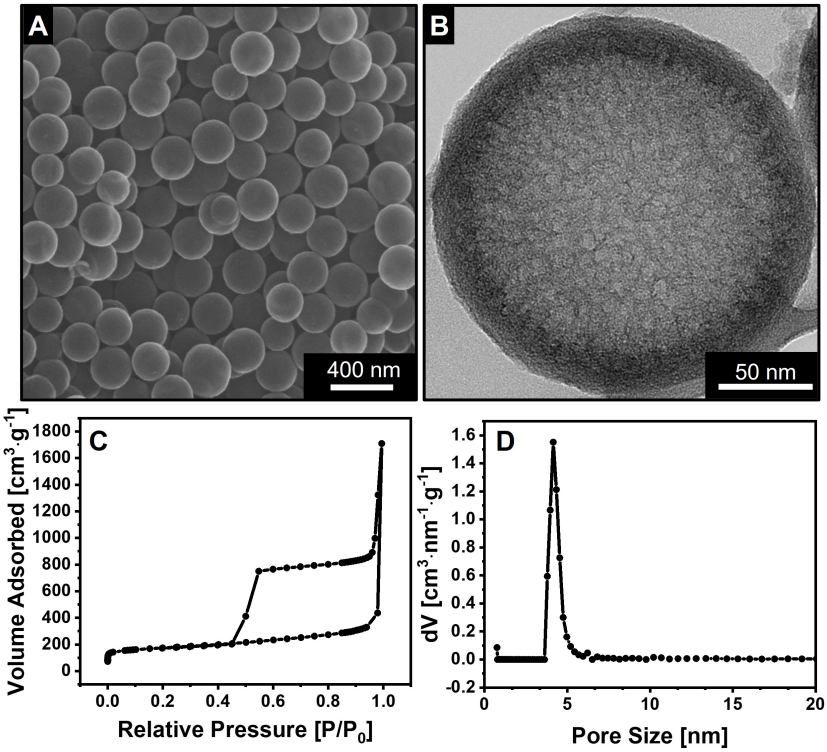

Figure 5.3. Physical characterization of PHCS. (A) SEM and (B) TEM images of the host material. (C) N_2 adsorption isotherm and (D) pore size distribution curve for the same material.

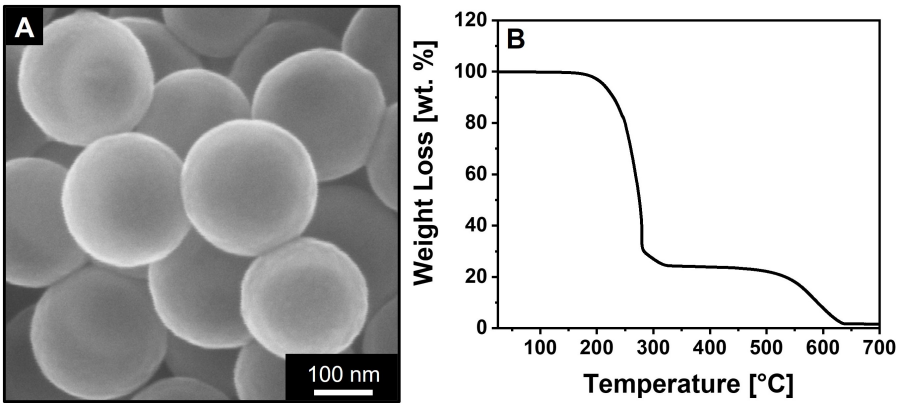

Figure 5.4. SEM and TGA analysis for S-PHCS. (A) SEM image and (B) TGA curve, yielding a sulfur content of 75 wt. % at a ramp rate of 10 °C·min^{-1} under air flow.

Constructing a compact cathode via the traditional slurry process demands the binders to be evenly distributed on the current collector. The conductive carbons (Super P and carbon nanotubes) and active composite material (S-PHCS) in the casting solvent need to be at a certain concentration to achieve a viscosity to ensure effective mixing, dispersion, and penetration of the binder material into the electrode.[59, 166] The hydrophilic character of these cross-linked polyelectrolyte binders provides excellent compatibility with water. A binary solvent system comprised of water and dimethylformamide was used for the two cross-linked polymers, whereas only dimethylformamide was used to prepare the PVDF casting solution. Dimethylformamide homogenizes the nonpolar S-PHCSs and carbon, whereas water ensures that the binder is well dispersed in the solvent. The S-PHCS composite, carbon additives, and the binder solutions were mixed and cast on both sides of P50 carbon paper via a layer-by-layer deposition technique to maximize the packing efficiency. The use of P50 as a current collector is dictated by several factors. In comparison with an Al foil current collector, the micron-sized car-

bon fibers (**Figure 5.5A**) provide a 3D electronically conductive network that enables excellent electron transfer to the adherent cathode materials, while precluding any aluminum corrosion that could result from the reaction between the chloride counter-ions with an Al current collector.[164] The fibrous structure of the P50 carbon paper further allows sufficient electrolyte penetration, without compromising the overall sulfur content, to overcome mass-transport barriers in thick electrodes. In particular, the nature of the carbon paper enables the measurement of the intrinsic electrode's mechanical properties, which is the focus of the study reported here. Furthermore, Al and P50 current collectors have a similar areal mass of 4.5 and 5.0 mg·cm^{-2}, respectively. Therefore, from a gravimetric point of view, the overall sulfur content is not sacrificed. The high-magnification SEM image (**Figure 5.5B**) and EDX analysis (**Figures 5.5C** and **5.5E**) of the representative poly(AETMAC-*co*-EGDA)-based sulfur electrode show that not only are the materials evenly distributed onto the P50 carbon paper, the overall structure of the cathode also exhibits sufficient porosity for the electrolyte penetration.[60] These properties do not exist for Al foil and are vital to showcase the properties of the binder itself, namely, its mechanical properties that enable long-term cycling even at high-sulfur loading, as shown below.

The electrochemical performance of the resulting Li-S cells was examined by galvanostatic cycling (**Figure 5.6**). Electrodes with a low loading of ∼3.5 mg·cm^{-2} (based on sulfur) were first fabricated with different polymeric binders in order to rank the impact of the functional group and the mechanical properties on sulfur utilization and cycling stability before examining high loading Li-S cells. During the first activation cycle at C/20, the poly(AETMAC-*co*-EGDA), poly(DADMAC-*co*-EGDA), and PVDF-

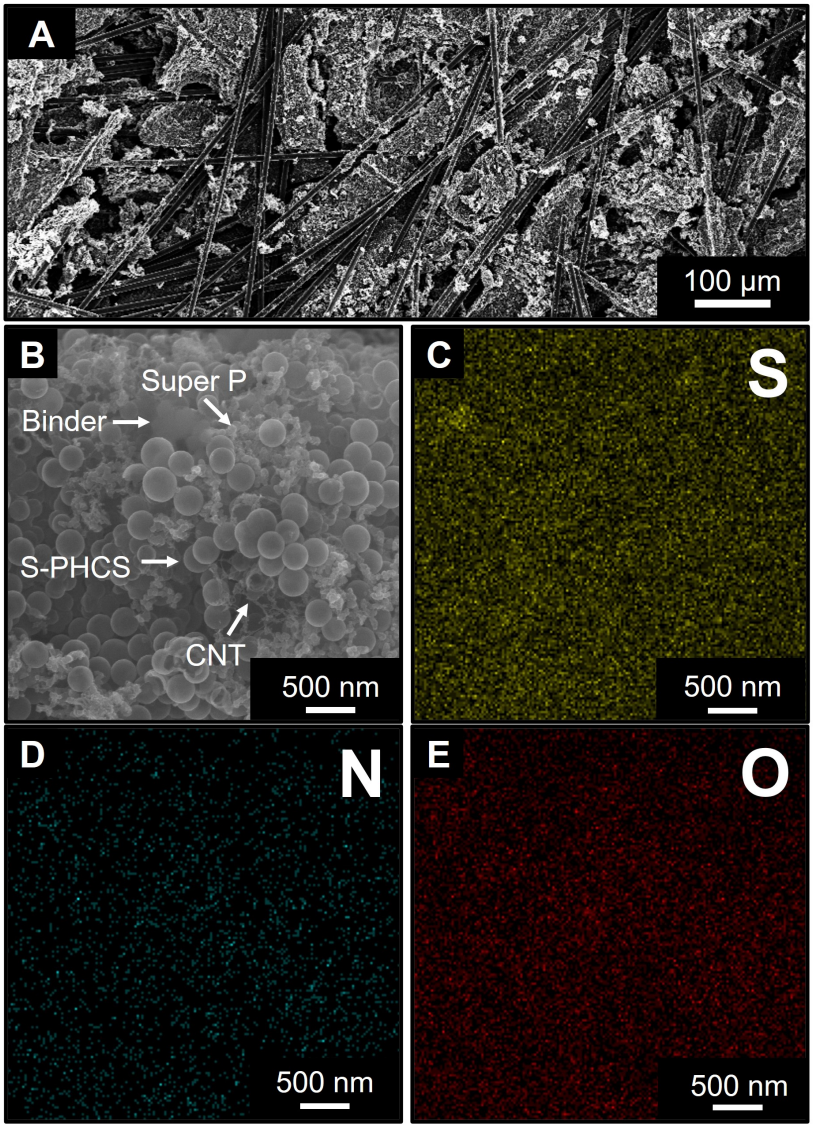

Figure 5.5. SEM and EDX analysis of the S-PHCS cathode fabricated with poly(AETMAC-*co*-EGDA). (A) SEM image of the P50 carbon paper current collector. (B) SEM image of the sulfur cathode fabricated with poly(AETMAC-*co*-EGDA) and its elemental mapping of (C) S; (D) N; and (E) O.

based electrodes exhibit similar discharge capacities of 1115, 1160, and 1175 $mA{\cdot}h{\cdot}g^{-1}$, respectively (**Figure 5.6A**). The sloping region below ~1.8 V *vs.* Li/Li^+ is due to the electrode's passivation from slight reduction of $LiNO_3$ additive on the first cycle.[117] CV studies on these cathodes (**Figure 5.7**) further confirm the galvanostatic cycling results and show that the electrochemical profiles of these cathodes exhibit a typical two-peak discharge step behavior corresponding to the formation of high-order polysulfides at ~2.3 V and nucleation/precipitation of insoluble Li_2S at ~2.1 V *vs.* Li/Li^+.[151, 167]

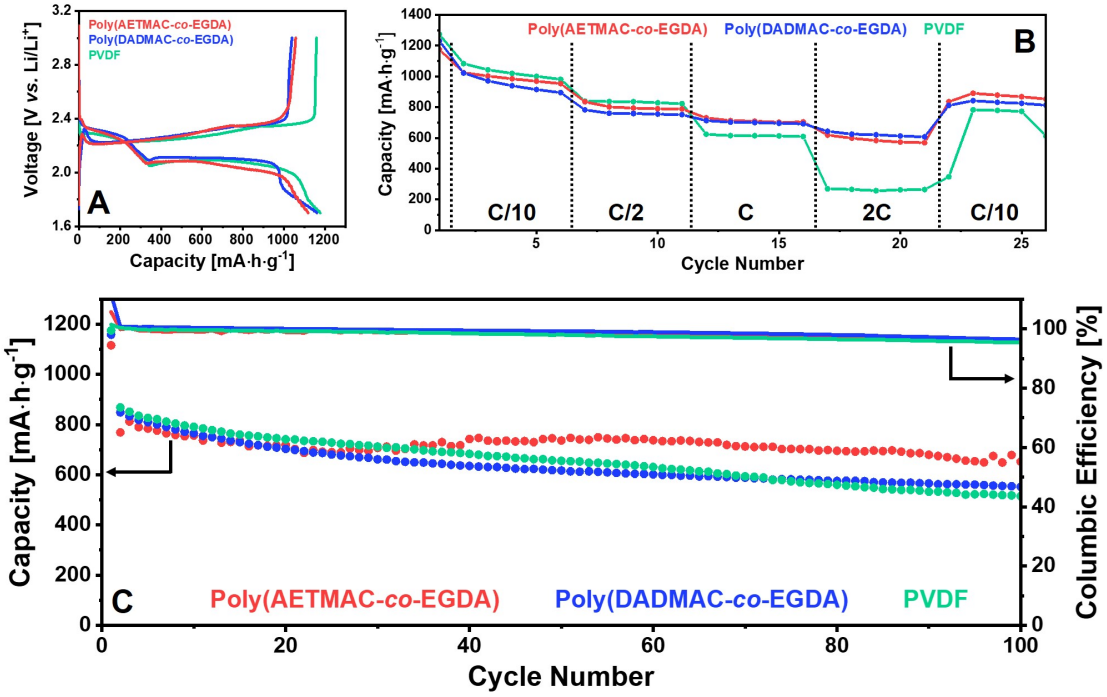

Figure 5.6. Electrochemical profiles for the S-PHCS cathodes fabricated with the polymeric binders at high-sulfur loading of 3.5 $mg{\cdot}cm^{-2}$. (A) Electrochemical profiles (C/20); (B) discharge capacities at different C-rates; and (C) long-term cycling stability conducted at a C/5 rate.

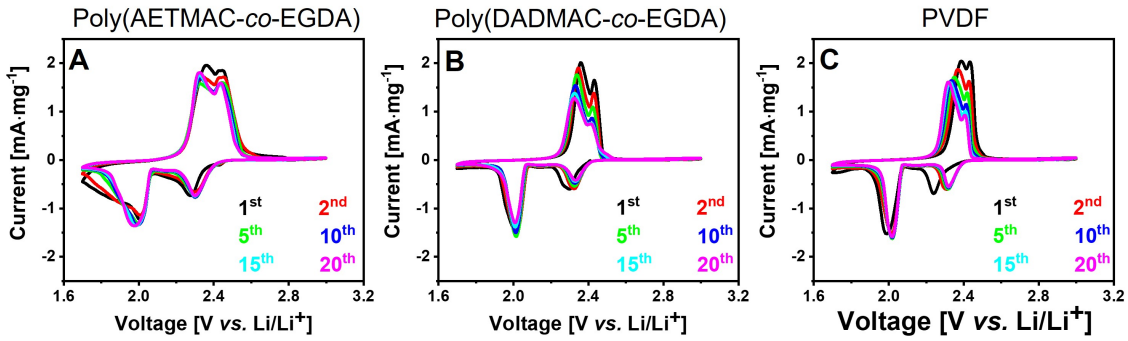

Figure 5.7. CV profiles of the S-PHCS cathodes fabricated with different polymeric binders: (A) poly(AETMAC-*co*-EGDA), (B) poly(DADMAC-*co*-EGDA) and (C) PVDF, shown at different sweep cycles. The scan rate was maintained at $0.1\,\mathrm{mV{\cdot}s^{-1}}$. The small reduction in hysteresis between the 1st and subsequent cycles, most evident for PVDF, is ascribed to changes incurred on fully wetting the electrode on the first cycle.

The discharge capacity of these cathodes at different C-rates is compared in **Figure 5.6B**. The Li-S cells fabricated with either polyelectrolytes exhibit a reversible capacity of $\sim$600 $\mathrm{mA{\cdot}h{\cdot}g^{-1}}$ at 2C. The capacity recovered to $\sim$850 $\mathrm{mA{\cdot}h{\cdot}g^{-1}}$ when the C-rate reverted to C/10. In sharp contrast, the capacity of the PVDF-based Li-S cell drop to 250 $\mathrm{mA{\cdot}h{\cdot}g^{-1}}$ at 2C and show capacity fluctuation during subsequent cycling at C/10. Here, the carbon spheres only provide physical confinement for the polysulfides by limiting diffusion, but these sulfur species can be ultimately solubilized in the electrolyte.[9, 155, 168] For this reason, the electrode with the PVDF binder only retain 52 % capacity over 100 cycles (**Figure 5.6C**), whereas electrodes prepared with the poly(AETMAC-*co*-EGDA) and poly(DADMAC-*co*-EGDA) binders retain 85 and 65 % of their initial capacities, respectively. Their high concentration of ammonium cations forms a 3D network of interacting sites to more effectively bind polysulfide anions.[155, 157] Nonetheless, the behaviour of these two cross-linked binders diverge

after 30 cycles. Although the capacity of the cathodes fabricated with poly(DADMAC-*co*-EGDA) continues to decline past this point, that of poly(AETMAC-*co*-EGDA) remained relatively constant. This is reflected in the more invariant CV profiles exhibited for the sulfur cathode fabricated with poly(AETMAC-*co*-EGDA) (**Figure 5.7A**; after the first *activation* cycle) in comparison with the evolving nature of the CV observed for poly(DADMAC-*co*-EGDA) (**Figure 5.7B**). These binders do not display a drastic difference in polysulfide adsorptivity and share the same cross-linker in optimized cross-linking density. The underlying difference lies in their mechanical properties, as discussed below.

5.6 Importance of Mechanical Properties in Polymeric Binder for Li-S Cell Longevity

The swellability of the polymers was studied by soaking them in DOL/DME (1:1 v/v). The change in the weight corresponding to the solvent uptake was monitored after extracting the solid at different contact times. The weight gain was calculated according to **Equation 5.1**

$$\frac{W_{wet} - W_{dry}}{W_{dry}} \times 100\% \qquad 5.1$$

where W_{dry} is the weight of the dry polymer and W_{wet} is the weight after soaking. This value provides a rough estimate of the polymer-solvent interactions (**Figure 5.8A**). Poly(AETMAC-*co*-EGDA) was fabricated with a lower cross-linker ratio (4:1 molar ratio of AETMAC:EGDA) and swelled far less (∼60 wt. %) than PVDF (∼140 wt. %)

but also less than poly(DADMAC-*co*-EGDA) (∼180 wt. %), which was prepared with a higher cross-linker ratio of 2:1 mole ratio of DADMAC:EGDA. This is attributed to the large chain transfer constant of the allylic DADMAC monomers, which interferes with the growth of an extended network.[169] It results in a much looser network and higher swellability compared to the AETMAC network. The lower degree of swelling and higher chemical stability observed in poly(AETMAC-*co*-EGDA) are important binder characteristics to maximize the acid-base interactions between ammonium cations and polysulfides anions.[155] This is particularly important for high-sulfur loading cathodes, where cell performance is strongly dependent on the amount of liquid electrolyte available.[170] A moderate degree of polymeric binder swelling can result in superior electrochemical performance,[155, 171] the high swelling observed for both PVDF and poly(DADMAC-*co*-EGDA) leads to the uptake of significant amounts of liquid electrolyte. Consequently, the polymer no longer binds the electrode components. Furthermore, in the case of poly(DADMAC-*co*-EGDA), extensive swelling weakens the interactions between the ammonium chloride and lithium polysulfides, which hinders the entrapment of polysulfides. Thus, poly(DADMAC-*co*-EGDA) adsorbs less Li_2S_n than poly(AETMAC-*co*-EGDA), as demonstrated in **Figure 5.2E**

The sulfur electrode fabricated with poly(AETMAC-*co*-EGDA) also better supports the continuous stress during cycling. The tensile strength, as well as the Young's modulus and toughness of the cathodes (cut into rectangles 3" × 1"), were evaluated on a tensometer. The force and the displacement recorded in real time were used to calculate

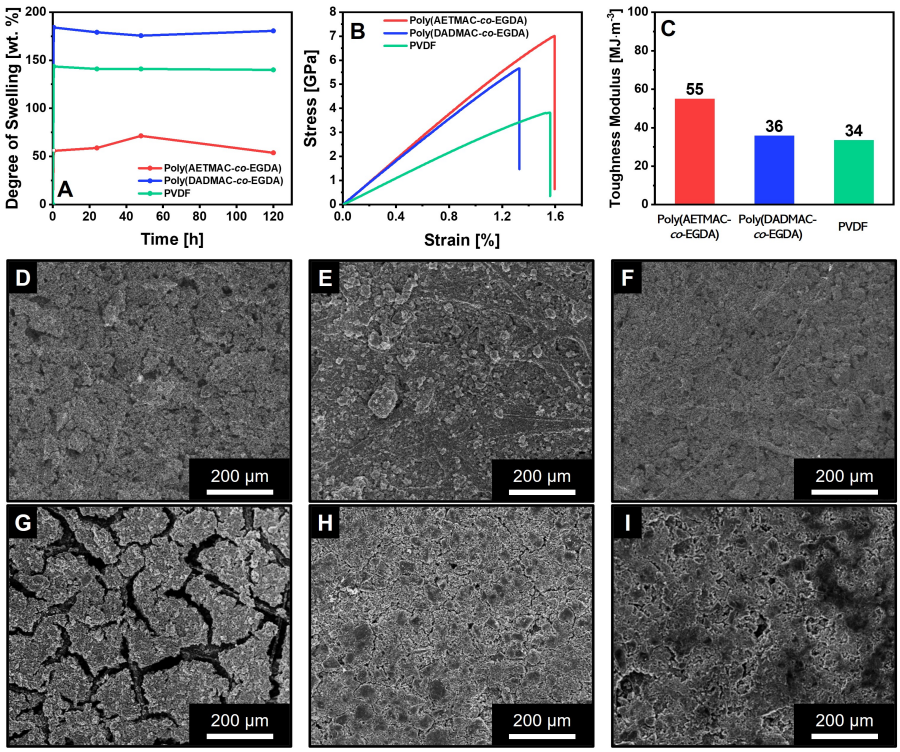

Figure 5.8. Mechanical properties and topological SEM images of the S-PHCS cathodes during cycling. (A) Time-dependent swelling profiles for the polymers in the electrolyte (DOL/DME, 1:1 v/v). (B) Tensile stress-strain curves and (C) toughness of sulfur cathodes using these polymeric binders on P50 carbon paper, until fracture. SEM images of the surface of the sulfur cathodes (D-F) before and (G-I) after 100 cycles fabricated with (D, G) PVDF; (E, H) poly(DADMAC-*co*-EGDA); and (F, I) poly(AETMAC-*co*-EGDA).

the stress (σ_{Young}), given by **Equation 5.2**:

$$\sigma_{\text{Young}} = \frac{F_z - F_{z_0}}{A} \tag{5.2}$$

where F_z and F_{z_0} are the forces experienced by the electrode during the experiment and at the beginning of the experiment, respectively. A is the cross-sectional area of

the electrode. For a 1" width P50 carbon paper with a sulfur loading of 3.5 mg·cm^{-2}, the cross-sectional area of the specimen was 7 mm^2. The strain (ϵ_{strain}) was calculated according to **Equation 5.3**:

$$\epsilon_{strain} = \frac{x_z - x_{z_0}}{x_{z_0}} \times 100\% \tag{5.3}$$

where x_z and x_{z_0} are the distances between the two grip heads while the electrode was being stretched.

The stress-strain curves for these electrodes in **Figure 5.8B** show a profile typical of fiber nanocomposites: a linear curve that obeys Hooke's law, followed by a sudden drop in stress.[172] This sharp decrease in stress corresponds to the tearing of the P50 paper when the maximum stress is exceeded, and provides the value of the tensile strength. The poly(AETMAC-*co*-EGDA)-based electrode exhibits the highest tensile strength (7.0 GPa), compared to the electrodes prepared from poly(DADMAC-*co*-EGDA) (5.7 GPa) and PVDF (3.8 GPa). Furthermore, the Young's modulus of the electrode fabricated from the two cross-linked binders is very similar (4.5 GPa), and greatly improved over the PVDF (2.5 GPa). The cross-linked binders form a 3D network that also improve the connectivity between the cathode components (S-PHCSs and carbon additives) and the carbon fibers in the P50 carbon paper. This material entanglement decreases the likelihood of delamination during cycling and stiffens the electrode structure, thus improving the tensile strength and Young's modulus.[151, 173]

Toughness (U) is an intrinsic property that describes the energy of mechanical deformation per unit volume prior to fracture. It provides a metric to gauge the durability

of the electrode and is calculated by integrating the area under the stress-strain curve, as described in **Equation 5.4**:[174]

$$U = \int_{x_{z_r}}^{x_{z_0}} \sigma_{\text{Young}} \times \frac{x_z - x_{z_0}}{x_{z_0}} \, dx_{z_z} \tag{5.4}$$

where x_{z_r} is the distance between the two grip heads when the electrode ruptures.

The toughness measured for sulfur electrodes with different binders is compared in **Equation 5.4**. The electrode prepared with poly(AETMAC-*co*-EGDA) exhibit the highest value of 55 $\text{MJ}\cdot\text{m}^{-3}$. Both poly(DADMAC-*co*-EGDA) (36 $\text{MJ}\cdot\text{m}^{-3}$) and PVDF (34 $\text{MJ}\cdot\text{m}^{-3}$) exhibit similar but much lower toughness. This suggests that at the same sulfur and carbon additive loading, poly(AETMAC-*co*-EGDA) forms a more resilient 3D network with the S/C composite, providing superior mechanical bonding compared to the other two polymers.

SEM studies were carried out before (**Figure 5.8D - 5.8F**) and after cycling (**Figure 5.8G - 5.8I**) to validate the impact of the mechanical properties in maintaining cathode architecture. Cross-sectional areas of these electrodes (**Figure 5.9**) were also examined to investigate electrode material delamination from the current collector. The low-magnification SEM images in **Figure 5.8D - 5.8F** show that all three electrodes were relatively flat and free of cracks. Furthermore, the cross-sectional SEM images in **Figure 5.9A - 5.9C** show that most of the cathode materials penetrated a few tens of microns into the carbon fiber matrix. Upon cycling, the PVDF-based electrode (**Figure 5.8G**) shows large cracks. This is accompanied by severe delamination of the cathode material from the P50 current collector, as shown in the cross-

sectional area SEM image upon cycling at C/5 for 10 cycles (**Figure 5.9D**). This is attributed to the fact that PVDF exhibits the lowest tensile strength, Young's modulus, and toughness among the binders studied and thus cannot support drastic volume changes upon cycling. On the other hand, electrodes cast with the poly(DADMAC-*co*-EGDA) binder exhibit fewer cracks and less material delamination under identical cycling conditions (**Figure 5.8H** and **5.9E**). This is due to the higher tensile strength and Young's modulus resulting from the incorporation of cross-linker (EGDA). Furthermore, the improved capacity retention benefited from the large number of active sites in the polymer network, and provides additional polysulfide chemisorption. However, the highly swollen poly(DADMAC-*co*-EGDA) network is unable to maintain uniform interaction with lithium polysulfides, causing the capacity of the electrode to diminish rapidly (**Figure 5.6C**). The architecture of the poly(AETMAC-*co*-EGDA)-based electrode remained intact upon deep cycling (**Figure 5.8I** and **5.9F**). This further confirms that the individual S/C composite particles were strongly bound to the current collector. In summary, the low swelling capability of poly(AETMAC-*co*-EGDA) ensures sufficient interactions between its ammonium cations and the polysulfide anions. This cross-linked polymer also conveys a higher tensile strength, stiffness, and toughness to the electrode for increased tolerance to delamination, and favours electrode durability.

To further correlate the electrochemical performance with the mechanical properties of the sulfur electrodes fabricated with these binders, EIS studies were performed during cycling (**Figure 5.10**). The interfacial resistance of both the PVDF- and poly(DADMAC-*co*-EGDA)-based electrodes increase during the first 50 cycles. This is in strong agreement with the SEM analysis (see surface topology in **Figure 5.8**

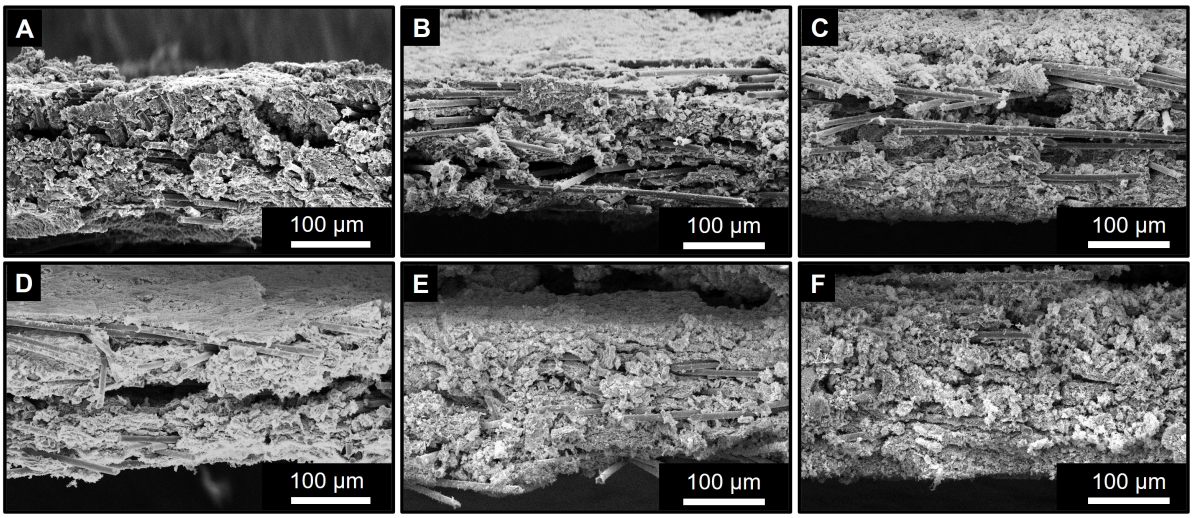

Figure 5.9. Cross-sectional SEM images of the S-PHCS cathodes during cycling. (A-C) before and (D-F) 10 cycles fabricated with (A, D) PVDF; (B, E) poly(DADMAC-*co*-EGDA); and (C, F) poly(AETMAC-*co*-EGDA).

and cross-section in **Figure 5.9**), which suggests that the architecture of these electrodes slowly deteriorates as a result of their inferior physical properties. In contrast, the EIS of the poly(AETMAC-*co*-EGDA)-based electrode (**Figure 5.10C**) remained largely unchanged. This indicates that although both poly(DADMAC-*co*-EGDA) and poly(AETMAC-*co*-EGDA) contain ammonium cation subunits that engage in charge transfer interactions with the polysulfide anions,[159, 175] the latter polymer provides superior mechanical binding strength towards the cathode components as well as the current collector, preserving the electrode integrity during cycling.

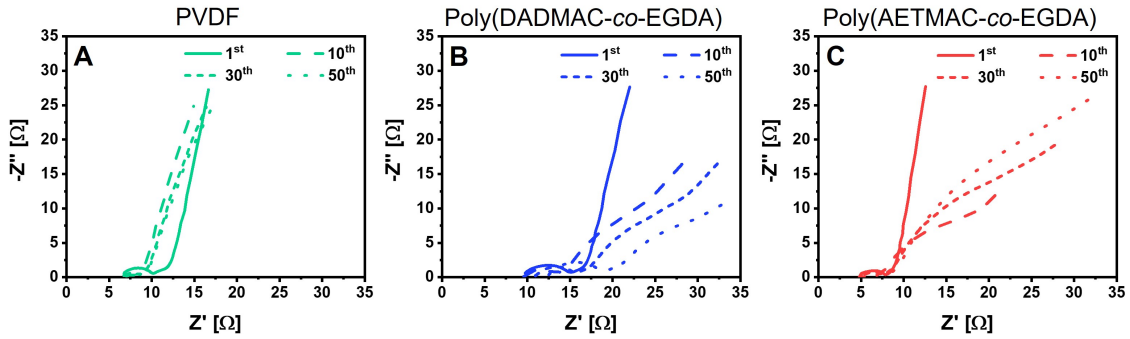

Figure 5.10. Nyquist plots of the S-PHCS cathodes at different cycle numbers: (A) PVDF, (B) poly(DADMAC-*co*-EGDA), and (C) poly(AETMAC-*co*-EGDA).

5.7 Electrochemistry with High Sulfur Loading Electrodes

High-sulfur loading (6.0 mg·cm^{-2}) electrodes were fabricated using these binders as a further proof-of-concept. All cathodes were maintained at open circuit voltage for 4 hours prior to cycling to allow equilibrium swelling of the binder. Due to the thickness of the electrodes, these cathodes were conditioned at low current density of C/50 for one cycle, where all cathodes exhibit a similar initial discharge capacity between 800 and 1000 mA·h·g^{-1} or areal capacity between 4.5 and 5.6 mA·h·cm^{-2} before switching to cycling at C/10. On the first cycle at C/10, specific capacities of 905, 710, and 640 mA·h·g^{-1} or areal capacities of 5.4, 4.0, and 3.7 mA·h·cm^{-2} are obtained for electrodes fabricated with poly(AETMAC-*co*-EGDA), poly(DADMAC-*co*-EGDA), and PVDF, respectively (**Figure 5.11A** and **5.11B**). The initial areal capacities of the cathodes in this study are not as high as for some recently reported 3D-architectured cathodes; however, those cathodes were studied over only 100 cycles using a catholyte-type cell (that is, a high electrolyte:sulfur ratio).[24] Considering the relatively low electrolyte/sulfur

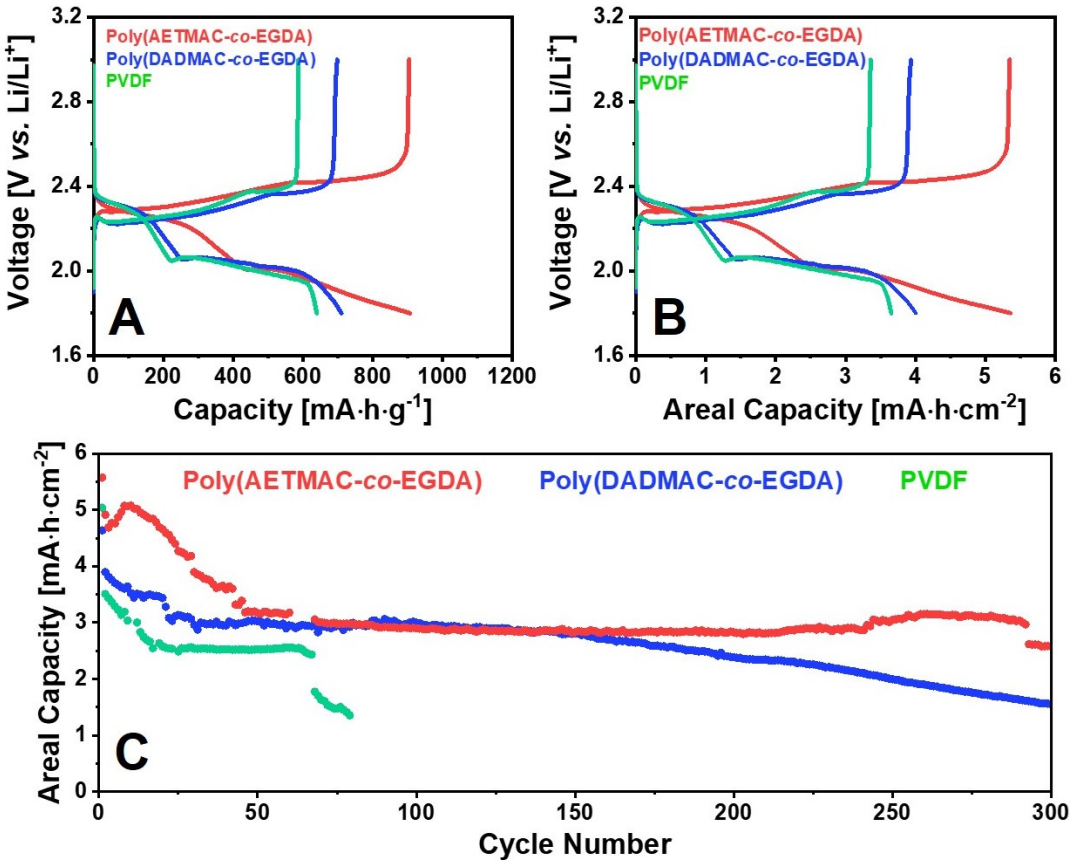

Figure 5.11. Electrochemical profiles for the S-PHCS cathodes fabricated with the polymeric binders at high-sulfur loading of 6.0 mg·cm^{-2}. First discharge/charge voltage profile at a current rate of C/10 as a function of (A) mass-specific capacity and (B) areal capacity. (C) Long-term cycling at C/10 for the same sulfur cathodes (the 1st conditioning cycle is at C/50). The CE for the polyelectrolyte binders over the cycling duration was ~90 %.

(7:1) ratio used in this study, the approach is promising for higher energy density Li-S cell applications.

Long-term cycling of the electrodes over 300 cycles (**Figure 5.11C**) provides further insight into the ability of the binder to stabilize the cycling of high loading Li-S cells. The

PVDF based electrode shows fluctuation in capacity with rapid fading. The capacity drop after 60 cycles indicates cumulative surface passivation from randomly precipitated Li_2S/S_8 materials on the electrode surface, which becomes pronounced at the 79^{th} cycle and causes cell death. However, the sulfur cathodes fabricated with poly(DADMAC-*co*-EGDA) and poly(AETMAC-*co*-EGDA) exhibit good reversible discharge areal capacities over the first 150 cycles. The gradual capacity decay experienced on continued cycling ($>$ 150 cycles) of the poly(DADMAC-*co*-EGDA)-based sulfur cathode is ascribed to its high degree of swelling as well as to the low tensile strength and toughness of the polymer. At such a high degree of swelling, the ammonium cations may interact with the solvent molecules as much as with the polysulfides. The poly(AETMAC-*co*-EGDA)-based electrode reaches a higher capacity of $5\,mA{\cdot}h{\cdot}cm^{-2}$ (after the first few conditioning cycles needed to fully wet the electrode)[60, 176, 177] and ultimately stabilizes at $\sim 3\,mA{\cdot}h{\cdot}cm^{-2}$ on the 50^{th} cycle. Most importantly, capacity retention is excellent over the latter cycling period.

5.8 Conclusion

This chapter demonstrates the importance of cross-linked polymeric binders with both strong chemisorption and robust mechanical properties, utilizing poly(AETMAC-*co*-EGDA) as a model system, for the fabrication of stable and high loading sulfur cathodes. The combination of a 3D network in the cross-linked polymer and strong charge-transfer interactions between the quaternary ammonium groups and polysulfides lead to very significant improvement in the electrochemical performance compared with a

simple linear polymer binder such as PVDF. The tighter polymer network, compared to poly(DADMAC-*co*-EGDA), which contains similar chemical functionality, reduces electrolyte swelling and increases the tensile strength, Young's modulus, and toughness. These factors are all critical for delamination tolerance. Excellent capacity retention over 300 cycles for compact thick electrodes ($6.0\,\mathrm{mg{\cdot}cm^{-2}}$) is exhibited in Li-S cells with a moderate electrolyte-sulfur ratio. Moreover, traditional slurry processes can be used to cast the cathode material onto the current collector, which fits industrial protocols. These findings should inspire the battery community to place more focus on utilizing highly functional binders to achieve high areal capacity in Li-S cathodes.

Chapter 6

Lithium-Oxygen Battery Based on a Reversible Four-Electron Conversion

6.1 Introduction

As discussed in the **Section 1.4**, aprotic Li-O_2 battery is heavily plagued by the decomposition of organic electrolytes as well as by the corrosion of the porous carbon cathode hosts as a result of (su)peroxides attacks.[63, 178, 179, 180] Although effort has been made to improve the cycling performance of such battery system - albeit by means of a complex and debated pathway[181, 182] or novel cathode/electrolyte systems[67, 74] - the fundamental issues remain. In comparison with peroxide and superoxides which are known to react with organic electrolyte and carbon cathodes,[66, 180] Li_2O is benign as an oxidizing agent owing to the oxidation state of its oxide anion being -2. Therefore it does not react with DMSO for example, whereas Li_2O_2 oxidizes DMSO to form dimethyl sulfone (**Figure 6.1**). More importantly, Li-O_2 cells based on Li_2O as the

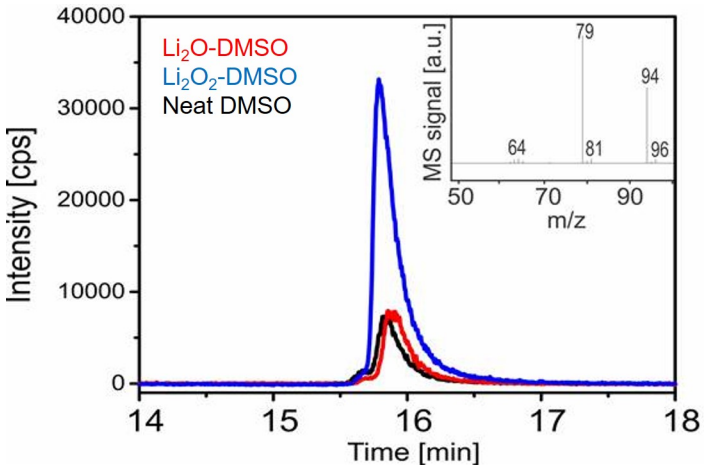

Figure 6.1. Quantitative gas chromatography-mass spectrometry (GC-MS) results of the reaction of DMSO with oxygenated species. Li_2O (red), and Li_2O_2 (blue) for 300 h, compared to neat DMSO (black). The GC trace shows the eluted fraction from the column that corresponds to methylsulfonylmethane, as proven by MS analysis (inset).

discharge product doubles its can theoretically deliver a high specific energy and energy density of 5.2 $kW{\cdot}h{\cdot}kg^{-1}$ and 10.5 $kW{\cdot}h{\cdot}L^{-1}$, respectively, exceeding that of fossil fuels (gasoline, 9.5 $kW{\cdot}h{\cdot}L^{-1}$) because it invokes a four-electron transfer.

Therefore, it is of much interest to seek a pathway for reversible oxygen reduction to lithium oxide. Consideration of the thermodynamics of the ORR shows that not only is standard Gibbs reaction energy ($\Delta_r G^\circ$) of the lithium peroxide formation (**Equation 6.1**, $-571\,kJ{\cdot}mol^{-1}$) is lower than that of the lithium oxide (**Equation 6.2**, $-561\,kJ{\cdot}mol^{-1}$),[183] but the formation of oxide also requires O-O bond cleavage of oxygen molecules, whereas peroxide does not. In other words, the formation of Li_2O_2, not Li_2O, is thermodynamically and kinetically favoured at ambient conditions. In this chapter, I demonstrate that by increasing the operating temperature and exploiting stable inorganic electrolytes and ORR/OER catalysts, the reversible formation of Li_2O leads to

a highly rechargeable Li-O_2 cell with high high capacity, low overpotential with transfer of 4 e^-/O_2, and excellent cycling performance.

$$2Li + O_2 \rightarrow Li_2O_2 \qquad \Delta_r G^\circ = -571\,kJ{\cdot}mol^{-1} \tag{6.1}$$

$$2Li + \frac{1}{2}O_2 \rightarrow Li_2O \qquad \Delta_r G^\circ = -561\,kJ{\cdot}mol^{-1} \tag{6.2}$$

6.2 Experimental Methods

6.2.1 Preparation of $LiNO_3$-KNO_3 Molten Salt Electrolyte

The molten nitrate salt electrolyte was composed of lithium nitrate (99.99 %, Sigma-Aldrich) and potassium nitrate (99.0 %, Sigma-Aldrich) with a mole ratio of 42:58, which forms a eutectic.[69, 70] Since the glass fiber separator (Whatman) was poorly wetted by the molten nitrate, the electrolyte filled separator was prepared by immersing the glass fiber paper in an aqueous solution of $LiNO_3$-KNO_3 at a salt concentration of $0.25\,mg{\cdot}mL^{-1}$. The wetted glass fiber discs with a diameter of 12 mm were placed in a 180 °C oven for 20 min to evaporate water and allow the absorbed nitrates to melt to form a molten salt. This process was iterated several times until all of the pores in the glass fiber were filled. The mass loading of the electrolyte was 100 ± 10 mg per glass fiber. After the electrolyte-filled separators were vacuum-dried at 200 °C for 24 h in a Büchi vacuum oven, they were then transferred into a glovebox for cell assembly.

6.2.2 Preparation of LAGP Solid Electrolyte

LAGP was synthesized via a solid-state reaction. First, 2.65 g Li_2CO_3 (ACS reagent, Sigma-Aldrich), 1.22 g Al_2O_3 (Sigma-Aldrich), 7.51 g GeO_2 ($\geq$ 99.99%, Sigma-Aldrich), and 16.52 g $NH_4H_2PO_4$ (99.999 %, Sigma-Aldrich) precursors were ball-milled with acetone at 250 RPM for 4 h using agate mortar balls (6 mm, 5 g). The obtained mixture was then dried in a 60 °C oven for 12 h to remove the solvent. The white powders were then calcined at 600 °C in air for 4 h to decompose the precursors. The subsequent light grey powders were ball-milled at 250 RPM for 4 h, followed by pelletization at an applied pressure of 3 tons. The square pellet (0.4 cm^3) was then calcined at 900 °C in air for 6 h. Another ball-milling procedure was employed to grind the pellets, and the resulting particles were sieved to a dimension smaller than 106 µm in diameter. The solid electrolyte powder (1 g) was pressed under 5 tons for 1 min. The resulting white disc was sintered at 900 °C in air for 10 h, with heating and cooling rates of 1 °C·min^{-1}.

6.2.3 Preparation of Ni-$LiNO_3$-KNO_3 Composite Cathode

Typically, 4 g Ni powder (Anachemia) was mixed with 4 mL of $LiNO_3$-KNO_3 aqueous solution (0.25 mg·mL^{-1}). The mixture was then heated in an oven at 180 °C for 20 min to remove water and to form a thin layer of the molten nitrate on the Ni nanoparticles. Finally, 200 mg of the Ni-$LiNO_3$-KNO_3 composite cathode powder were pressed onto a stainless steel current collector (SS316) under an applied pressure of 1 ton. The geometric area of the cathode was 1 cm^2. The cathodes were further dried at 200 °C for

one day in a Büchi vacuum oven prior to use.

6.2.4 Preparation of Li_2O_2-prefilled Electrode

In an Ar-filled glovebox, the pre-filled electrode was prepared by grinding and mixing 200 mg of the Ni-$LiNO_3$-KNO_3 composite material and 50 mg of the commercial Li_2O_2 powder (technical grade, Sigma-Aldrich) in a mortar. The mixture powder was then pressed onto a stainless steel current collector (SS316) under an applied pressure of 1 ton. The geometric area of the electrode was 1 cm^2.

6.2.5 Preparation of Li_2O-prefilled Electrode

In an Ar-filled glovebox, the pre-filled electrode was prepared by grinding and mixing 200 mg of the Ni-$LiNO_3$-KNO_3 composite material and 50 mg of the commercial Li_2O powder (Sigma-Aldrich) in a mortar. The mixture powder was then pressed onto a stainless steel current collector (SS316) under an applied pressure of 1 ton. The geometric area of the electrode was 1 cm^2.

6.2.6 Determination of Li_2O Solubility in Molten Nitrate

The solubility of Li_2O in the molten nitrate was measured using a home-made apparatus. Commercial Li_2O powder (1 g) was added to the 20 g $LiNO_3$-KNO_3 eutectic mixture and placed in a glass beaker. The eutectic nitrate mixture (4 g) alone was also placed into a separate container whose bottom was sealed with a glass fiber membrane. The

apparatus was assembled in an Ar-filled glovebox by inserting the container into the glass beaker. The apparatus was heated at 150 °C under vacuum to melt the eutectic. A glass pipette was inserted into the container to extract the molten nitrate for the solubility measurement, and the amount of Li_2O in the eutectic was quantified by titration. As shown in **Table 6.1**, the solubility of Li_2O molten nitrate was 27.6mM at 150 °C.

Table 6.1. Li_2O solubility in $LiNO_3$-KNO_3 molten salt electrolyte at 150 °C.

Time [h]	Solubility [mM]
24	30.8
48	23.3
72	28.8
Average	**27.6 ± 4.0**

6.2.7 GC-MS Analysis for the Chemical Stability of Li_2O and Li_2O_2 in DMSO

DMSO (anhydrous, ≥99.9 %, Sigma-Aldrich) was distilled under partial pressure and stored over molecular sieves (3 Å, beads 8 - 12 mesh, Sigma-Aldrich) for two days prior to use. In an Ar-filled glovebox, commercial Li_2O and Li_2O_2 powders were mixed with 6.2 mL of the purified DMSO. The stoichiometric mole ratio between the commercial powders and DMSO was kept at 1:100. The resulting suspensions were stirred using a magnetic stir bar for 300 hours, followed by centrifugation (10 kRPM, 10 min) to remove the solids. The supernatant was collected and further diluted in acetonitrile (1:10 vol. %) before GC-MS analysis. Single-ion monitoring mode was utilized to enhance the sensitivity of dimethyl sulfone signal.

6.2.8 Quantification of the Discharge Products

Preparation of the cathode for quantification. After disassembling the cell, the cathode was removed from the glovebox and transferred into a glass vial filled with 3 mL water. After 5 min of sonsication, the solution was filtered to remove the insoluble Ni nanoparticles. The resulting transparent solution was used for the quantification of Li_2O_2 and Li_2O.

Lithium peroxide. The quantification of Li_2O_2 was accomplished by first hydrolyzing Li_2O_2 to form LiOH and H_2O_2 (**Equation 6.3**), followed by an oxidation of $TiOSO_4$ by hydrogen peroxide (**Equation 6.4**). The final yellow coloured product (TiO_2SO_4) has an adsorption peak at 405 nm, detected by an UV-vis spectrometer.[184] The calibration curve for H_2O_2 detection was established by preparing a stock solution of H_2O_2 (30 wt. % in H_2O, Sigma-Aldrich) in water at varying concentrations. The H_2O_2 (0.5 mL) and $TiOSO_4$ (0.5 mL, 15 wt. % in dilute sulfuric acid, Sigma-Aldrich) were added to a poly(methyl methacrylate) cuvette. The exact procedure was followed when quantifying the cathode solution.

$$Li_2O_2 + 2H_2O \rightarrow 2LiOH + H_2O_2 \tag{6.3}$$

$$H_2O_2 + TiOSO_4 \rightarrow TiO_2SO_4 + H_2O \tag{6.4}$$

Lithium oxide. The quantification of Li_2O was accomplished by first hydrolyzing Li_2O to form LiOH (**Equation 6.5**) that was titrated with HCl (**Equation 6.6**). The total alkalinity of the solution (n_{all}), via hydrolysis, was comprised of two components: Li_2O_2 ($n_{Li_2O_2}$) and Li_2O (n_{Li_2O}). Prior knowledge on the amount of Li_2O_2 in the solution

computes the total amount of Li_2O as shown in **Equation 6.7**:

$$Li_2O + 2H_2O \rightarrow 2LiOH \tag{6.5}$$

$$LiOH + HCl \rightarrow LiCl + H_2O \tag{6.6}$$

$$n_{Li_2O} = \frac{1}{2} \times (n_{all} - 2n_{Li_2O_2}) \tag{6.7}$$

6.3 Cell Configuration

According to the Gibbs-Helmholtz equation, the formation of Li_2O as the discharge product, rather than Li_2O_2, is only thermodynamically favoured at temperature above 150 °C (**Figure 6.2A**). To achieve this, lithium nitrate/potassium nitrate ($LiNO_3$-KNO_3) eutectic molten salt was utilized as the liquid electrolyte because it exhibits an eutectic point of 125 °C and possess good chemical stability and high conductivity.[70]. A non-porous $Li_{1.5}Al_{0.5}Ge_{1.5}(PO_4)_3$ (LAGP) solid electrolyte was further employed at the Li anode to inhibit the cross-over of soluble products. The overall cell design in shown in **Figure 6.2B**.

Moreover, I employ a non-carbonaceous composite cathode composed of Ni nanoparticles coated *in-situ* to form Li_xNiO_2, which serves as the vital electrocatalyst that reversibly catalyzes O-O bond cleavage and formation. The SEM image in **Figure 6.3A** shows the Ni-nitrate composite cathode is composed of Ni nanoparticles and covered by a very thin layer of nitrate melt. XPS analysis on the material further reveals that Ni particles in the composite cathode are covered with two types of oxide species due to the

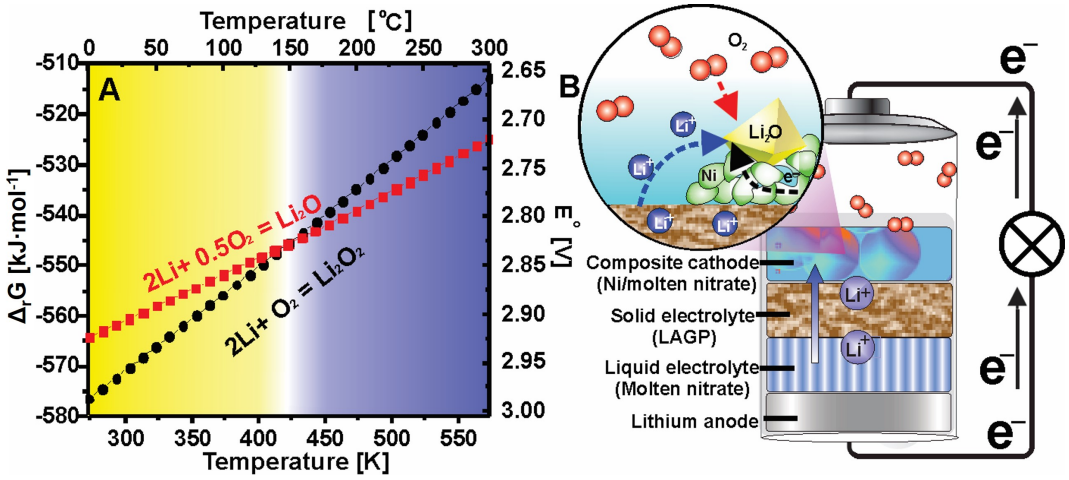

Figure 6.2. Thermodynamics map for Li-O_2 electrochemistry and configuration of the inorganic Li-O_2 battery. (A) Gibbs reaction energy and cell potential for the formations of Li_2O (red) and Li_2O_2 (black) as a function of temperature. The thermodynamic data were calculated according to the database of HSC Chemistry version 5. (B) Configuration of the inorganic electrolyte Li-O_2 cell and schematic illustration of Li_2O formation during discharge.

oxidation of Ni by molten nitrate. The major peak at 855.4 eV in the Ni 2p spectrum (**Figure 6.3C**) is assigned to Ni_2O_3 layer, evidenced by its corresponding O 1s peak at 531.9 eV as shown in **Figure 6.3D**.[185] The formation of lithiated nickel (III) oxide (Li_xNiO_2) electrocatalyst is demonstrated by its characteristic Ni 2p peak at 854.0 eV; O 1s peak at 529.6 eV; and Li 1s peak at 54.9 eV as described in the literature.[186, 187] The peak at 56.0 eV in the Li 1s spectrum is residual $LiNO_3$,[188] attributed to incomplete washing of the sample.

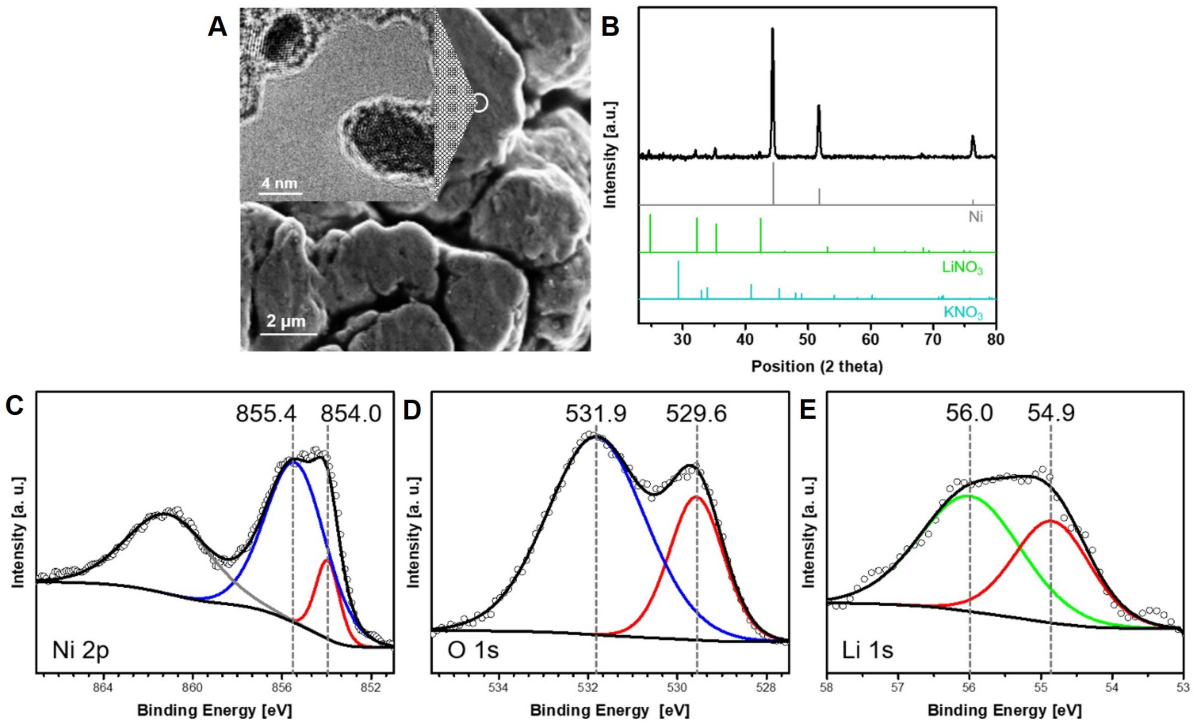

Figure 6.3. Characterization of the Ni-$LiNO_3$-KNO_3 material. (A) SEM image and the corresponding TEM image (inset) and (B) XRD pattern of the Ni-$LiNO_3$-KNO_3 materials. XPS spectra: (C) Ni 2p, (D) O 1s, and (E) Li 1s. Multiplet components were not considered when fitting the Ni 2p spectrum and only the lower binding components of the Ni 2p spectrum are displayed.

6.4 Analysis on Redox Products

Cells were sealed with oxygen (5.0, Praxair) and cycled between 2.6 and 3.5 V *vs.* Li/Li^+ at an applied current of $0.1\,mA{\cdot}cm^{-2}$ at 150 °C. The Li-O_2 cells exhibit a very high discharge capacity of $11\,mA{\cdot}h{\cdot}cm^{-2}$ (**Figure 6.4A**). After fully discharging the cell to 2.6 V, the XRD pattern of the composite cathode shows two peaks at 34° and 56° assigned to the (111) and (002) reflections of Li_2O. (**Figure 6.4B**). A Raman band definitive of Li_2O

at 523 cm^{-1} further supports formation of the oxide as shown in **Figure 6.4C**. The SEM image in **Figure 6.4D** reveals that the discharged cathode is covered with large ~5 µm octahedral crystals, a morphology characteristics of the Li_2O anti-fluorite structure. Because the solubility of Li_2O in molten nitrate is 27 mM at 150 °C (**Table 6.1**), it is speculated that solution-mediated Li_2O transport - as reported in aprotic Li-O_2 and Na-O_2 cells[189, 190] - is responsible for its crystal nucleation and growth. A high initial Coulombic efficiency of 96 % was achieved after recharging the cell to 3.5 V *vs.* Li/Li^+, accompanied by a very low polarization of 0.2 V (**Figure 6.4A**). The disappearance of Li_2O in the XRD (**Figure 6.4B**) and Raman (**Figure 6.4C**) of the recharged cathode indicates Li_2O is fully removed by oxidation. Furthermore, the charged cathode is bare (**Figure 6.4E**), identical to before discharge (**Figure 6.4F**), which further supports excellent electrochemical reversibility.

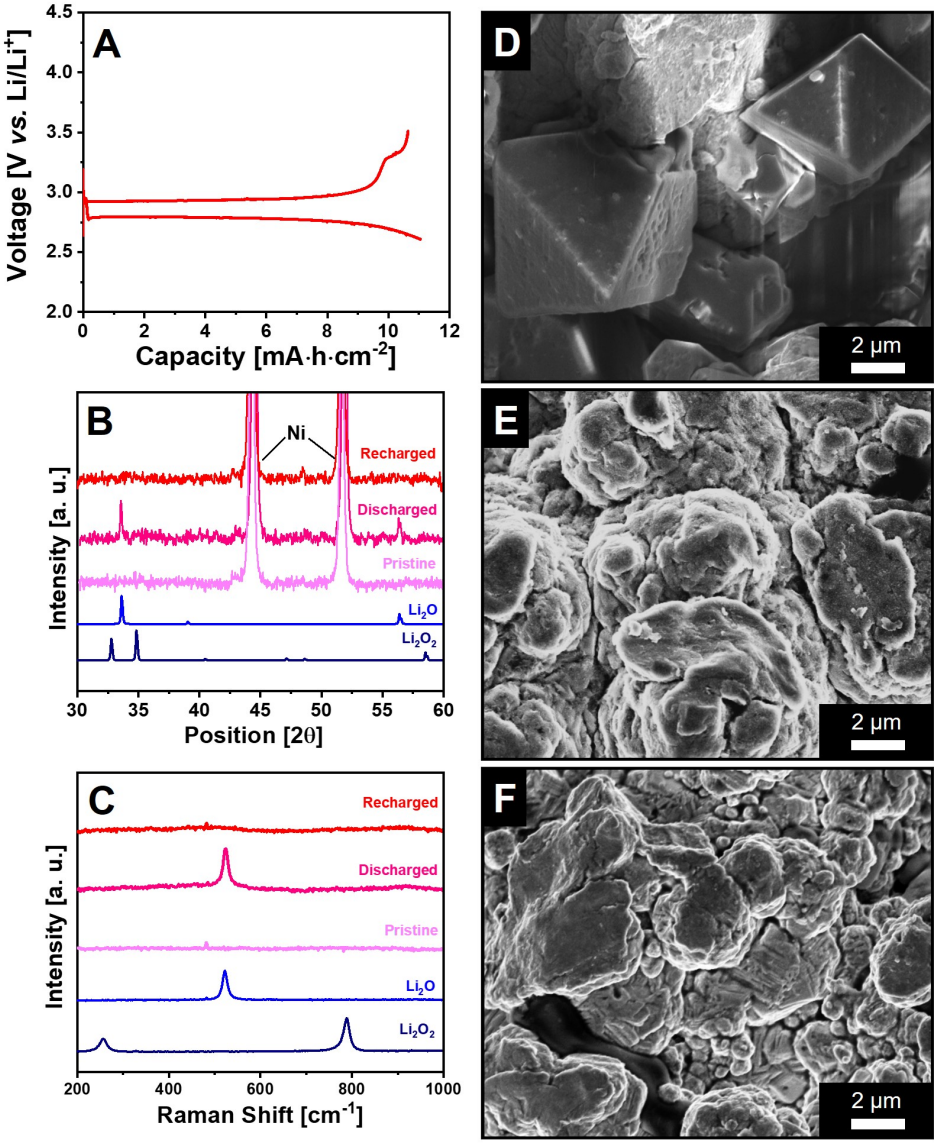

Figure 6.4. Characteristics of the inorganic Li-O_2 battery. (A) Electrochemical profile of the inorganic Li-O_2 cells. The current density was maintained at 0.1 mA·cm^{-2}, and cutoff voltages are 2.6 and 3.5 V. (B) XRD patterns, (C) Raman spectra, and (D - F) SEM images: (D) discharged cathode (2.6 V); (E) recharged cathode (3.5 V); and pristine cathode.

Compositional changes of the redox products at the 1st and 10th cycle were quantified to further examine the electrochemical reversibility of the cell. The cell was first discharged to 2 mA·h·cm^{-2} and recharged to 3.5 V. The results are summarized in **Figure 6.5A**. Unsurprisingly, Li_2O is the main discharge product (36.1 µmol), along with a tiny fraction of Li_2O_2 (1.1 µmol). The total amount of Li_2O and Li_2O_2 (37.2 µmol) is nearly identical to the theoretical value of 37.3 µmol, assuming a $2e^-$ transfer per mole of products (**Equations 6.8** and **6.9**):

$$2Li^+ + \frac{1}{2}O_2 + 2e^- \rightarrow Li_2O \qquad 6.8$$

$$2Li^+ + O_2 + 2e^- \rightarrow Li_2O_2 \qquad 6.9$$

After recharging the cell to 3.5 V, the amount of Li_2O on the cathode is reduced to 2.6 µmol, whereas no Li_2O_2 is observed. The residual Li_2O likely arises from its low solubility in the molten nitrate electrolyte and/or its cross-over to the electrically insulating LAGP membrane, rendering it electrochemically inaccessible in subsequent cycles. This may account to the slight higher Li_2O amount quantified in the 10th cycle. Nonetheless, no other noticeable changes in the product quantity is identified. It can be concluded that the cell exhibit good reversibility.

DEMS monitoring of the gaseous products formed during the 1st (**Figure 6.5B**) and 10th (**Figure 6.5C**) charge sheds some light in the charge mechanism. The first charge profile exhibits two plateaus at 3.0 and 3.3 V (**Figure 6.5B**), in agreement with the cycling profile detailed in **Figure 6.4A**. The rate of O_2 evolution on either plateau is exactly equal to the theoretical value based on $4e^-/O_2$, indicating the electrochemical

oxidation of Li_2O (**Equation 6.10**):

$$2Li_2O \rightarrow 4Li^+ + O_2 + 4e^- \qquad 6.10$$

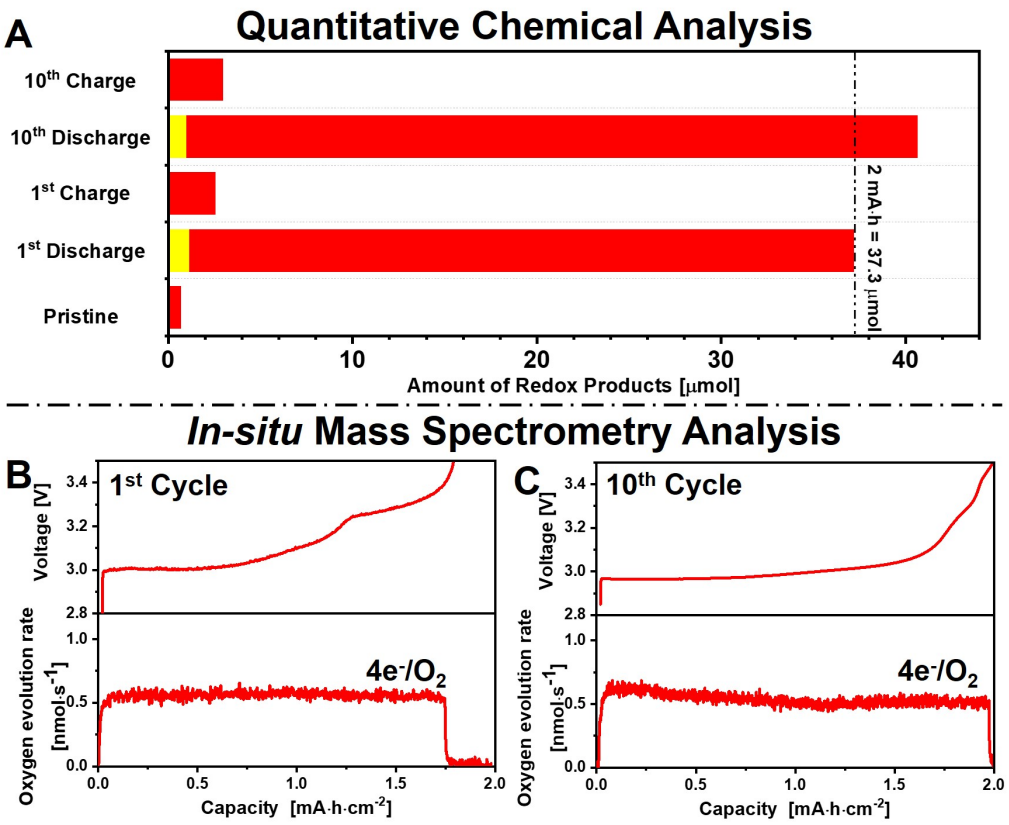

Figure 6.5. High reversibility of inorganic the Li-O_2 battery. (A) Quantitative analysis of the redox products at 1st and 10th cycle: Li_2O (red) and Li_2O_2 (yellow). The discharge capacity limit is 2 mA·h·cm^{-2} and the charge limit is 3.5 V. The current density is 0.1 mA·cm^{-2}. (B - C) DEMS of gaseous oxygen evolution upon (B) 1st charge and (C) 10th charge. The cells were pre-discharged to 2 mA·h·cm^{-2} at 0.1 mA·cm^{-2}. The charging rate was 0.2 mA·cm^{-2} in order to enhance the O_2 mass spectrometry signal.

It is speculated that the first plateau at 3.0 V is due to the oxidation of Li_2O crystallites that are deposited near or on the Ni catalyst at the cathode, whereas the higher plateau at 3.3 V (whose disappearance at the 10th charge is not well understood at present) corresponds to the oxidation of Li_2O deposited on LAGP. In the latter case, the soluble oxide must diffuse back to the Ni particles for OER, creating a kinetic overpotential as previously noted in Na-O_2 cells.[191] Moreover, rechargeability of the cell improves upon deeper cycling as indicated by more oxygen evolution and a more prolonged charge plateau at 3.0 V, with a CE of 100 % at the 10^{th} cycle (**Figure 6.5C**).

6.5 Long-term Cycling Performance of the Li-O_2 Battery

The long-term electrochemical performance of the newly designed Li-O_2 battery based on four-electron conversion was examined by galvanostatic cycling at limited discharge capacity of $0.5\,mA{\cdot}h{\cdot}cm^{-2}$ at $0.1\,mA{\cdot}cm^{-2}$ for 100 cycles (**Figure 6.6A**). Shallow cycling was necessary to limit the amount of Li transfer at the negative electrode in order to provide proof of concept of the rechargeability at the cathode. The cell exhibits a low overpotential of 0.16 V and two discharge plateaus. The first plateau at $\sim$3.0 V *vs.* Li/Li^+ corresponding to a very low capacity ($\sim 0.1\,mA{\cdot}h{\cdot}cm^{-2}$), followed by a much longer discharge plateau at $\sim$2.75 V *vs.* Li/Li^+. The Ni-$LiNO_3$-KNO_3 cathode cell at a much deeper state of discharge of $11\,mA{\cdot}h{\cdot}cm^{-2}$ exhibits a similar electrochemical profile, although the first short plateau is masked by the large discharge capacity (**Figure 6.4A**). The first discharge plateau in **Figure 6.6A** can be ascribed to the

initial formation of the Li_2O species in solution, which has a different formation energy than that of solid Li_2O. Phase field simulation of Li-O_2 electrochemistry by Welland *et al.* reports a higher potential results from nucleation of a supersaturated solution of solvated species before growth of solid products.[192] The longer plateau at 2.75 V corresponds to oxygen reduction at the surface of the Ni electrocatalyst to form Li_2O. Upon charge, the cell also exhibits two charge plateaus at ~3.0 and ~3.3 V *vs.* Li/Li^+, which is in agreement with the DEMS measurement in **Figure 6.5B** and the deep-cycled Ni-$LiNO_3$-KNO_3 cathode in **Figure 6.4A**. The CE of the cell increases rapidly from 80 to 100 % over ten cycles and is subsequently stable (**Figure 6.6B**). This performance is superior to that of aprotic organic electrolyte Li-O_2 cells,[68] where parasitic reactions cause poor cycling performance. A monolayer of carbonate created at the carbon-Li_2O_2 interface causes an increase of interfacial resistance,[193] and triggers the decomposition of organic electrolyte by a superoxide attack that forms carbon-centered radicals.[194] By using inorganic electrolytes, electrolyte degradation is avoided. Moreover, a layer of lithiated nickel (III) oxide and Ni_2O_3 on the surface of the Ni particles (because of the oxidation of Ni by $LiNO_3$, **Figure 6.3**) provides a protective passivation layer; meanwhile, lithiation improves the electronic conductivity of the oxide layer.[195] Hence, the chemically stable inorganic electrolyte and electrocatalyst play critical and synergistic roles in assuring a four-electron conversion to form Li_2O.

Although a Li^+-ion conducting interface is used between the Li and LAGP in order to prevent direct reduction of the LAGP,[196], degradation of the LAGP membrane over 100 cycles - arising from its probable poor stability in molten nitrate and some localized reduction (**Figure 6.7A**) - still leads to increased impedance from the membrane

(**Figure 6.7B**). This resulted in an increase of the overpotential by 0.15 V over 100 cycles. This suggests more effort is needed to address the challenges on the negative electrode side, such as the development of lithium protection layer.

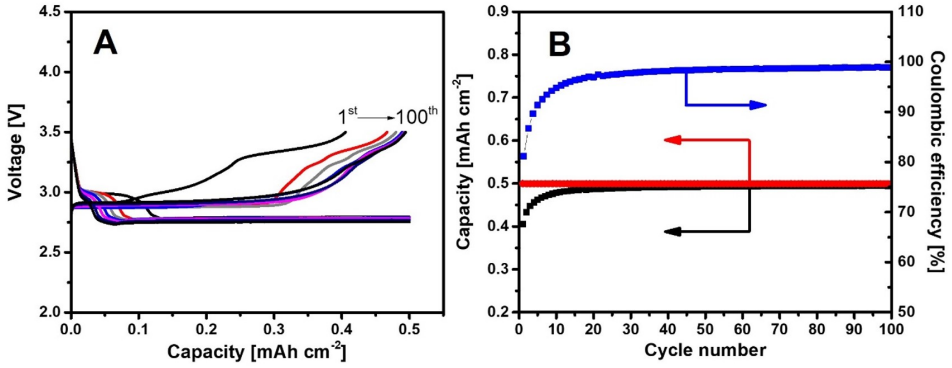

Figure 6.6. Long-term cycling performance of the inorganic Li-O_2battery. (A) Electrochemical profiles of the molten salt Li-O_2 cell fabricated with the Ni-$LiNO_3$-KNO_3 composite cathode operating at 150 °C over 100 cycles at a constant current density of 0.1 mA·cm^{-2}. (B) The corresponding changes in discharge (red), charge (black), and CE (blue) during cycling. The discharge capacity was limited at 0.5 mA·h·cm^{-2}. The upper voltage limit was set at 3.5 V due to O_2 evolution stops at a charge voltage of 3.48 V (**Figure 6.5B**).

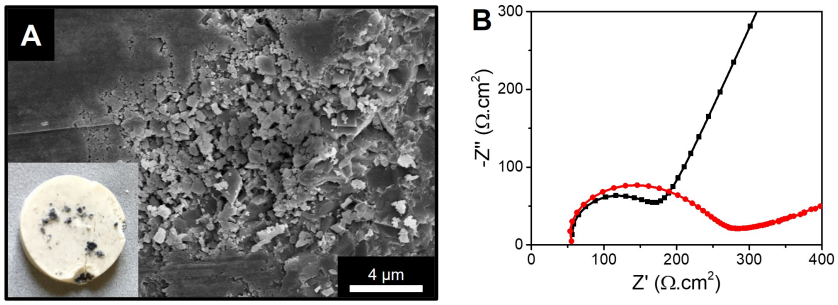

Figure 6.7. Challenges related to the LAGP electrolyte layer. (A) SEM image of LAGP membrane after cycling, where the black spots and cracks on the surface of the membrane are shown in the photographic image (inset). (B) EIS spectra LAGP at 150 °C before (black) and after (red) cycling for 50 cycles.

6.6 Mechanism in the Four-Electron Transfer Process

Based on the analysis discussed above, a peroxide-mediated ORR pathway is proposed with illustration (**Figure 6.8A**) and explanation outlined below.

Diffusion. Oxygen first adsorbs on the surface of the cathode (**Equation 6.11**):

$$O_2 \rightarrow O_{2,\text{eltd}} \tag{6.11}$$

Reduction. Oxygen is electrochemically reduced to form lithium peroxide ($Li_2O_{2,\text{eltd}}$), via a two-electron transfer, on the surface of the Li_xNiO_2/Ni catalyst (**Equation 6.12**):

$$2Li^+ + O_{2,\text{eltd}} + 2e^- \rightarrow Li_2O_{2,\text{eltd}} \tag{6.12}$$

Desorption. A small amount of Li_2O_2 attached on the cathode slowly desorbs from the catalyst surface, governed by its low solubility and diffusibility in the molten nitrate electrolyte (**Equation 6.13**):

$$Li_2O_{2,\text{eltd}} \rightarrow Li_2O_{2,\text{elyt}} \tag{6.13}$$

Disproportionation. Most remaining Li_2O_2 is converted to Li_2O by the catalyst through disproportionation (**Equation 6.14**):

$$Li_2O_{2,\text{eltd}} \rightleftharpoons Li_2O_{,\text{eltd}} + \frac{1}{2}O_2 \tag{6.14}$$

Transport. Once formed, Li_2O is soluble in the electrolyte (**Equation 6.15**). Upon supersaturation, formation of Li_2O nuclei triggers nucleation and growth which results in micrometer-sized Li_2O crystals:[197]

$$Li_2O_{,\text{eltd}} \rightarrow Li_2O_{,\text{elyt}} \qquad 6.15$$

Experimental and computational studies suggest that the ORR pathway via peroxide is operative over a variety of metal catalysts (such as platinum, mercury, and silver).[198, 199]. The amount of Li_2O_2 formed at different discharge conditions is quantified after discharging the cell to $2\,mA{\cdot}h{\cdot}cm^{-2}$. As shown in **Figure 6.8B** and **6.8C**, the amount of Li_2O_2 increases from 0 µmol at $0.05\,mA{\cdot}cm^{-2}$ to 4 µmol at $0.2\,mA{\cdot}cm^{-2}$, whereas it decreases from 3.5 µmol at 135 °C to 0 µmol at 170 °C. According to the proposed ORR pathway, the fast formation of Li_2O_2 at higher discharge rates likely results in some Li_2O_2 remaining owing to relatively slow disproportionation (rate-determining step). However, the elevated temperature accelerates disproportionation, rapidly converting Li_2O_2 to Li_2O. Evidence confirming the catalytic disproportionation of Li_2O_2 is shown in **Figures 6.8D** and **6.8E**. When a mixture composed of commercial Li_2O_2 powder and the Ni-$LiNO_3$-KNO_3 material was heated at 150 °C, oxygen evolution was detected with mass spectrometry, accompanied by diffraction peaks of Li_2O in the XRD pattern of the mixture. Neither feature is observed in the absence of either component.

Suntivich *et al.* have shown that high ORR activity for transition metal oxide catalysts primarily correlates to σ^*-orbital (e_g) occupation and the extent of transition-metal-oxygen covalency.[200] Optimal activity correlates to an e_g occupancy is close to unity.

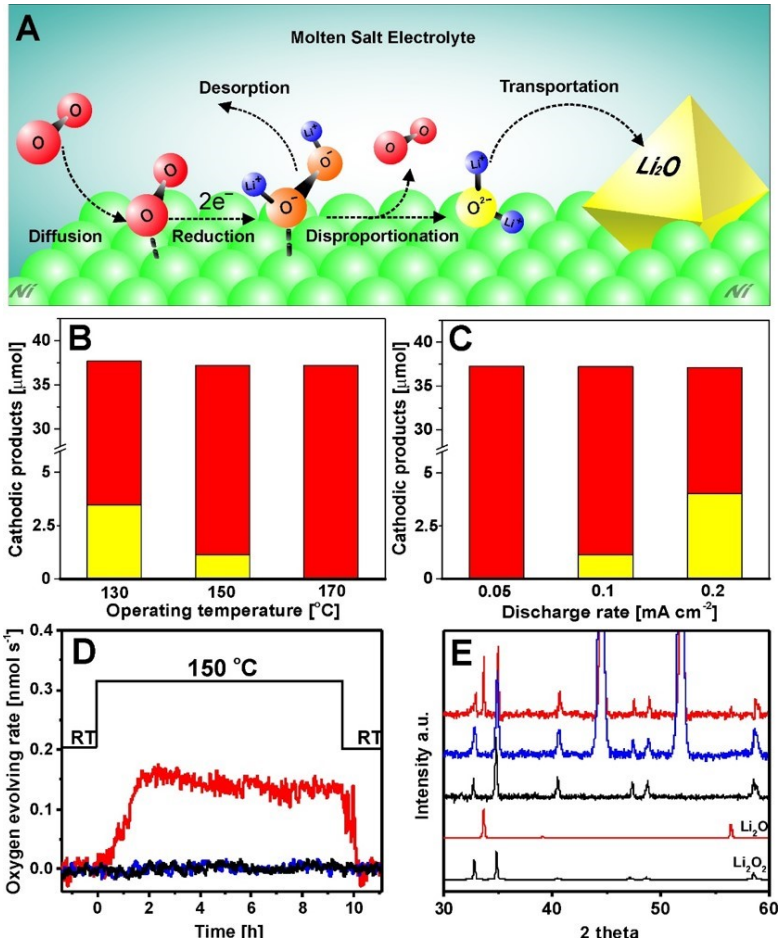

Figure 6.8. Mechanistic studies of the oxygen reduction reaction over the Ni-based electrocatalyst. (A) Schematic illustration of the pathway of the oxygen reduction reaction. (B and C) Effects of (B) operating temperature and (C) discharge rates on the composition of oxygen reduction products, Li_2O (red) and Li_2O_2 (yellow). A discharge rate of $0.1\,mA{\cdot}cm^{-2}$ was applied to study the temperature effects, and 150 °C was chosen to investigate the effects of discharge rate. All cells were discharged to $2\,mA{\cdot}h{\cdot}cm^{-2}$ prior to quantitative analysis. (D) Oxygen mass spectrometry signal response on heating a mixture composed of commercial Li_2O_2 powder with the Ni-$LiNO_3$-KNO_3 composite cathode (red), Ni (blue), and $LiNO_3$-KNO_3 molten nitrate (black) at 150 °C, respectively; and (E) their corresponding XRD patterns after heating the mixtures for 1 week.

Consistent with this design principle, the surface Li_xNiO_2 species on the Ni particle contains Ni^{3+} with an electron configuration of $t_{2g}^6 e_g^1$.[201] Furthermore, the Ni^{3+}/Ni^{2+} redox couple promotes charge transfer between surface cations and adsorbates. Both factors give rise to a high ORR activity of Li_xNiO_2.[202] Although the thermodynamic driving force for the disproportionation of Li_2O_2 is very small (only $-0.063\,kJ{\cdot}mol^{-1}$ at 150 °C), the removal of Li_2O from the catalyst surface via solution-mediated transport will shift the equilibrium (**Equation 6.15**) toward the right, exposing the active catalyst surface. The spontaneous disproportionation reaction on oxygen reduction dictates that OER must follow a different pathway, however. Indeed, no Li_2O_2 intermediate is observed when charging a Li-O_2 cell by using a Li_2O-prefilled cathode (**Figure 6.9**). The lack of a peak at 408 nm suggests Li_2O_2 is not formed on charging, but rather Li_2O is directly oxidized to molecular oxygen (O_2). It is speculated that Li_2O is solubilized and diffuses to the surface of Li_xNiO_2 for electrocatalytic oxidation via a direct 4 e^- pathway. Suntivich *et al.* also concluded that the OER activity of metal oxides, similar to ORR, is dependent on the occupancy of 3d electron states with e_g symmetry.[203] Thus, although Li_xNiO_2 is an effective ORR electrocatalyst, it also reversibly catalyzes OER,[204] leading to a low charge overpotential.

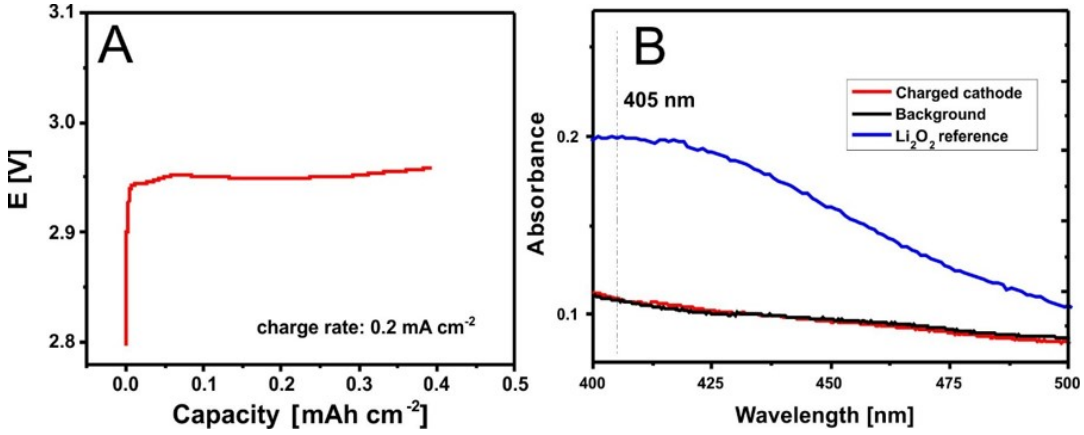

Figure 6.9. Analysis Li_2O_2 as redox intermediate during charge using Li_2 pre-filled cathode. (A) Charge profile of a Li-O_2 cell with a Ni-$LiNO_3$-KNO_3 pre-filled with commercial Li_2O powder. The charge cut-off was set at a capacity of $0.4\,mA{\cdot}h{\cdot}cm^{-2}$ at a current density of $0.2\,mA{\cdot}cm^{-2}$. (B) UV-vis spectra of the corresponding charged cathode indicates the absence of Li_2O_2.

6.7 Conclusion

By tuning the operating temperature and using a single bifunctional ORR/OER catalyst, the Li-O_2 battery overcomes the barriers of thermodynamics and kinetics, leading to the electrochemically reversible formation of Li_2O instead of Li_2O_2. The in-situ generated Li_xNiO_2 electrocatalyst - applicable to other metal oxygen electrochemistries - catalzes both O-O cleavage to form Li_2O on discharge, and the reverse process that releases oxygen upon charge in a $4e^-/O_2$ process with excellent CE and low polarization. The latter is aided by electrolyte-solubilized Li_2O transfer. Of course, Li-O_2 cell is more reversible when Li_2O is the product is a consequence of the less reactive chemical nature of oxide versus superoxide or peroxide. Moreover, the use of chemically stable

inorganic electrolytes and a non-carbonaceous cathode circumvents the degradation of organic electrolyte and carbon corrosion, which form the main failure mechanisms for the traditional aprotic Li-O_2 cells. The Li_2O cell presented here is akin to both fuel cells and electrolyzers - which also operate on the basis of a 4 e^- electrocatalyzed reaction - in which Li_2O replaces H_2O, and the combination forms a simple reversible energy storage system. Though elevated operating temperatures can limit battery applications, commercialized sodium nickel chloride cells and Na-S batteries actually run at much higher temperatures ($\sim$325 °C), and proton exchange membrane fuel cells are recently trending to operate at temperatures between 120 and 180 °C.[205] More fundamentally, this work directly addresses a number of issues associated with Li-O_2 chemistry, showing it is not intrinsically limited and that a reversible four-electron transfer from Li_2O is possible. All these factors enable the Li-O_2 cells to operate at almost theoretical CE.

Chapter 7

Solution Route to Synthesize LiPON Protective Layer for Lithium Metal Anode

7.1 Introduction

Lithium metal has long sought as the *Holy Grail* negative electrode for Li batteries due to its high theoretical capacity ($3800\,\mathrm{mA{\cdot}h{\cdot}g^{-1}}$ or $2080\,\mathrm{mA{\cdot}h{\cdot}cm^{-3}}$) and low reduction potential ($-3.04\,\mathrm{V}$ *vs.* SHE). However, as discussed in **Section 1.5**, lithium's characteristic dendrites electrodeposition poses tremendous challenges in its application as the anode. This problem is further amplified in some of the high specific energy electrochemical systems such as Li-S and Li-O_2 batteries because of the large amount of uneven Li deposition during charge. While there has been great efforts in resolving this problem, the issues related to severe shuttling effects, fast cell degradation due to electrolyte degradation/consumption, and cell short-circuits are yet to be resolved.[94, 107]

As dendrite formation is triggered by the large electric field caused by ion depletion

near the electrodeposition surface, which is governed by the intrinsic transference number of the electrolyte, stabilizing lithium deposition by controlling the ion depletion and/or improving the surface stability are routes to resolve that issue.[90] This is exemplified by some of the recent works that utilize conductive porous skeletons as current collectors to suppress dendrite formation by reducing the local current density.[107, 206] This approach is efficient because the plated lithium duplicates the porous structure. Another approach focuses on electrolyte design such as solid-state electrolyte or solvent-in-salt systems that posse unity or near-unity lithium transference number compared to classical electrolytes.[110, 207, 208] The goal of this approach is to alleviate ion depletion on the anode's surface. Artificial installation of a stable SEI by electrolyte additives[121, 49, 209] or ex-situ physical deposition by protective layer too can limit the accelerated parasitic reactions between lithium anode and electrolyte.[210, 211, 212] Although these two approaches are effective at relatively low current densities, their combination is more promising to tackle the dendrite challenges and the severe shuttling effect, as recently demonstrated by the effectiveness of surface protection layers equipped with good ion conductivity and high chemical stability. These materials include alloy-halide composites,[213, 214], Li_3PS_4,[121], Li_3N,[215] and Li_3PO_4.[216]

In addition to the class of material is lithium phosphorus oxynitride - an ionic conductive and chemically stable glass electrolyte that stabilizes lithium metal during deposition.[217] While the material itself is not a very good ion conductor, exhibiting conductivity on the order of 1×10^{-6} - 1×10^{-7} S·cm^{-1}, the interface that is formed with lithium is excellent. The excellent stability of this material with respect to Li is likely ascribed to characteristic of oxynitrides, though the understanding of why this is

the case is still not clear.[218, 219, 220] Nonetheless, LiPON films are widely used in micro-batteries, where the material is conventionally coated onto electrodes via atomic layer deposition (ALD) methods.[221] Deposition of LiPON films from Li_3PO_4 targets under a nitrogen atmosphere, however, involves numerous complex factors which have to be strictly controlled.[222, 223, 224] In this chapter, I present a wet chemistry route that involves the formation of elemental phosphorous via reduction of a phosphorous halide, followed by its nitridation in $LiNO_3$ to synthesize LiPON in situ on lithium metal.

7.2 Experimental Methods

7.2.1 Preparation of LiPON-Protected Lithium Anode

Lithium metal foil (99.9 %, Sigam-Aldrich) was polished to remove any impurity. After polishing metal until the surface was extremely shiny, the foil was immersed in a THF solution containing 0.167 M PCl_3 (99.999 %, Sigma-Aldrich). After a phosphorus layer was form on the lithium metal surface, the film was transferred to $LiNO_3$ solution (0.5 M, THF). Once nitridation was completed (24 h), the LiPON protected lithium metal (LiPON/Li) was rinsed thrice with THF and dried in vacuum for 12 h.

7.2.2 Preparation of the Core-Shell Sulfur-MnO_2 Nanoparticle

A core-shell composite was utilized as the sulfur active material, and was synthesized as previously reported.[225] In a typical procedure, 17.87 g sodium thiosulfate pentahydrate (ACS, Sigma-Aldrich) dissolved in 400 mL water was added to an aqueous

polyvinylpyrrolidone solution (33.35 g·L^{-1}, 40kDa, VWR). After stirring the entire mixture for 15 min, 13 mL HCl (37 wt. %, Sigma-Aldrich) was pour into the slightly turbid polyvinylpyrrolidone/thiosulfate solution. After stirring for 2 h, the sulfur nanoparticles were rinsed with copious amount of water before redispersing in water. To coat the δ-MnO_2 onto the sulfur core, 16 mL of the as-prepared sulfur nanoparticles (5 wt. % in water) were further dispersed in 800 mL water and sonicated for 2h in an ice bath. Next, 200 mL $KMnO_4$ (2 mg·mL^{-1}) was added dropwise to the nanosized sulfur suspension. The mixture was stirred for 24 h at room temperature. The solid was then collected by centrifugation (10 kRPM, 5 min) and dried at 90 °C for 12 h. The sulfur content in the S-MnO_2 composite was determined to be 75 wt. % by TGA.

7.2.3 Electrode Preparation

The sulfur electrodes were prepared by casting a water/DMF slurry containing S-MnO_2, Super P, CNT, and poly(AETMAC-*co*-EGDA) in weight ratio of 8:0.5:0.5:1 onto P50 carbon paper. The electrodes were dried in a 60 °C oven for 24 h before they were transferred to an Ar filled glovebox. Li-S coin cells (2023) were assembled using lithium foil as anode/reference electrode. The electrolyte formulation for Li-S cell was 1 M LiTFSI in DOL/DME, the electrolyte/sulfur ratio was maintained at 7:1 in all electrochemical studies.

7.3 Physical Characterization of the LiPON Protection Layer

A facile wet chemistry route is presented to coat LiPON on lithium metal in situ, using PCl_3 as the phosphorus source and $LiNO_3$ as the nitridation agent. The SEM shows the LiPON film is uniformly coated onto Li. The average thickness of the film is $\sim$10 µm (**Figure 7.1**). Elemental mapping on the film further reveals an even distribution of N, O, and P elements, with an average nitrogen content of 12 at. % (**Figures 7.1C** to **7.1G**). This suggests a high degree of nitridation in the LiPON phase.

The reaction between lithium metal and phosphorus trichloride affords an red phosphorus layer on the lithium metal surface (**Equation 7.1**), evidenced by its corresponding Raman bands at 287, 352, 386, 453 cm^{-1} (bottom panel, **Figure 7.2A**) that match the fingerprints of red phosphorus.[226, 227] The spontaneous transformation of the phosphorus material to LiPON in the presence of $LiNO_3$ is confirmed by additional new bands that are characteristics to the LiPON structure (top panel, **Figure 7.2A**). The board bands at 820 cm^{-1} is assigned to $-$N= linkage, whereas two additional bands at 601 and 650 cm^{-1} are clear indications of the tri-coordinated nitrogen ($-$N<) bonding structure.[228, 229] Moreover, new emerging bands at 1000 and 1117 cm^{-1} belong to the pyrophosphate/metaphosphate moieties commonly identified in the LiPON structure.[229, 230] In summary, the nitridation of red phosphorus results in the formation of LiPON film. Although the reaction mechanism of using lithium nitrate to convert red phosphorus to LiPON is not fully understood, a possible reaction is proposed in **Equation 7.2**.

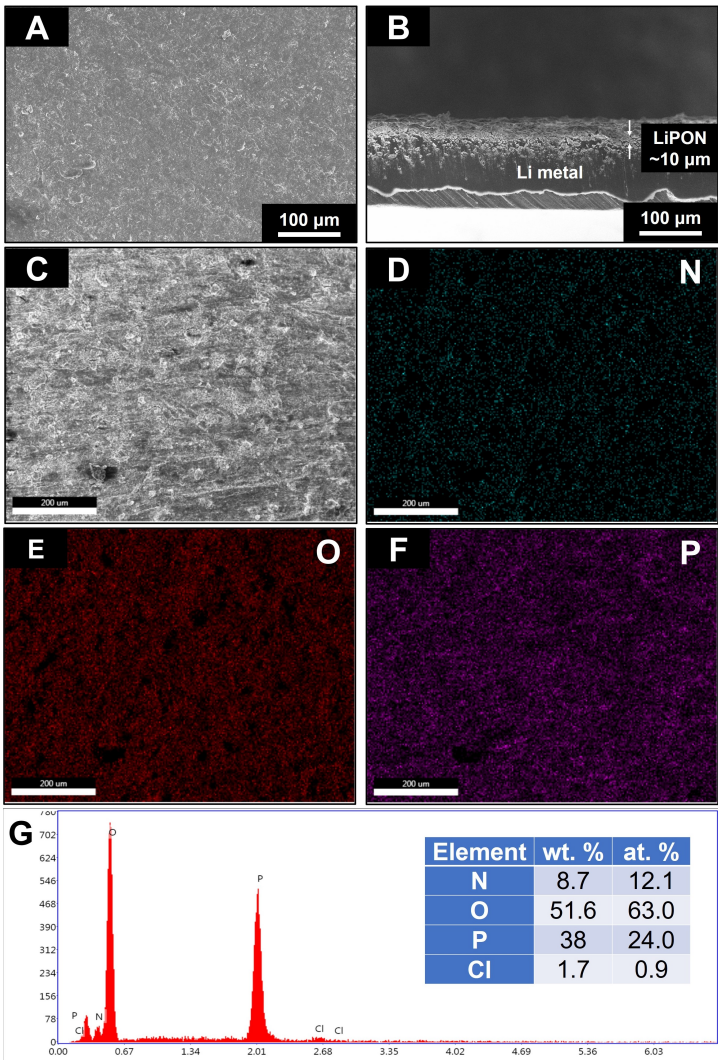

Figure 7.1. SEM and EDX analysis of the LiPON protected Li metal. (A) SEM images of LiPON/Li: (A) topological and (B) cross-sectional view. (C-G) EDX analysis on the same material. (C) SEM image of the area; (D-F) EDX mapping shows a uniform distribution of (D) N, (E) O, and (F) P on the surface. (G) EDX point spectrum shows the existence of C (unlabelled), O, N, P and Cl (residual LiCl from the phosphorylation reaction) on the surface. The nitrogen content is ∼12 at. % based on the EDX point spectra averaged over several locations.

$$3Li + PCl_3 \rightarrow 3LiCl + P \quad (7.1)$$

$$Li + P + LiNO_3 \rightarrow Li_xPO_yN_z \quad (7.2)$$

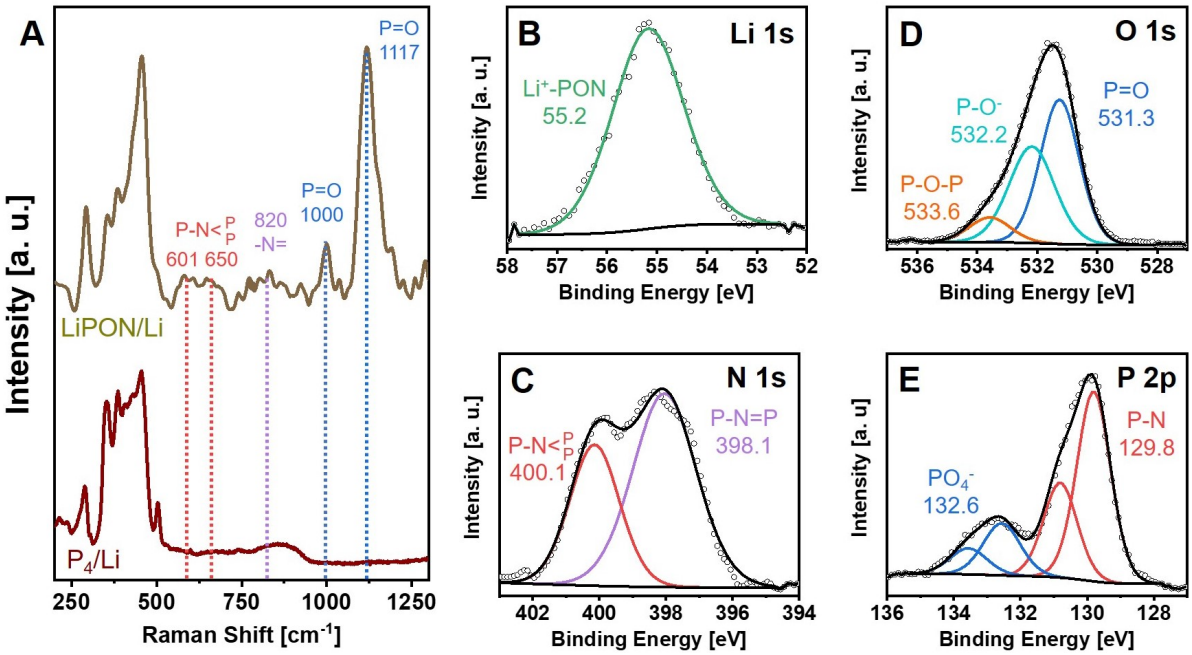

Figure 7.2. Characteristics of the LiPON protection layer. (A) Raman analysis of the material coated onto Li after phosphorylation (bottom) and its nitridation (top). (B-E) XPS analysis of the LiPON protected lithium foil: (B) Li 1s; (C) N 1s; (D) O 1s; and (E) P 2p.

It is worth noting that the intensities of the nitrogen-related bands in **Figure 7.2A** are fairly weak, probably due to the intrinsic structural disorder in LiPON.[222, 228] XPS analysis is employed to further probe the surface species of the LiPON-protected Li metal. As per convention, only the peak positions of the lower binding energy components of the P 2p spin orbital doublets are discussed. The single peak in Li 1s spec-

trum at 55.6 eV is assigned to the Li^+ that binds to the pyrophosphate/metaphosphate anions (**Figure 7.2B**).[222, 231] The two chemical environments fitted in the N 1s spectrum (**Figure 7.2C**) is also consistent with the Raman data (**Figure 7.2A**). The first peak, located at 398.1 eV and contributing 67 % of the nitrogen environment, corresponds to nitrogen bounded to two phosphorus atoms (−N=). The second peak, located at 400.1 eV, is characteristic of a nitrogen atom linked to three phosphorus atoms (−N<) found in LiPON. The O 1s spectrum in **Figure 7.2D** is also deconvoluted into three Gaussian-Lorentzian components, which correspond to the P=O (non-bridging, 531.3 eV), $P-O^-$ (non-bridging, 532.2 eV), and P−O−P (bridging, 533.6 eV) bonding structures. Here, the relatively low concentration of the bridging P−O−P environments (7.74 %) and the predominance of P=O sites (51.2 %) suggests high nitridation in the LiPON material.[231] This is further supported by the P 2p spectrum shown in **Figure 7.2E**. The di-coordinated nitrogen (−N=), or tri-coordinated nitrogen (−N<) atoms substitutes oxygen atoms in the PO_4^- groups, giving rise to an amorphous glass formed by two additional building units (tetrahedral PO_3N and PO_2N_2) with a binding energy at 129.8 eV.[222, 223] This substitution also reduces the binding energy that would correspond to PO_4^- environment from the typical value of 133.2 to 132.6 eV.[222, 232] It worth noting though that the peak corresponding to red phosphorus overlaps with that of the PN environment due to their similar binding energies (130.0 *vs.* 129.8 eV). In conclusion, the chemical environments identified in Raman and XPS (**Figure 7.2**) are consistent with each other. LiPON is considered to be a non-stoichiometric lithium oxynitride phosphate glass where the P/O and P/N ratios can be varied within a wide range. The proposed LiPON structure is presented

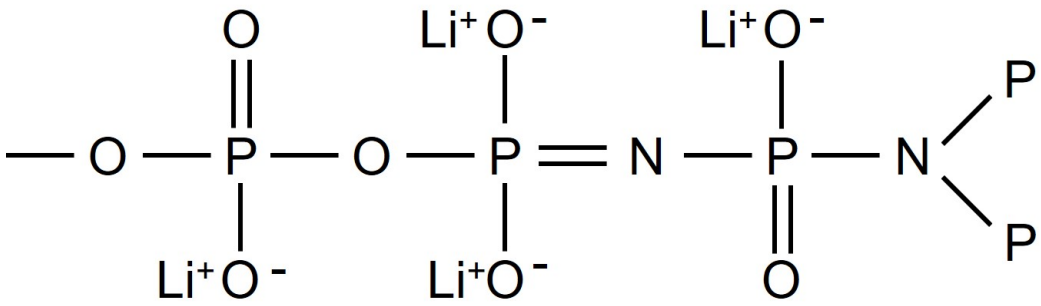

Figure 7.3. Proposed LiPON structure.

in **Figure 7.3**, and is consistent with the LiPON film produced by conventional ALD methods. Furthermore, the composition of this protection layer is distinct from SEI produced from lithium metal treating with $LiNO_3$ alone (particularly the nitrogen chemical environments), where the product is mostly comprised of Li_xNO_y and $ROCH_2-Li$ moitiés.[116, 233]

The Li-ion conductivity of the LiPON film was evaluated by EIS. A Swagelok cell was prepared by stacking a piece of lithium metal and the LiPON protected lithium together, without liquid electrolyte and separator (**Figure 7.4A**). The total ionic conductivity measured from the Nyquist plot is 6.2×10^{-7} S·cm^{-1} (**Figure 7.4B**), comparable to the LiPON films prepared by ALD which ranges from 1×10^{-7} to 1×10^{-6} S·cm^{-1}.[93, 221, 222, 223, 224, 231]

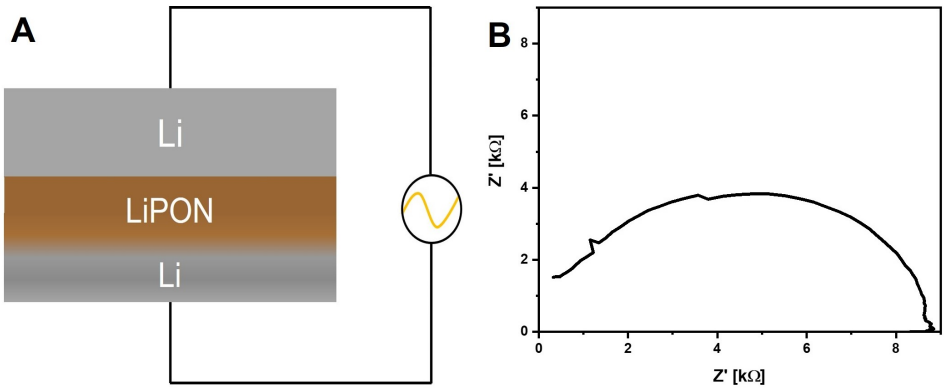

Figure 7.4. Electrochemical measurement of LiPON protected Li in solid-state configuration. (A) Schematic of the all-solid-state cell prepared by stacking LiPON-protected Li and Li foil and (B) the Nyquit plot of the cell. (C) The evolution of voltage profiles of the symmetric cells over cycling with the pristine Li (gray) and the LiPON protected Li (re). The electrolyte is 1 MLiTFSI in DOL/DME.

Li dendrite suppression by the LiPON protective film is further supported by the long-term electrochemical profile of the stripping-plating measurements. Experiments were carried out using coin-cell configuration with 1 M LiTFSI in DOL/DME as liquid electrolyte and Celgard separator. A fixed amount of 1 mA·h·cm^{-2} of lithium was deposited alternatively between the working and counter electrodes at a current density of 0.5 mA·cm^{-2}. The LiPON protected lithium foil shows stable Li plating/stripping up

to 1500 hours (750 cycles) in the ether electrolytes (**Figure 7.5A**). In sharp contrast, the cell with the pristine lithium foil short-circuited shorted at around 1200 hours when cycled under the identical conditions. In consideration of the low ionic conductivity of the LiPON layer ($6.2 \times 10^{-7}\,\mathrm{S{\cdot}cm^{-1}}$, **Figure 7.4B**), the theoretical overpoential due the Ohmic drop across layer should be significantly higher than $\sim$40 mV. However, the porous structure of the LiPON film (**Figure 7.1B**) enables the liquid electrolyte to directly contact with the Li metal. This in turns lowers the overpotential to a value that is similar to that of the pristine Li as seen in **Figure 7.5A** in prolonged cycling ($>$ 300 hours).

The effect of the porous LiPON structure in protecting the lithium metal against liquid electrolyte is further showcased in symmetric Li|Li cells. **Figures 7.5B** and **7.5C** show the impedance spectra of these symmetric cells at OCV. There are two overlapped semi-circles for both cells. The first one at the high-frequency is ascribed to the bulk SEI resistance (R_{SEI}) and the second at intermediate-frequency is attributed to the charge transfer resistance (R_{ct}). R_{SEI} describes to the resistance of the SEI layers that forms between the lithium metal and liquid electrolyte, and is related to the interfacial stability of the lithium metal. Immediately after cell assembly, the cell with unprotected lithium metal shows an areal specific resistance of $700\,\Omega{\cdot}\mathrm{cm}^2$ which is much higher than that of the LiPON protected lithium ($200\,\Omega{\cdot}\mathrm{cm}^2$). Because LiPON remains fairly porous, the liquid electrolyte can still react with lithium metal reacts readily to form an additional SEI continues to grow over time, resulting in progressive increase of the resistance in both cell (**Figures 7.5B** and **7.5C**). However, because majority of the Li surface is covered by the LiPON material, the probability of Li metal adversely reacting with

electrolyte species to form a mechanically and chemically unstable SEI is suppressed. Therefore, the total ASR of the LiPON protected lithium metal remained significantly smaller ($500\,\Omega{\cdot}cm^2$) than the pristine lithium after 10 h of storage. (**Figure 7.5C**). This implies LiPON still manages to keep Li from reacting with the liquid electrolyte, and the layer forms a chemically stable interface with both components.

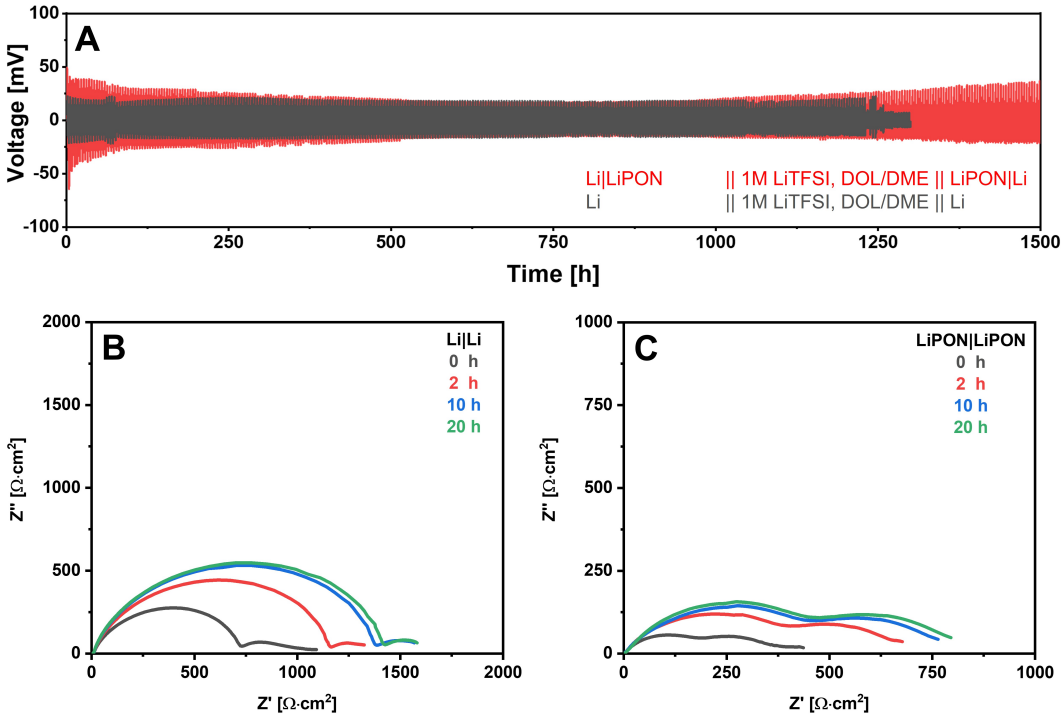

Figure 7.5. Electrochemical performance comparison between LiPON-protected and pristine Li in symmetrical cell configuration. (A) The evolution of symmetric cell voltage profiles upon Li plating on LiPON-protected Li (red) and pristine Li (grey) in liquid cell. The plating/stripping experiments were carried at a current density of $0.5\,mA{\cdot}cm^{-2}$ with a capacity limit of $1\,mA{\cdot}h{\cdot}cm^{-2}$. (B-D) Nyquist plots obtained from the EIS measurement on the symmetric cells with (B) fresh Li and (C) LiPON-protected Li electrodes, respectively. The liquid electrolyte is 1 M LiTFSI in DOL/DME.

7.4 Electrochemistry of LiPON protected Li-S Cell

One of the largest hurdles in lithium anode, aside from the dendritic growth of lithium during deposition, is the parasitic polysulfide shuttle. While there have been much efforts to minimize the shuttling effect, such as sulfur host materials that suppress polysulfide leeching into the electrolyte by operation of physical/chemical adsorption.[9] However, long term cycling of these lithium sulfur batteries are largely achieved with the aid of $LiNO_3$ electrolyte additive that consumes some of the leached polysulfides and forms a stable SEI on lithium metal.[30, 114, 118] Therefore, the effectiveness of the LiPON film in protecting Li metal in Li-S batteries needs to be evaluated in electrolyte that does not contain such additives (1 M LiTFSI in DOL/DME).

The active material composite is the MnO_2 encapsulated sulfur nanoparticles that had been reported previously.[225] The sulfur core were synthesized via the disproportionation of $Na_2S_2O_3$ in the presence of hydrochloric acid, utilizing polyvinylpyrrolidone as template. The SEM image (**Figure 7.6A**) of the sulfur nanoparticles reveals an uniform spherical morphology with an average diameter of 500 nm. Upon reaction with potassium permanganate, the surface sulfur nanoparticles was converted to MnO_2.[225] This results in the formation of a sulfur-MnO_2 core-shell structure as shown in **Figure 7.6B**. The existance of the MnO_2 nanosheet is further evidenced by the classical birnessite-type δ-MnO_2 nanoleaflets surrounding the underlying sulfur nanoparticles as shown in its high-magnification SEM image (**Figure 7.6C**). TGA in **Figure 7.6D** confirms the sulfur loading in the composite to be 75 wt. %.

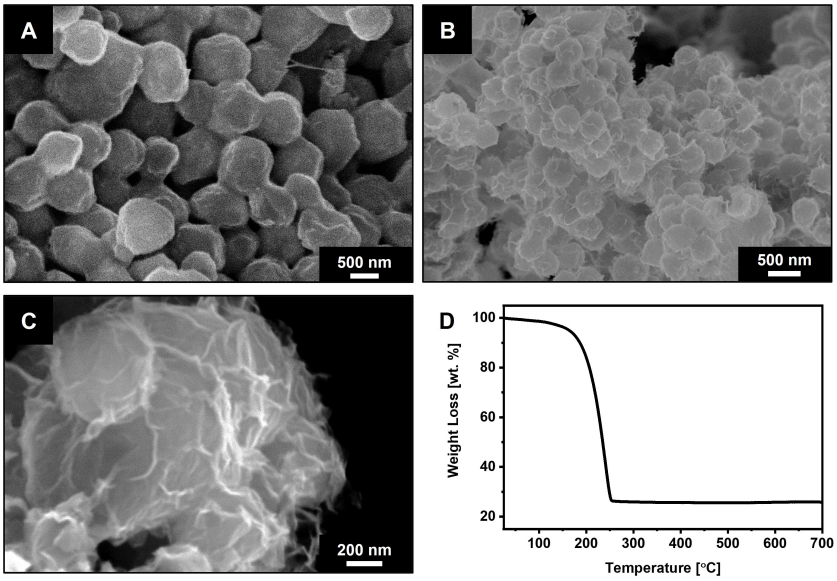

Figure 7.6. Physical characterization of the S-MnO_2 core-shell composite. (A-C) SEM images of (A) sulfur nanoparticles; and (B) low- and (C) high-magnification of core-shell sulfur-MnO_2 cathode composite. (D) TGA curve for the same material, yielding a sulfur content of 75 wt. % at a ramp rate of 10 °C·min^{-1} under N_2 flow.

The electrochemical performance of the resulting Li-S cell was examined by galvanostatic cycling (**Figure 7.7A**). The sulfur loading in these cells were maintained at ∼3 mg·cm^{-2}. Poly(AETMAC-*co*-EGDA) was employed as the binder at the cathode to accommodate large volume change during cycling. During the first activation cycle at C/20, the bare Li and LiPON-protected Li cells deliver a similar discharge capacity of 1050 mA·h·g^{-1}. However, the severe polysulfide shuttle results an infinite charge on the cell employing bare Li as the anode. In sharp contrast, the cell with LiPON protected lithium as anode recovered all of its capacity on charge. Upon long-term cycling (**Figure 7.7B**) at C/5, however, the CE of the LiPON cell quick falls to around 83 % percent. The relatively low CE suggests polysulfide shuttle is not entirely eliminated by

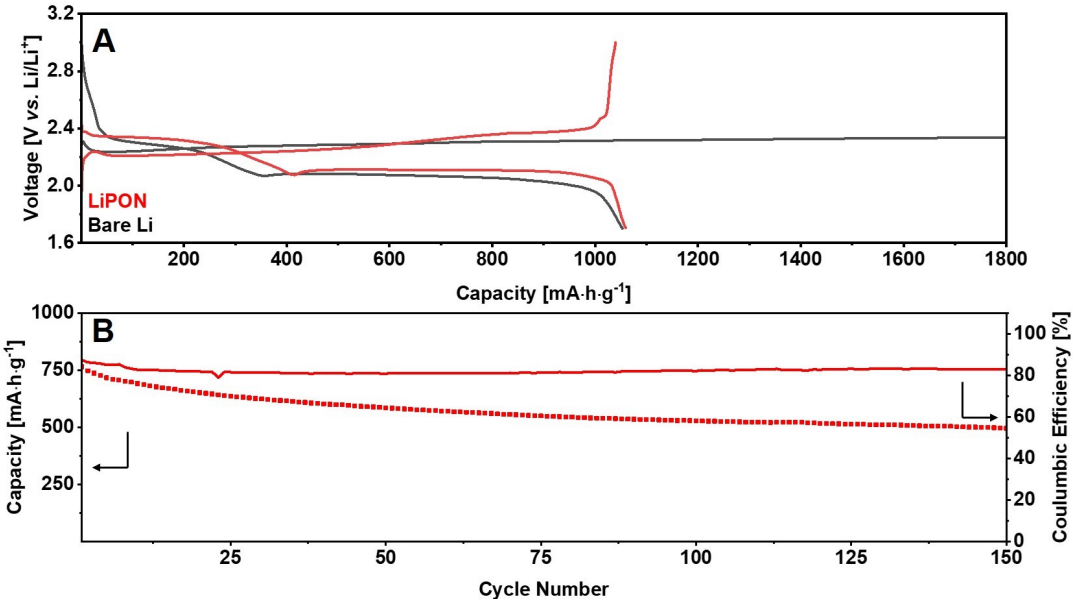

Figure 7.7. Electrochemical performance of the LiPON protected Li. (A) Electrochemical profiles (C/20) and (B) long-term cycling stability the Li-S cells fabricated with LiPON-protected lithium anode at C/5 rate. Electrolyte formulation was 1 M LiTFSI in DOL/DME.

the LiPON film. Careful SEM analysis on **Figure 7.1A** and **7.1B** shows LiPON film is not dense. That would mean that the dissolved polysulfide can creep into the pores and corrode the lithium anode, giving rise to the low CE. This is further supported by the negligible overpotential difference between the two cells (**Figure 7.7A**). In other words, optimization of the film is still necessary to construct a dense film.

7.5 Conclusion

I have demonstrated a solution chemistry route for synthesizing LiPON as protection layer for Li metal, as proven by extensive Raman and XPS analysis. Although the

reaction mechanism is yet to be understood, this method is nonetheless very distinct from the traditional ALD method, highlighting its effectiveness and low cost. Utilizing S-MnO_2 core-shell composite as active materials, the LiPON protected cell is able to achieve at least 80 % CE without the aid of lithium nitrate, whereas the bare Li cell experienced infinite charge due to polysulfide shuttle.

Chapter 8

Conclusions and Future Prospects

8.1 Conclusion

This dissertation document encompasses a wide spectrum of approaches, from the aspect of electrode and electrolyte design, to improve capacity retention and cycle life of Li-S and Li-O_2 batteries, as well as the verification and elucidation on the underlying chemistry that drive their successes. Due to their high energy density (**Table 1.1**) and cost effectiveness, Li-S and Li-O_2 batteries are considered as two strongest candidates as post lithium-ion battery technologies. However, to fully realize their potentials, their respective challenges need to be addressed.

For Li-S battery, the longevity of sulfur cathode is hampered by both the polysulfide shuttle and cathode architecture stability. An ideal sulfur host should be lightweight, electrically conductive, and exhibit strong chemical interactions with lithium polysulfides. The comprehensive study in **Chapter 3** focuses on uncovering a corre-

lation between the metal oxides' redox potentials and their abilities to mediate sulfur conversion via the formation of thiosulfate/polythionate complex. Extensive CV and XPS studies on various transitional metal oxides conclude the key in activating thiosulfate/polythionate conversion lies within the redox potential overlapping with the host materials and polysulfides. This *Goldilock* potential sits between 2.40 and 3.05 V *vs.* Li/Li^+, and materials such as CuO (E° = 2.53 V), VO_2 (E° = 2.79 V), MnO_2 (E° = 3.05 V) have been identified to fit this category. Materials outside of this range lead to either over-oxidation of the sulfur species to electrochemically inactive sulfate and small traces of thiosulfate/polythionate (> 3.05 V: NiOOH and V_2O_5), or entrapment of polysulfides via other mechanism such as electrostatic interactions (< 2.40 V: Fe_2O_3, Co_3O_4, V_2O_3, NiO, CuO_2, and CoO). To further validate this concept, several home-made transition metal oxides supported on graphene (i.e. Co_3O_4, VO_2, and V_2O_5) were prepared and utilized as sulfur hosts. Unsurprisingly, the Li-S cells fabricated with VO_2-graphene show the most promising results, owing to the formation of thiosulfate/polythionate redox mediators. The cells exhibit an excellent initial discharge capacity of 1180 $mA{\cdot}h{\cdot}g^{-1}$ at C/20, and maintain an ultra-low capacity fading rate of 0.058 % per cycle over 1000 cycles. The significance of this study is that now the Li-S community has a guideline for determining whether a particular sulfur host material follows the thiosulfate/polythionate mediation mechanism.

Chapter 4 provides a perfect example of host material that extends the scope of sulfur catenation mechanism, using highly electronic conductive 2D transition-metal carbides or carbonitrides known as MXene as a model system. While the polysulfide entrapment mechanism of this material was partially revealed in a previous report, this

work provides a full picture on how MXene entraps polysulfides through a two-step dual-mechanism. The general formula for MXene can be presented as $M_{n+1}X_nT_x$ where T is the surface-terminated functional groups (OH, F, O, etc.). XPS analysis on the MXene-Li_2S_4 composite shows the terminal hydroxyl groups on the MXene's surface engage in the thiosulfate/polythionate mechanism, exposing the underlying acidic Ti sites to undergo a secondary Lewis acid-base interactions with polysulfides. Multiwalled carbon nanotubes are further incorporated between MXene nanosheet to improve the electronic conductivity, maximize the polysulfide adsorptivity, and prevent individual MXene nanosheeet from re-stacking. This porous, conductive network enables the resultant Li-S cell to exhibit excellent long-term cycling performance with an ultra low fading rate of 0.043 % per cycle for up to 1200 cycles. Moreover, stable performance is achieved for practical high sulfur loading electrodes up to 5.5 $mg{\cdot}cm^{-2}$. **Chapter 3** and **4** inspire future studies to seek other materials that have both high electrical conductivity and polysulfide adsorption, evidenced by some of the recent publications.[234, 235, 236]

The state of health for sulfur cathodes is not only determined by host materials to encase active materials and retain polysulfides, but also by binder materials to maintain structural stability. Polymeric binders should possess good resilience and adhesivity to avoid material delamination, accommodate the large volume change (80 % in the S_8/Li_2S conversion) during cycle, and retard polysulfide leaching. The work presented in **Chapter 5** provides a deeper understanding of the binder's characteristics to achieve these goals. Through a careful selection of monomer and cross-linker, a multi-functional cross-linked binder (poly(AETMAC-*co*-EGDA)) that not only confines the soluble polysulfide species, but also is mechanically robust to allow stable cycling. When coupled

with highly electronic conductive carbon spheres (sulfur host), a crack-free high sulfur loading electrodes ($6\,mg{\cdot}cm^{-2}$) exhibit high areal capacity of $5.6\,mA{\cdot}h{\cdot}cm^{-2}$ after few conditioning cycles at a low electrolyte/sulfur ratio of $7\,mL : 1\,g$. The cell ultimately stabilizes at $\sim 3\,mA{\cdot}h{\cdot}cm^{-2}$ with limited capacity decay for 300 cycles. The excellent cycling performance of poly(AETMAC-*co*-EGDA) is attributed to its lower transfer-coefficient in comparison with that of the DADMAC. As a result, the polyelectrolyte is able to maintain stronger charge-transfer interactions between its quaternary ammonium group and polysulfides, in comparison with the poly(DADMAC-*co*-EGDA) binder. The tighter network also improves the tensile strength, Young's modulus, and toughness of the sulfur electrode. These factors are critical to curb material delamination. Notably, the excellent compatibility of the polymeric material with the selected casting solvent permits a conventional slurry process, which maximizes electrode packing efficiency and is commensurate with current industrial protocols.

In summary, the approaches to fabricate healthy sulfur cathodes then come down to (a) minimize polysulfides shuttling by host material's chemical interactions and (b) reinforce cathode architecture through polymer binders with high compatibility.

Chapter 6 presents a major breakthrough - the possibility that reversible oxygen reduction/oxidation reactions are no longer intrinsically limited by the (su)peroxide species. By increasing the operating temperature to at least 150 °C and using a bifunctional lithiated nickel oxide (Li_xNiO_2) as electrocatalyst, thermodynamics and kinetics barriers for the formation of Li_2O, a chemically begin species, are overcome. The use of an inorganic electrolytes and a non-carbonaceous cathode further circumvents the degradation of organic electrolyte and carbon corrosion by the (su)peroxides - the main

cause of failure in aprotic Li-O_2 cells. As a result, the Li-O_2 cell exhibits stable cycling performance for 100 cycles, accompanied with very low polarization of 0.16 V and high Coulombic efficiency close to 100 %. The reversible formation and oxidation of lithium oxide via a four-electron transfer process further increases theoretical specific energy of Li-O_2 battery to from 3500 $W \cdot h \cdot kg^{-1}$ to 5200 $W \cdot h \cdot kg^{-1}$.

The success of Li-S and Li-O_2 battery systems relies on a robust and safe operation of lithium metal as the anode. The parasitic reactions between the highly reactive Li metal and the conventionally formulated electrolyte leads to electrolyte degradation, amplified by by high-surface area *dendritic* growth of lithium metal. The work in **Chapter 7** describes a an efficient yet facile strategy to protect the lithium by forming a single Li^+ solid electrolyte layer - lithium phosphorus oxynitride - on the Li surface in situ via wet-chemistry approach. This method of preparing LiPON distinguishes itself from the conventional ALD, which is expensive because it requires precise control in many deposition parameters such as temperature, gas flow rate, clean-room setup etc. to obtain a composition-consistent and uniform coating. Instead, the approach proposed here takes the advantages of the cost-effectiveness and simplicity offered by the solution-mediated method. The excellent coating and chemical stability afforded by LiPON endows its Li-S cells to exhibit Coulombic efficiency of at least 80 % without the use of any electrolyte additives.

8.2 Future Prospective

It remains to be proven how Li-S and Li-O_2 battery technologies will flourish.

For instance, the largest impending factor for Li-S technology commercialization is that the battery's energy density advantage over LIB at the cell level is being neutralized by excessive conductive carbon additives in the sulfur cathode matrix. Furthermore, the current Li-S cell design is based on a *near-catholyte* system (i.e. high E/S ratio), which is necessary to ensure a smooth polysulfide dissolution-precipitation process. Otherwise, the high concentration of polysulfides in the electrolyte will result in (a) aggravated polysulfide shuttle; (b) increased electrolyte viscosity; and (c) decreased lithium ion transport kinetics. And yet, to offset the *dead weight* from these inactive components (such as electrolyte, host materials, carbon additives, polymeric binders, etc.), the areal sulfur loading must be at least $5\,\mathrm{mg{\cdot}cm^{-2}}$. Pertinent to this problem is the impediments of electrolyte penetration in the thick electrodes. In order words, closing the gap between lab prototype and commercial batteries necessitates the consideration of these two parameters; and yet, a decade of research has shown it is difficult to resolve these two problems simultaneously. Rather than continuing to be frustrated with this issue, the substitution of organic electrolyte for a SSE materials that have zero solubility for polysulfides and support the presumably solid-solid sulfur/lithium sulfide conversion is a very attractive approach. The future work on Li-S battery research should then focus on constructing all-solid-state Li-S battery.

Moving the spotlight to the neighbouring Li-O_2 technology, its dream towards commercialization was once almost shattered, can now be reconsidered by resolving cathode/electrolyte decomposition issues. However, there still remain three major challenges that need to resolved. First, there exists an energy density penalty associated with the use of high mass Ni as the electrocatalyst and operating the cell at $150\,^{\circ}\mathrm{C}$ to promote

the conversion of lithium preoxides to oxide. Second, LAGP plays a pivotal role in preventing cell-short circuiting. However, this oxide material is not chemically stable against lithium metal or the molten nitrate electrolyte. Lithium dendrite growth during prolonged cycling can lead to localized reduction of the membrane as depicted in **Figure 6.7**. Instead, the use of garnet-type (e.g. $Li_{0.29}La_{0.57}TiO_3$) solid-state electrolytes is a more viable option because of its excellent stability with Li.[237] Finally, the open-cell architecture and stringent O_2 purity bring a huge burden on practical application for Li-O_2 battery. Similar to Li-S battery, starting the cell at a fully discharge state is an approach. However, the chemical instability of (super)oxide species make that task previously impossible. Instead, with the new oxygen redox pathway, there is hope in pre-loading the cathode with Li_2O particles. The oxygen electrochemistry can now be confined within a sealed cell environment. This approach have been attempted by some of the recent works on Li-O_2 battery that operates solely on the conversion of Li_2O/Li_2O_2 with promising results.[238, 239]

Finally, the implementation of Li metal at the anode is essential for Li-S and Li-O_2 batteries. Future research efforts should be paid towards the use of solid-state electrolytes as a protection layer. In particular, thin, dense, and highly conductive solid electrolytes is a strong candidates. However, artificial interface engineering may be necessary to improve its contact with Li metal.

Once respective problems related Li-S and Li-O_2 battery are tackled, and the major challenges related to lithium anodes are resolved, these battery technologies will no doubt revolutionize the field of electrochemical power sources and will promote the electromobility revolution for the days to come.

References

[1] S. R. James, R. W. Dennell, A. S. Gilbert, H. T. Lewis, J. A. J. Gowlett, T. F. Lynch, W. C. McGrew, C. R. Peters, G. G. Pope, A. B. Stahl, and S. R. James. Hominid use of fire in the lower and middle Pleistocene: A review of the evidence. *Curr. Anthropol.*, 30:1–26, 1989.

[2] World Bank. Fossil fuel energy consumption (% of total). https://data.worldbank.org/indicator/EG.USE.COMM.FO.ZS.

[3] V. Masson-Delmotte, P. Zhai, A. Pirani, S. L. Connors, C. Péan, S. Berger, N. Caud, Y. Chen, L. Goldfarb, M.I. Gomis, M. Huang, K. Leitzell, E. Lonnoy, J. B. R. Matthews, T. K. Maycock, T. Waterfield, O. Yelekçi, R. Yu, and B. Zhou. Climate change 2021: The physical science basis. contribution of working group i to the sixth assessment report of the intergovernmental panel on climate change. Technical report, IPCC, 2021.

[4] Y. Liang, C.-Z. Zhao, H. Yuan, Y. Chen, W. Zhang, J.-Q. Huang, Y. Liu D. Yu, M.-M. Titirici, Y.-L. Chueh, H. Yu, and Q. Zhang. A review of rechargeable batteries for portable electronic devices. *InfoMat*, 1:6–32, 2019.

[5] Christopher Auyeung. Chemical and solar cells. https://www.ck12.org/c/physics/chemical-and-solar-cells/lesson/Chemical-and-Solar-Cells-MS-PS.

[6] M. Li, J. Lu, Z. Chen, and K. Amine. 30 years of lithium-ion batteries. *Adv. Mater.*, 30:1800561, 2018.

[7] J. B. Goodenough. How we made the Li-ion rechargeable battery. *Nat. Electron.*, 1:204–204, 2018.

[8] P. G. Bruce, S. A. Freunberger, L. J. Hardwick, and J.-M. Tarascon. Li-O_2 and Li-S batteries with high energy storage. *Nat. Mater*, 11:19–29, 2012.

[9] Q. Pang, X. Liand, C. Y. Kwok, and L. F. Nazar. Advances in lithium-sulfur batteries based on multifunctional cathodes and electrolytes. *Nature Energy*, 1:16132, 2016.

[10] A. Manthiram, Y. Fu, and Y.-S. Su. Challenges and prospects of lithium-sulfur batteries. *Acc. Chen. Res.*, 46:1125–1134, 2013.

[11] G. Offer S. Waluś, I. Hunt, Y. Patel, T. Stockley, J. Williams., and R. Purkayastha. Volumetric expansion of lithium-sulfur cell during operation - Fundamental insight into applicable characteristics. *Energy Storage Mater.*, 10:233–245, 2018.

[12] A. Manthiram, Y. Fu, S.-H. Chung, C. Zu, and Y.-S. Su. Rechargeable lithium-sulfur batteries. *Chem. Rev.*, 114:11751–11787, 2014.

[13] M. Cuisinier, P.-E. Cabelguen, S. Evers, G. He, M. Kolbeck, A. Garsuch, T. Bolin, M. Balasubramanian, and L. F. Nazar. Sulfur speciation in Li-S batteries determined by operando X-ray absorption spectroscopy. *J. Phys. Chem. Lett.*, 4:3227–3232, 2013.

[14] S. Drvarič Talian, G. Kapun, J. Moškon, A. Vizintin, A. Randon-Vitanova, R. Dominko, and M. Gaberšček. Which process limits the operation of a Li-S system? *Chem. Mater.*, 31:9012–9023, 2019.

[15] G. Li, S. Wang, M. Li Y. Zhang, Z. Chen, and J. Lu. Revisiting the role of polysulfides in lithium-sulfur batteries. *Adv. Mater.*, 30:1705590, 2018.

[16] Y. V. Mikhaylik and J. R. Akridge. Polysulfide shuttle study in the Li/S battery system. *J. Electrochem. Soc.*, 151:A1969–A1976, 2004.

[17] J. Speight. *Lange's Handbook of Chemistry*. McGraw-Hill Education, New York, 16^{th} edition, 2005.

[18] X. Ji, K. T. Lee, and L. F. Nazar. A highly ordered nanostructured carbon-sulphur cathode for lithium-sulfur batteries. *Nat. Mater.*, 8:500–506, 2009.

[19] G. He, S. Evers, X. Liang, M. Cuisinier, A. Garsuch, and L. F. Nazar. Tailoring porosity in carbon nanospheres for lithium-sulfur battery cathodes. *ACS Nano*, 7:10920–10930, 2013.

[20] W. Zhou, C. Wang, Q. Zhang, H. D. Abruña, Y. He, J. Wang, S. X. Mao, and X. Xiao. Tailoring pore size of nitrogen-doped hollow carbon nanospheres for confining sulfur in lithium-sulfur batteries. *Adv. Energy Mater.*, 5:1401752, 2015.

[21] D. Gueon, J. T. Hwang, S. B. Yang, E. Cho, K. Sohn, D.-K. Yang, and J. H. Moon. Spherical macroporous carbon nanotune particles with ultrahigh sulfur loading for lithium-sulfur battery cathodes. *ACS Nano*, 12:226–233, 2018.

[22] B. Zhang, X. Qin, G. R. Li, and X. P. Gao. Enhancement of long stability of sulfur cathode by encapsulating sulfur into micropores of carbon spheres. *Energy Environ. Sci.*, 3:1531–1537, 2010.

[23] L. Borchardt, M. Oschatz, and S. Kaskel. Carbon materials for lithium sulfur batteries - ten critical questions. *Chem. Eur. J.*, 22:7324–7351, 2016.

[24] S.-H. Chung, C.-H. Chang, and A. Manthiram. A carbon-cotton cathode with ultrahigh-loading capability for statically and dynamically stable lithium-sulfur batteries. *ACS Nano*, 10:10462–10470, 2016.

[25] G. Zhou, L.-C. Yin, D.-W. Wang, L. Li, S. Pei, I. R. Gentle, F. Li, and H.-M. Cheng. Fibrous hybrid of graphene and sulfur nanocrystals for high-performance lithium-sulfur batteries. *ACS Nano*, 7:5367–5375, 2013.

[26] L. Qie and A. Manthiram. Long-life Li/polysulfide batteries with high sulfur loading enabled by lightweight three-dimensional nitrogen/sulfur-codoped graphene sponge. *Nat. Commun.*, 6:7760, 2015.

[27] Y.-Z. Zhang, Z. Zhang, S. Liu, G.-R. Li, and X.-P Gao. Free-standing porous carbon nanofiber/carbon nanotube film as sulfur immobilizer with high areal capacity for lithium-sulfur battery. *ACS Appl. Mater. Interfaces*, 10:8749–8757, 2018.

[28] G. Zhou, G. S. Hwang E. Paek, and A. Manthiram. A facile layer-by-layer approach for high-areal-capacity sulfur cathodes. *Adv. Mater.*, 27(10):1694–1700, 2015.

[29] N. Kang, Y. Lin, L. Yang, D. Lu, J. Xiao, Y. Qi, and M. Cai. Cathode porosity is a missing key parameter to optimize lithium-sulfur battery energy density. *Nat. Commun.*, 10:4597, 2019.

[30] R. Sahore, B. D. A. Levin, M. Pan, D. A. Muller, F. J. DiSalvo, and E. P. Giannelis. Design principles for optimum performance of porous carbons in lithium-sulfur batteries. *Adv. Energy Mater.*, 6:1600134, 2016.

[31] Y. Yang, G. Yu, J. J. Cha, H. Wu, M. Vosgueritchian, Y. Yao, Z. Bao, and Y. Cui. Improving the performance of lithium-sulfur batteries by conductive polymer coating. *ACS Nano*, 5:9187–9193, 2011.

[32] L. Ma, H. Zhuang, Y Lu, S. S. Moganty, R. G. Hennig, and L. A. Archer. Tethered molecular sorbents: enabling metal-sulfur battery cathodes. *Adv. Energy Mater.*, 4:1400390, 2014.

[33] Y. Shi, L. Peng, Y. Ding, and G. Yu. Nanostructured conductive polymers for advanced energy storage. *Chem. Soc. Rev.*, 44:6684–6696, 2015.

[34] L. Ji, M. Rao, H. Zheng, L. Zhang, Y. Li, W. Duan, E. J. Cairns, and Y. Zhang. Graphene oxide as a sulfur immobilizer in high performance lithium/sulfur cells. *J. Am Chem. Soc.*, 133:18522–18525, 2011.

[35] L Zhang, L. Li, P.-A. Glans, Y. Zhang, J. Zhu, and J. Guo. Electronic structure and chemical bonding of a graphene oxide-sulfur nanocomposite for use in superior performance lithium-sulfur cells. *Phys. Chem. Chem. Phys.*, 14:13670–13675, 2012.

[36] H. Yuan, W. Zhang, J.-G. Wang, G. Zhou, Z. Zhuang, J. Luo, H. Huang, Y. Gan, C. Liang, Y. Xia, J. Zhang, and X. Tao. Facilitation of sulfur evolution reaction by pyridinic nitrogen doped carbon manoflakes for highly-stable lithium-sulfur batteries. *Energy Storage Mater.*, 10:1–9, 2018.

[37] L.-C. Yin, J. Liang, G.-M. Zhou, F. Li, R. Saito, and H.-M. Cheng. Understanding the interactions between lithium polysulfide and N-doped graphene using density functional theory calculations. *Nano Energy*, 25:203–210, 2016.

[38] Z. W. Seh, Q. Zhang, W. Li, G. Zheng, H. Yao, and Y. Cui. Stable cycling of lithium sulfide cathodes through strong affinity with a bifunctional binder. *Chem. Sci.*, 4:3673–3677, 2013.

[39] X. Tao, J. Wang, C. Liu, H. Wang, H. Yao, G. Zheng, S. W. Seh, Q. Cai, W. Li, G. Zhou, and Y. Cui. Balancing surface adsorption and diffusion of lithium-polysulfides on nonconductive oxides for lithium-sulfur battery design. *Nat. Commun.*, 7(11203), 2016.

[40] S. Evers, T. Yim, and L. F. Nazar. Understanding the nature of absorption/adsorption in nanoporous polysulfide sorbents for the Li-S Battery. *J. Phys. Chem. C*, 116:19653–19658, 2012.

[41] Q. Pang, D. Kundu, M. Cuisinier, and L. F. Nazar. Surface-enhanced redox chemistry of polysulphides on a metallic and polar host for lithium-sulphur batteries. *Nat. Commun.*, 5:4759, 14.

[42] X. Chen, H.-J. Peng, R. Zhang, l Hou T.-Z, Huang J.-Q, B. Li, and Q. Zhang. An analogous periodic law for strong anchoring of polysulfides on polar hosts in lithium sulfur batteries: S- or Li-binding on first-row transitional-metal sulfides? *ACS Energy Lett.*, 2:795–801, 2017.

[43] W. Xue, Z. Shi, L. Suo, C. Wang, Z. Wang, H. Wang, K. P. So, A. Maurano, D. Yu, Y. Chen, L. Qie, Z. Zhu, G. Xu, J. Kong, and J. Li. Intercalation-conversion hybrid cathodes enabling Li-S full-cell architectures with jointly superior gravimetric and volumetric energy densities. *Nat. Energy*, 4:374–382, 2019.

[44] Q. Pang, D. Kundu, and L. F. Nazar. A graphene-like metallic cathode host for long-life and high-loading lithium–sulfur batteries. *Mater. Horiz.*, 3:130–136, 2016.

[45] G. Zhou, H. Tian, Y. Jin, X. Tao, B. Liu, R. Zhang, Z. W. Seh D. Zhou, Y. Liu, J. Sun, J. Zhao, C. Zu, D. S. Wu, Q. Zhand, and Y. Cui. Catalytic oxidation of Li_2S on the surface of metal sulfides for Li-S batteries. *Proc. Natl. Acad. Sci. U.S.A.*, 114:840–845, 2017.

[46] H.-J. Peng, G. Zhang, X. Chen, Z.-W. Zhang, W.-T. Xu, J.-Q. Huand, and Q. Zhang. Enhanced electrochemical kinetics on conductive polar mediators for lithium-sulfur batteries. *Angew. Chem. Int. Ed.*, 55:12990–12995, 2016.

[47] M.-S. Song, S.-C. Han, H.-S. Kim, J.-H. Kim, K.-T. Kim, Y.-M. Kang, H.-J. Ahn, S. X. Dou, and J.-Y. Lee. Effects of nanosized adsorbing material on electrochemical properties of sulfur cathodes for Li/S secondary batteries. *J. Electrochem. Soc.*, 151:A791, 2004.

[48] C. Ye, Y. Jiao, H. Jin, A. D. Slattery, K. Davey, H. Wang, and S.-Z. Qiao. 2D MoN-VN heterostructure to regulate polysulfides for highly efficient lithium-sulfur batteries. *Angew. Chem. Int. Ed.*, 57:16703–16707, 2018.

[49] Q. Pang, C. Y. Kwok, D. Kundu, X. Liang, and L. F. Nazar. Lightweight metallic MgB_2 mediates polysulfide redox and promises high-energy-density lithium-sulfur batteries. *Joule*, 3(1):136–148, 2019.

[50] S. Huang, Y. V. Lim, X. Zhang, Y. Wang, Y. Zheng, D. Kong, M. Ding, S. A. Yang, and H. Y. Yang. Regulating the polysulfide redox conversion by iron phosphide nanocrystals for high-rate and ultrastable lithium-sulfur battery. *Nano Energy*, 51:340–348, 2018.

[51] J. He and A. Manthiram. A review on the status and challenges of electrocatalysts in lithium-sulfur batteries. *Energy Storage Mater.*, 20:55–70, 2019.

[52] X. Hong and R. Wang and Y. Liu and J. Fu and J. Liang and S. Dou. Recent advances in chemical adsorption and catalytic conversion materials for Li-S batteries. *J. Energy Chem.*, 42:144 – 168, 2020.

[53] Y. Song, Cai W, L. Kong, J. Cai, Q. Zhang, and J. Sun. Rationalizing electrocatalysis of Li-S chemistry by mediator design: progress and prospects. *Adv. Energy Mater.*, 10:1901075, 2020.

[54] X. Liang, C. Hart, Q. Pang, A. Garsuch, T. Weiss, and L. F. Nazar. A highly efficient polysulfide mediator for lithium-sulfur batteries. *Nat. Commun*, 6:5682, 2015.

[55] Q. Pang, X. Liang, C. Y. Kwok, and L. F. Nazar. Review - the importance of chemical interactions between sulfur host materials and lithium polysulfides for advanced lithium-sulfur batteries. *J. Electrochem. Soc.*, 162:A2567–A2576, 2015.

[56] W. C. Wake. *Adhesion and the Formulation of Adhesives.* Applied Science Pubs, 2nd edition, 1982.

[57] P. Bhattacharya, M. I. Nandasiri, D. Lv, A. M. Schwarz, J. T. Darsell, W. A. Henderson, D. A. Tomalia, J. Liu, J.-G. Zhand, and J. Xiao. Polyamidoamine dendrimer-based binders for high-loading lithium–sulfur battery cathodes. *Nano Energy*, 19:176–186, 2016.

[58] G. Zheng, Q. Zhang, J. J. Cha, Y. Yang, W. Li, Z. W. Seh, and Y. Cui. Amphiphilic surface modification of hollow carbon nanofibers for improved cycle life of lithium sulfur batteries. *Nano Letters*, 13:1265–1270, 2013.

[59] M. Shaibani, M. S. Mirshekarloo, R. Singh, C. D. Easton, M. C. D. Cooray, N. Eshraghi, T. Abendroth, S. Dörfler, H. Althues, S. Kaskel, A. F. Hollenkamp, M. R. Hill, and M. Majumder. Expansion-tolerant architectures for stable cycling of ultrahigh-loading sulfur cathodes in lithium-sulfur batteries. *Sci. Adv.*, 6:eaay2757, 2020.

[60] Q. Pang, X. Liang, C. Y. Kwok, J. Kulisch, and L. F. Nazar. A comprehensive approach toward stable lithium-sulfur batteries with high volumetric energy density. *Adv. Energy Mater.*, 7:1601630, 2017.

[61] H. Arai, J. Garche, and L. Colmenares, editors. *Electrochemical Power Sources: Fundamentals, Systems, and Applications. Metal-Air Batteries: Present and Perspective*. Elsevier, 2021.

[62] K. M. Abraham and Z. Jiang. A polymer electrolyte-based rechargeable lithium/oxygen battery. *J. Electrochem. Soc.*, 143:1–5, 1996.

[63] D. Aurbach, B. D. McCloskey, L. F. Nazar, and P. G. Bruce. Advances in understanding mechanisms underpinning lithium-air batteries. *Nat. Energy*, 1:16128, 2016.

[64] L. Johnson, C. Li, Z. Liu, Y. Chen, S. A. Freunberger, P. C. Ashok, B. B. Praveen, K. Dholakia, J.-M. Tarascon, and P. G. Bruce. The role of LiO_2 solubility in O_2 reduction in aprotic solvents and its consequences for Li-O_2 batteries. *Nat. Chem.*, 6:1091–1099, 2014.

[65] S. A. Freunberger, Y. Chen, Z. Peng, J. M. Griffin, L. J. Hardwick, F. Bardé, P. Novák, and P. G. Bruce. Reactions in the rechargeable lithium/O_2 battery with alkyl carbonate electrolytes. *J. Am. Chem. Soc*, 133:8040–8047, 2011.

[66] D. G. Kwabi, T. P. Batcho, C. V. Amanchukwu, N. Ortiz-Vitoriano, P. Hammond, C. V. Thompson, and Y. Shao-Horn. Chemical instability of dimethyl sulfoxide in lithium-air batteries. *J. Phys. Chem. Lett.*, 5:2850–2856, 2014.

[67] S. A. Freunberger, Y. Chen, N. E. Drewett, L. J. Hardwick, F. Bardé, and P. G. Bruce. The lithium-oxygen battery with ether-based electrolytes. *Angew. Chem. Int. Ed.*, 50:8609–8613, 2011.

[68] B. D. Adams, R. Black, Z. Williams, R. Fernandes, M. Cuisinier, E. J. Berg, P. Novak, G. K. Murphy, and L. F. Nazar. Towards a stable organic electrolyte for the lithium oxygen battery. *Adv. Mater. Energy*, 5:1400867, 2015.

[69] X. Zhang, K. Xu, and Y. Gao. The phase diagram of $LiNO_3$-KNO_3. *Thermochim. Acta*, 385:81–84, 2002.

[70] V. Giordani, D. Tozier, H. Tan, C. M. Burke, B. M. Gallant, J. Uddin, J. R. Greer, B. D. McCloskey, G. V. Chase, and D. Addison. A Molten Salt Lithium–Oxygen Battery. *J. Am. Chem. Soc.*, 138:2656–2663, 2016.

[71] Z. Huang, H. Zeng, M. Xie, X. Lin, Z. Huang, Y. Shen, and Y. Huang. A stable lithium-oxygen battery electrolyte based on fully methylated cyclic ether. *Angew. Chem. Int. Ed.*, 58:2345–2349, 2019.

[72] D. Sharon, P. Sharon, D. Hirshberg, M. Salama, M. Afri, L. J. W. Shimon, W.-J. Kwak, Y.-K. Sun, A. A. Frimer, and D. Aurbach. 2,4-Dimethoxy-2,4-dimethylpentan-3-one: an aprotic solvent designed for stability in Li-O_2 cells. *J. Am. Chem. Soc.*, 139:11690–11693, 2017.

[73] Z. Ma, X. Yuan, L. Li, Z.-F. Ma, D. P. Wilkinson, L. Zhang, and J. Zhang. A review of cathode materials and structures for rechargeable lithium-air batteries. *Energy Environ. Sci.*, 8:2144–2198, 2015.

[74] M. M. Ottaka Thotiyl, S. A. Freunberger, Z. Peng, and P. G. Bruce. The carbon electrode in nonaqueous Li-O_2 cells. *J. Am Chem. Soc*, 135:494–500, 2013.

[75] Z. Peng, S. A. Freunberger, Y. Chen, and P. G. Bruce. A reversible and higher-rate Li-O_2 battery. *Science*, 337:563–566, 2012.

[76] M. M. Ottakam Thotiyl, S. A. Freunberger, Z. Peng, Y. Chen, Z. Liu, and P. G. Bruce. A stable cathode for the aprotic Li-O_2 battery. *Nat. Mater.*, 12:1050–1056, 2013.

[77] B. D. Adams, R. Black, C. Radtke, Z. Williams, B. L. Mehdi, N. D. Browning, and L. F. Nazar. The importance of nanometric passivating films on cathodes for Li-air batteries. *ACS Nano*, 8:12483–12493, 2014.

[78] D. Kundu, R. Black, E. J. Berg, and L. F. Nazar. A highly active nanostructured metallic oxide cathode for aprotic Li_2S_n batteries. *Energy Environ. Sci.*, 8:1292–1298, 2015.

[79] J.-B. Park, I. Belharouak, Y. J. Lee, and Y.-K. Sun. A carbon-free ruthenium oxide/mesoporous titanium dioxide electrode for lithium-oxygen batteries. *J. Power Sources*, 295:299–304, 2015.

[80] M. Asadi, B. Kumar, C. Liu, P. Phillips, P. Yasaei, A. Behranginia, P. Zapol, R. F. Klie, L. A. Curtiss, and A. Salehi-Khojin. Cathode based on molybdenum disulfide nanoflakes for lithium-oxygen batteries. *ACS Nano*, 10:2167–2175, 2016.

[81] B. D. McCloskey, R. Scheffler, A. Speidel, D. S. Bethune, R. M. Shelby, and A. C. Luntz. On the efficacy of electrocatalysis in monaqueous Li-O_2 batteries. *J. Am. Chem. Soc.*, 133:18038–18041, 2011.

[82] M. S. Whittingham. Electrical energy storage and intercalation chemistry. *Science*, 192:1126–1127, 1976.

[83] M. S. Whittingham. Chalcogenide Battery, 1977. US Patent 4009052A.

[84] M. Winter, B. Barnett, and K. Xu. Before Li ion batteries. *Chem. Rev.*, 118:11433–11456, 2018.

[85] H. Hong, N. A. C. Mohamad, K. Chae, F. M. Mota, and D. H. Kim. The lithium metal anode in Li–S batteries: challenges and recent progress. *J. Mater. Chem. A*, 9:10012–10038, 2021.

[86] D. Aurbach and Y. Cohen. The application of atomic force microscopy for the study of Li deposition processes. *J. Electrochem. Soc.*, 143:3525–3532, 1996.

[87] V. Srinivasan, K. Higa, P. Barai, and Y. Xie. *Computational Modeling of Morphology Evolution in Metal-Based Battery Electrodes*. Springer, 2018.

[88] S. Chandrashekar, N. M. Trease, H. J. Chang, L.-S. Du, C. P. Grey, and A. Jerschow. ^{7}Li MRI of Li batteries reveals location of microstructural lithium. *Nat. Mater.*, 11:311–315, 2012.

[89] P. Bai, J. Li, F. R. Brushett, and M. Z. Bazant. Transition of lithium growth mechanisms in liquid electrolytes. *Energy Environ. Sci.*, 9:3221–3229, 2016.

[90] J.-N. Chazalviel. Electrochemical aspects of the generation of ramified metallic electrodeposits. *Phys. Rev. A*, 42:7355–7367, 1990.

[91] C. Brissot, M. Rosso, J.-N. Chazalviel, and S. Lascaud. Dendritic growth mechanisms in lithium/polymer cells. *J. Power Sources*, 81-82:925–929, 1999.

[92] E. Peled. The electrochemical behavior of alkali and alkaline earth metals in nonaqueous battery systems - the solid electrolyte interphase model. *J. Electrochem. Soc.*, 126:2047–2051, 1979.

[93] E. Peled, D. Golodnitsky, and G. Ardel. Advanced model for solid electrolyte interphase electrodes in liquid and polymer electrolytes. *J. Electrochem. Soc.*, 144:L208–L210, 1997.

[94] X.-B. Cheng, R. Zhang, C.-Z. Zhao, and Q. Zhang. Toward safe lithium metal anode in rechargeable batteries: a review. *Chem. Rev.*, 117:10403–10473, 2017.

[95] Y. S. Cohen, Y. Cohen, and D. Aurbach. Micromorphological studies of lithium electrodes in alkyl carbonate solutions using in situ atomic force microscopy. *J. Phys. Chem. B*, 104:12282–12291, 2000.

[96] M. Rosso, T. Gobron, C. Brissot, J.-N. Chazalviel, and S. Lascaud. Onset of dendritic growth in lithium/polymer cells. *J. Power Sources*, 97-98:804–806, 2001.

[97] E. Peled and S. Menkin. Review - sei: past, present and future. *J. Electrochem. Soc.*, 164:A1703–A1719, 2017.

[98] S. Nanda and A. Manthiram. Lithium degradation in lithium–sulfur batteries: insights into inventory depletion and interphasial evolution with cycling. *Energy Environ. Sci.*, 13:2501–2514, 2020.

[99] C. Fend, J. Li, M. Zhang, Y. Zhang, F. Yang, J. Z. lee, M.-H. Lee, J. Alvarado, M. S. Schroeder, Y. Yang, B. Lu, N. Williams, M. Ceja, L. Yang, M. Cai, J. Gu, K. Xu, X. Wang, and Y. S. Meng. Quantifying inactive lithium in lithium metal batteries. *Nature*, 572:511–515, 2019.

[100] D. Ayrback, E. Pollak, R. Elazari, G. Salitra, C. S. Kelley, and J. Affinito. On the surface chemical aspects of very high energy density, rechargeable Li-sulfur batteries. *J. Electrochem. Soc.*, 156:A694–A702, 2009.

[101] F. Wu, J. Qian, R. Chen, J. Lu, L. Li, H. Wu, J. Chen, T. Zhao, Y. Ye, and K. Amine. An effective approach to protect lithium anode and improve cycle performance for Li-S batteries. *ACS Appl. Mater. Interfaces*, 6:15542–15549, 2014.

[102] R. Yemini and M. Noked. Effect of polysulfide species on lithium anode cycle life and reversibility in Li-S batteries. *ACS Appl. Energy Mater.*, 4:4711–4718, 2021.

[103] G. Zhou, Y. Zhao, and A. Manthiram. Dual-confined flexible sulfur cathodes encapsulated in nitrogen-doped double-shelled hollow carbon spheres and Wrapped with graphene for Li-S batteries. *Adv. Energy Mater.*, 5:1402263, 2015.

[104] M. Cuisinier, C. Hart, M. Balasubramanian, A. Garsuch, and L. F. Nazar. Radical or not radical: revisiting lithium-sulfur electrochemistry in nonaqueous electrolytes. *Adv. Energy Mater.*, 5:1401801, 2015.

[105] S. Ha, Y. Kim, D. Koo, K.-H. Ha, Y. Park, D.-M. Kim, S. Son, T. Yim, and K. T. Lee. Investigation into the stability of Li metal anodes in Li-O_2 batteries with a redox mediator. *J. Mater. Chem. A*, 5:10609–10621, 2017.

[106] M.-H. Ryou, Y. M. Lee, Y. Lee, Ma. Winter, and P. Bieker. Mechanical surface modification of lithium metal: towards improved Li metal anode performance by directed Li plating. *Adv. Funct. Mater.*, 25:834–841, 2015.

[107] D. Lin, Y. Liu, Z. Liang, H.-W. Lee, J. Sun, H. Wang, K. Yan, J. Xie, and Y. Cui. Layered reduced graphene oxide with nanoscale interlayer gaps as a stable host for lithium metal anodes. *Nat. Nanotechnology*, 11:626–632, 2016.

[108] Z. Liang, D. Lin, J. Zhao, Z. Lu, Y. Liu, C. Liu, Y. Lu, H. Wang, K. Yan, and X. Tao. Composite lithium metal anode by melt infusion of lithium into a 3D conducting scaffold with lithiophilic coating. *Proc. Natl. Acad. Sci. U.S.A.*, 113:2862–2867, 2016.

[109] F. Ding, W. Xu, G. L. Graff, J. Zhang, M. L. Sushko, X. Chen, Y. Shao, M. H. Engelhard, Z. Nie, and J. Xiao. Dendrite-free lithium deposition via self-healing electrostatic shield mechanism. *J. Am. Chem. Soc.*, 135:4450–4456, 2013.

[110] B. Liu, W. Xu, P. Yan, X. Sun, M. E. Bowden, J. Read, J. Qian, D. Mei, C.-M. Wang, and J.-G. Zhang. Enhanced cycling stability of rechargeable Li-O_2 batteries Using high-concentration electrolytes. *Adv. Funct. Mater.*, 26:605–613, 2016.

[111] F. Wu, Y.-X. Yuan, X.-B. Cheng, Y. Bai, Y. Li, C. Wu, and Q. Zhang. Perspectives for restraining harsh lithium dendrite growth: towards robust lithium metal anodes. *Energy Storage Mater.*, 15:148–170, 2018.

[112] D. Lin, Y. Liu, and Y. Cui. Reviving the lithium metal anode for high-energy batteries. *Nat. Nanotechnology*, 12:194–206, 2017.

[113] B. Liu, J.-G. Zhang, and W. Xu. Advancing lithium metal batteries. *Joule*, 2:833–845, 2018.

[114] Y. V. Mikhaylik. Electrolytes for lithium sulfur cells, 2008. US Patent 7,354,680 B2.

[115] S. Xiong, K. Xie, Y. Diao, and X. Hong. Properties of surface film on lithium anode with $LiNO_3$ as lithium salt in electrolyte solution for lithium–sulfur batteries. *Electrochim. Acta*, 83:78–86, 2012.

[116] W. Li, H. Yao, K. Yan, G. Zheng, Z. Liang, Y.-M. Chiang, and Y. Cui. The synergetic effect of lithium polysulfide and lithium nitrate to prevent lithium dendrite growth. *Nat. Commun.*, 6:7436, 2015.

[117] L. Zhang, M. Lingm, J. Feng, L. Mai, G. Liu, and J. Gao. The synergetic interaction between $LiNO_3$ and lithium polysulfides for suppressing shuttle effect of lithium-sulfur batteries. *Energy Storage Mater.*, 11:24–29, 2018.

[118] S. S. Zhang. Role of $LiNO_3$ in rechargeable lithium/sulfur battery. *Electrochim. Actaa*, 70:344–348, 2012.

[119] X. Yu, Z. Bi, F. Zhao, and A. Manthiram. Polysulfide-shuttle control in lithium-sulfur batteries with a chemically/electrochemically compatible NaSICON-type solid electrolyte. *Adv. Energy Mater*, 6:1601392, 2016.

[120] Q. Pang, X. Liang, A. Shyamsunder, and L. F. Nazar. An in vivo formed solid electrolyte surface layer enables stable plating of Li metal. *Joule*, 1:871–886, 2017.

[121] Q. Pang, L. Zhou, and L. F. Nazar. Elastic and Li-ion–percolating hybrid membrane stabilizes Li metal plating. *Proc. Natl. Acad. Sci. U.S.A.*, 115:12389–12394, 2018.

[122] ETH zurich. Bragg's Law of diffraction. https://www.microscopy.ethz.ch/bragg.htm.

[123] Alex Ilitchev. SEM: types of electron and the information they provide. https://https://www.thermofisher.com/blog/microscopy/seeing-with-electrons-the-anatomy-of-an-electron-microscope.

[124] K. Siegbahn and K. Edvarson. β-Ray spectroscopy in the precision range of 1 : 105. *Nuclear Phys*, 1:137–159, 1956.

[125] S. Brunauer, P. H. Emmett, and E. Teller. Adsorption of gases in mutimolecular layer. *J. Am. Chem. Soc.*, 60:309–319, 1938.

[126] C. J. Hart, M. Cusinier, X. Liang, D. Kundu, A. Garsuch, and L. F. Nazar. Rational design of sulphur host materials for Li-S batteries: correlating lithium polysulphide adsorptivity and self-discharge capacity loss. *Chem Commun.*, 51:2308–2311, 2015.

[127] O. Wolter and J. Heitbaum. Differential electrochemical mass spectroscopy (DEMS) - a New method for the study of electrode processes. *Berichte der Bunsengesellschaft für physikalische Chemie*, 88:2–6, 1984.

[128] G. Santoiemma. Recent methodologies for studying the soil organic matter. *Appl. Soil Ecol.*, 123:546–550, 2018.

[129] R. Black. *The impact of degradation reactions on aprotic metal-O_2 battery performance*. PhD thesis, University of Waterloo, 2016.

[130] J. Zheng, J. Tian, D. Wu, M. Gu, W. Xu, C. Wang, F. Gao, M. H. Engelhard, J.-G. Zhang, J. Liu, and J. Xiao. Lewis acid-base interactions between polysulfides and metal organic framework in lithium sulfur batteries. *Nano Letters*, 14:2345–2352, 2014.

[131] X. Liang, A. Garsuch, and L. F. Nazar. Sulfur cathodes based on conductive MXene nanosheets for high-performance lithium-sulfur batteries. *Angew. Chem. Int. Ed.*, 54:3907–3911, 2015.

[132] Y. Liang, Y. Li, H. Wang, J. Zhou, J. Wang, T. Regier, and H. Dai. Co_3O_4 nanocrystals on graphene as a synergistic catalyst for oxygen reduction reaction. *Nat. Mater.*, 10:780–786, 2011.

[133] K. Nakagawa, R. Konaka, and T. Nakata. Oxidation with nickel peroxide. I. Oxidation of alcohols. *J. Org. Chem.*, 27:1597–1601, 1962.

[134] Z. H. Gan, G. Q. Yu, B. K. Tay, C. M. Tan, Z. W. Zhao, and Y. Q. Fu. Preparation and characterization of copper oxide thin films deposited by filtered cathodic vacuum arc. *J. Phys. D. Appl. Phys.*, 37:81–85, 2003.

[135] M. C. Biesinger, L. W. M. Lau, A. R. Gerson, and R. St. C. Smart. Resolving surface chemical states in XPS analysis of first row transition metals, oxides and hydroxides: Sc, Ti, V, Cu and Zn. *Appl. Surf. Sci.*, 257:887–898, 2010.

[136] G. C. Bond and J. B. P. Tripathi. Investigation of the decomposition and reduction of "nickel peroxide" by thermal analysis. *J. Chem. Soc., Faraday Trans. 1*, 73:545, 1977.

[137] L. M. Moroney, R. St C. Smart, and M. W. Roberts. Studies of the thermal decomposition of β-NiO(OH) and nickel peroxide by X-ray photoelectron spectroscopy. *J. Chem. Soc., Faraday Trans. 1*, 79:1769, 1983.

[138] M. C. Biesinger, B. P. Payne, L. W. M. Lau, A. Gerson, and R. St. C. Smart. X-ray photoelectron spectroscopic chemical state quantification of mixed nickel metal, oxide and hydroxide systems. *Surf. Interface Analy.*, 41:324–332, 2009.

[139] H. Li, P. He, Y. Wang, E. Hosono, and H. Zhou. High-surface vanadium oxides with large capacities for lithium-ion batteries: from hydrated aerogel to nanocrystalline VO_2(B), V_6O_{13} and V_2O_5. *J. Mater. Chem.*, 21:10999, 2011.

[140] E. Hryha, E. Rutqvist, and L. Nyborg. Stoichiometric vanadium oxides studied by XPS. *Surf. Interface Anal.*, 44:1022–1025, 2012.

[141] C. N. Berglund and H. J. Guggenheim. Electronic Properties of VO_2 near the semiconductor-metal Transition. *Phys. Rev.*, 185:1022–1033, 1969.

[142] M. Soltani, M. Chaker, E. Haddad, R. V. Kruzelecky, and J. Margot. Effects of Ti-W codoping on the optical and electrical switching of vanadium dioxide thin films grown by a reactive pulsed laser deposition. *Appl. Phys. Lett.*, 85:1958–1960, 2004.

[143] M. Naguib, O. Mashtalir, J. Carle, V. Presser, J. Lu, L. Hultman, Y. Gogotsi, and M. W. Barsoum. Two-dimensional transition metal carbides. *ACS Nano*, 6:1322–1331, 2012.

[144] M. Naguib, V. N. Mochalin, M. W. Barsoum, and Y. Gogotsi. 25^{th} anniversary article: MXenes: A new family of two-dimentional materials. *Adv. Mater.*, 26:992–1005, 2015.

[145] M. Naguiband Y. Gogotsi. Synthesis of two-dimensional materials by selective extraction. *Acc. Chem. Res.*, 48:128–135, 2015.

[146] M. Naguib, J. Halim, J. Lu, K. M. Cook, L. Hultman, Y. Gogotsi, and M. W. Barsoum. New two-dimensional niobium and vanadium carbides as promising materials for Li-Ion batteries. *J. Am. Chem. Soc.*, 135:15966–15969, 2013.

[147] P. Prieto and R. E. Kirby. X-ray photoelectron spectroscopy study of the difference between reactively evaporated and direct sputter-deposited TiN films and their oxidation properties. *J. Vacc. Sci. Technol. A*, 13:2819–2826, 1995.

[148] M. Kurtoglu, M. Naguib, Y. Gogotsi, and M. W. Barsoum. First principles study of two-dimensional early transition metal carbides. *MRS Commun.*, 2:133–137, 2012.

[149] O. Mashtalir, M. Naguib, V. N. Mochalin, Y. Dall'Agnese, M. Heon, M. W. Barsoum, and Y. Gogotsi. Intercalation and delamination of layered carbides and carbonitrides. *Nat. Commun.*, 4:1716, 2013.

[150] V. A. Davis, N. G. Parra-Vasquez, M. J. Grren, P. K. Rai, N. Behabtu, R. D. Booker, J. Schmidt, E. Kesselman, W. Zhou, H. Fan, W. W. Adams, R. H. Hauge, J. E. Fisher, Y. Cohen, Y. Talmon, R. S. Smalley, and M. Pasquali. True solutions

of single-walled carbon nanotubes for assembly into macroscopic materials. *Nat. Nanotechnol.*, 4:830–834, 2009.

[151] G. Li, M. Ling, Y. Ye, Z. Li, J. Guo, Y. Yao, J. Zhu, Z. Lin, and S. Zhang. *Acacia Senegal*-inspired bifunctional binder for longevity of Lithium-Sulfur Batteries. *Adv. Energy Mater.*, 5:1500878, 2015.

[152] L. Wang, D. Wang, F. Zhang, and J. Jin. Interface chemistry guided long-cycle-life Li-S battery. *Nano Lett.*, 13:4206–4211, 2013.

[153] J. Liu, D. G. D. Galpaya, L. Yan, M. Sun, Z. Lin, C. Yan, C. Liang, and S. Zhang. Exploiting a robust biopolymer network binder for an ultrahigh-areal-capacity Li-S battery. *Energy Environ. Sci.*, 10:750–755, 2017.

[154] T. D. Li, L. Pascal, Connell J. G., F. Y. Fan, S. M. Meckler, L. Ma, Y.-M. Chiang, D. Prendergast, and B. A. Helms. Molecular understanding of polyelectrolyte binders that actively regulate ion transport in sulfur cathodes. *Nat.Commun.*, 8:2277, 2017.

[155] K. Park, J. H. Cho, J.-H. Cho, B.-C. Yu, A. T. de la Hoz amd K. M. Miller, C. J. Ellison, and J. B. Goodenough. Trapping lithium polysulfides of a Li-S battery by forming lithium bonds in a polymer matrix. *Energy Environ. Sci.*, 8:2389–2395, 2015.

[156] S. Shen, Z. Zhu, and F. Liu. Introduction of poly[(2-acryloyloxyethyl trimethyl ammonium chloride)-co-(acrylic acid)] branches onto starch for cotton warp sizing. *Carbohydr. Polym.*, 138:280–289, 2016.

[157] M. Aly Saad Aly, M. Gauthier, and J. Yeow. On-chip cell lysis by antibacterial non-leaching reusable quaternary ammonium monolithic column. *Biomed. Microdevices*, 2016.

[158] P. Das, S. Ray, A. Bhaumik, B. Banerjee, and C. Mukhopadhyay. Cubic Ag_2O nanoparticle incorporated mesoporous silica with large bottle-neck like mesopores for the aerobic oxidative synthesis of disulfide. *RSC Adv.*, 5:6323–6331, 2015.

[159] M. Ling, W. Yan, A. Kawase, H. Zhao, Y. Fu, V. S. Battaglia, and G. Liu. Electrostatic polysulfides confinement to inhibit redox shuttle process in the lithium sulfur batteries. *ACS Appl. Mater. Interfaces*, 9:31741–31745, 2017.

[160] S. S. Zhang. New insight into liquid electrolyte of rechargeable lithium/sulfur battery. *Electrochim. Acta*, 97:226–230, 2013.

[161] F. He, B. Luo, S. Yuan, B. Liang, C. Choong, and S. O. Pehkonen. PVDF film tethered with RGD-click-poly(glycidyl methacrylate) brushes by combination of direct surface-initiated ATRP and click chemistry for improved cytocompatibility. *RSC Adv.*, 4:105–117, 2014.

[162] T. A Pascal, K. H. Wujcik, D. R. Wang, N. P. Balsara, and D. Prendergast. Thermodynamic origins of the solvent-dependent stability of lithium polysulfides from first principles. *Phys Chem. Chem. Phy.*, 19:1441–1448, 2017.

[163] G. Ai, Y. Dai, Y. Ye, W. Mao, Z. Wang, H. Zhao, Y. Chen, J. Zhu, Y. Fu, V. Battaglia, J. Guo, V. Srinivasan, and G. Liu. Investigation of surface effects through the application of the functional binders in lithium sulfur batteries. *Nano Energy*, 16:28–37, 2015.

[164] J. Liao and Z. Ye. Quaternary ammonium cationic polymer as a superior bifunctional binder for lithium–sulfur batteries and effects of counter anion. *Electrochim. Acta*, 259:626–636, 2018.

[165] J. Liao, Z. Liu, X. Liu, and Z. Ye. Water-soluble linear poly(ethylenimine) as a superior bifunctional binder for lithium-sulfur batteries of improved cell performance. *J. Phys. Chem. C*, 122:25917–25929, 2018.

[166] R. W. Nunes, J. R. Martin, and J. F. Johnson. Influence of molecular weight and molecular weight distribution on mechanical properties of polymers. *Polym. Eng. Sci.*, 22:205–228, 1982.

[167] G. Zhou, L. Lu, C. Ma, S. Wang, Y. Shi, N. Noratkar, W. Ren, F. Li, and H.-M. Cheng. A graphene foam electrode with high sulfur loading for flexible and high energy Li-S batteries. *Nano Energy*, 11:356–365, 2015.

[168] S.-Y. Li, W.-P. Wang, H. Duan, and Y.-G. Guo. Recent progress on confinement of polysulfides through physical and chemical methods. *J. Energy Chem.*, 27:1555–1565, 2018.

[169] J. E. Mark. *Physical Properties of Polymer Handbook*. Springer, New York, 2^{nd} edition, 2007.

[170] J. Zheng, D. Lv, M. Gu, C. Wang, J-G. Zhang, J. Liu, and J. Xiao. How to obtain reproducible results for lithium sulfur batteries? *J. Electrochem. Soc.*, 160:A2288–A2292, 2013.

[171] K. Xu. Electrolytes and interphases in Li-ion batteries and beyond. *Chem. Rev.*, 114:11503–11618, 2014.

[172] H. Gu, J. Guo, H. Wei, S. Guo, J. Liu, Y. Huang, M. Khan, A. Mojammel, X. Wang, D. O. Young, and S. Wei. Strengthened magnetoresistive epoxy nanocomposite papers derived from synergistic nanomagnetite-carbon nanofiber nanohybrids. *Adv. Mater.*, 27:6277–6282, 2015.

[173] H. Gu, S. Tadakamalla, X. Zhang, Y. Huang, Y. Jiang, H. A. Colorado, Z. Luo, S. Wei, and Z. Guo. Epoxy resin nanosuspensions and reinforced nanocomposites from polyaniline stabilized multi-walled carbon nanotubes. *J. Mater. Chem. C*, 1:729–743, 2013.

[174] J. Tomastik and R. Ctvrlik. Nanoscratch test - a tool for evaluation of cohesive and adhesive properties of thin films and coatings. *EPJ Web Conf.*, 48:00027, 2013.

[175] A. Chen, M. Ling, L. Hencz, H. Ling, G. Li, Z. Lin, G. Liu, and S. Zhang. Exploring chemical, mechanical, and electrical functionalities of binders for advanced energy-storage devices. *Chem. Rev.*, 118:8936–8982, 2018.

[176] S. S. Zhang. A concept for making poly(ethylene oxide) based composite gel polymer electrolyte lithium/sulfur battery. *J. Electrochem. Soc.*, 160:A1421–A1424, 2013.

[177] L. Xiao, Y. Cao, J. Xiao, B. Schwenzer, M. H. Engelhard, L. V. Saraf, Z. Nie, G. J. Exarhos, and J. Liu. A soft approach to encapsulate sulfur: polyaniline nanotubes for lithium-sulfur batteries with long cycle life. *Adv. Mater.*, 24:1176–1181, 2012.

[178] D. Sharon, D. Hirshberg, M. Afri, A. Garsuch, A. A. Frimer, and D. Aurbach. Lithium-oxygen electrochemistry in non-aqueous solutions. *Isr. J. Chem.*, 55:508–520, 2015.

[179] T. A. Pascal, K. H. Wujcik, J. Velasco-Velez, C., A. A. Teran, M. Kapilashrami, J. Cabana, J. Guo, M. Salmeron, N. Balsara, and D. Nitash. X-ray absorption spectra of dissolved polysulfides in lithium sulfur batteries from first-principles. *J. Phys. Chem. Lett.*, 5:1547–1551, 2014.

[180] S. H. Black, R.and Oh, J.-H. Lee, T. Yim, B. Adams, and . F. Nazar. Screening for superoxide reactivity in Li-O_2 batteries: effect on Li_2O_2/LiO crystallization. *J. Am. Chem. Soc.*, 134:2902–2905, 2012.

[181] T. Liu, M. Leskes, W. Yu, A. J. Moore, L. Zhou, P. M. Bayley, G. Kim, and C. P. Grey. Cycling Li-O_2 batteries via LiOH formation and decomposition. *Science*, 350(6260):530–533, 2015.

[182] C. M. Burke, R. Black, I. R. Kochetkov, V. Giordani, D. Addison, L. F. Nazar, and B. D. McCloskey. Implications of $4e^-$ oxygen reduction via iodide redox mediation in Li-O_2 batteries. *ACS Energy Lett.*, 1:747–756, 2016.

[183] C. L. Bender, P. Hartmann, M. Vračar, P. Adelhelm, and J. Janek. On the thermodynamics, the role of the carbon cathode, and the cycle life of the sodium superoxide (NaO_2) battery. *Adv. Energy Mater.*, 4:1301863, 2014.

[184] X. Gao, Y. Chen, L. Johnson, and P. G. Bruce. Promoting solution phase dishcarge in Li-O_2 batteries containing weakly solvating electrolyte solution. *Nat. Mater.*, 15:882–888, 2016.

[185] K. S. Kim and N. Winograd. X-ray photoelectron spectroscopic studies of nickel-oxygen surfaces using oxygen and argon ion-bombardment. *Surf. Sci.*, 43:625–643, 1974.

[186] A. W. Moses, H. G. Garcia Flores, and M. A. Kim, J.-G. Langell. Surface properties of $LiCoO_2$, $LiNiO_2$ and $LiNi_{1-x}Co_xO_2$. *Appl. Sur. Sci.*, 253:4782–4791, 2007.

[187] A. N. Mansour. Characterization of $LiNiO_2$ by XPS. *Surf. Sci. Spectra*, 3:279–286, 1994.

[188] S. Aduru, S. Contarini, and J. W. Rabalais. Electron-, x-ray-, and ion-stimulated decomposition of nitrate salts. *J. Phys. Chem.*, 90:1683–1688, 1986.

[189] N. B. Aetukuri, B. D. Mccloskey, J. M. García, L. E. Krupp, V. Viswanathan, and Alan C. L. Solvating additives drive solution-mediated electrochemistry and enhance toroid growth in non-aqueous Li-O_2 batteries. *Nat. Chem.*, 7:50–56, 2015.

[190] C. Xia, R. Black, R. Fernandes, B. Adams, and L. F. Nazar. The critical role of phase-transfer catalyst in aprotic sodium oxygen batteries. *Nat. Chem.*, 7:496–501, 2015.

[191] P. Hartmann, M. Heinemann, C. L. Bender, K. Graf, R.-P. Baumann, P.p Adelhelm, C. Heiliger, and J. Janek. Discharge and charge reaction paths in sodium-oxygen batteries: Does NaO_2 form by direct electrochemical growth or by precipitation from solution? *J. Phys. Chem. C*, 119:22778–22786, 2015.

[192] M. J. Welland, K. C. Lau, P. C. Redfern, L. Liang, D. Zhai, D. Wolf, and L. A. Curtiss. An atomistically informed mesoscale model for growth and coarsening during discharge in lithium-oxygen batteries. *J. Chem. Phys.*, 143:224113, 2015.

[193] B. D. McCloskey, D. S. Bethune, R. M. Shelby, T. Mori, R. Scheffler, A. Speidel, M. Sherwood, and A. C. Luntz. Limitations in rechargeability of Li-O_2 batteries and possible origins. *J. Phys. Chem. Lett.*, 3:3043–3047, 2012.

[194] C. Xia, R. Fernandes, F. H. Cho, N. Sudhakar, B. Buonacorsi, S. Walker, M. Xu, J. Baugh, and L. F. Nazar. Direct evidence of solution-mediated superoxide transport and organic radical formation in Na-O_2 batteries. *J. Am. Chem. Soc*, 138:11219–11226, 2016.

[195] W. Chia-Ching and Y. Cheng-Fu. Investigation of the properties of nanostructured Li-doped NiO films using the modified spray pyrolysis method. *Nanoscale Res. Lett.*, 8:33, 2013.

[196] P. Hartmann, T. Leichtweiss, M. R. Busche, M. Schneider, M. Reich, J. Sann, P. Adelhelm, and J. Janek. Degradation of NASICON-type materials in contact with lithium metal: formation of mixed conducting interphases (MCI) on solid electrolytes. *J. Phys. Chem. C*, 117:21064–21074, 2013.

[197] B. D. Adams, C. Radtke, R. Black, M. L. Trudeau, K. Zaghib, and L. F. Nazar. Current density dependence of peroxide formation in the Li-O_2 battery and its effect on charge. *Energy Environ. Sci.*, 6:1772, 2013.

[198] N. Markovic. Surface science studies of model fuel cell electrocatalysts. *Surf. Sci. Rep.*, 45:117–229, 2002.

[199] C. M. Sánchez-Sánchez and A. J. Bard. Hydrogen peroxide production in the oxygen reduction reaction at different electrocatalysts as quantified by scanning electrochemical microscopy. *Anal. Chem.*, 81:8094–8100, 2009.

[200] J. Suntivich, H. A. Gasteiger, Naoaki Y., H. Nakanishi, J. B. Goodenough, and Y. Shao-Horn. Design principles for oxygen-reduction activity on perovskite oxide catalysts for fuel cells and metal–air batteries. *Nat. Chem.*, 3:546–550, 2011.

[201] Y. Koyama, T. Mizoguchi, H. Ikeno, and I. Tanaka. Electronic structure of lithium nickel oxides by electron energy loss spectroscopy. *J. Phys. Chem. B*, 109:10749–10755, 2005.

[202] S. Srinivasan. *Fuel Cells: From Fundamentals to Applications*. Springer, New York, 1st ed. edition, 2010.

[203] J. Suntivich, K. J. May, H. A. Gasteiger, J. B. Goodenough, and Y. Shao-Horn. A perovskite oxide optimized for oxygen evolution catalysis from molecular orbital principles. *Science*, 334:1383–1385, 2011.

[204] Z. W. Seh, J. Kibsgaard, C. F. Dickens, I. Chorkendorff, J. K. Nørskov, and T. F. Jaramillo. Combining theory and experiment in electrocatalysis: insights into materials design. *Science*, 355:eaad4998, 2017.

[205] M. E. Scofield, H. Liu, and S. S. Wong. A concise guide to sustainable PEMFCs: recent advances in improving both oxygen reduction catalysts and proton exchange membranes. *Chem. Soc. Rev.*, 44:5836–5860, 2015.

[206] C.-P. Yang, Y.-X. Yin, S.-F. Zhang, N.-W. Li, and Y.-G. Guo. Accommodating lithium into 3D current collectors with a submicron skeleton towards long-life lithium metal anodes. *Nat. Commun.*, 6:8058, 2015.

[207] J. Qian, W. A. Henderson, W. Xu, P. Bhattacharya, M. Engelhard, O. Borodin, and J.-G. Zhang. High rate and stable cycling of lithium metal anode. *Nat. Commun.*, 6:6362, 2015.

[208] L. Suo, Y.-S. Hu, H. Li, M. Armand, and Q. Chen. A new class of Solvent-in-Salt electrolyte for high-energy rechargeable metallic lithium batteries. *Nat. Commun.*, 4:1481, 2013.

[209] Y. Gofer, M. Ben-Zion, and D. Aurbach. Solution of $LiAsF_6$ in 1,3-dioxolane for secondary lithium batteries. *J. Power Sources*, 39:163–178, 1992.

[210] D. Chen, P. Liu, L. Zhong, S. Wang, M. Xiao, D. Han, S. Huang, and Y. Meng. Covalent organic frameworks with low surface work function enabled stable lithium anode. *Small*, pages 163–178, 2021.

[211] Y.-G. Lee, S. Fujiki, C. Jung, B. Suzuki, N. Yashiro, R. Omada, D.-S. Ko, T. Shiratsuchi, T. Sugimoto, S. Ryu, J. H. Ku, T. Watanabe, Y. Park, Y. Aihara, D. Im, and I. T. Han. High-energy long-cycling all-solid-state lithium metal batteries enabled by silver-carbon composite anodes. *Nat. Energy*, 5:299–308, 2020.

[212] A. C. Kozen, C.-F. Lin, A. J. Pearse, M. A. Schroeder, X. Han, L. Hu, S.-B. Lee, G. W. Rubloff, and M. Noked. Next-generation lithium metal anode engineering via atomic layer deposition. *ACS Nano*, 9:5884–5892, 2015.

[213] X. Liang, Q. Pang, I. R. Kochetov, M. S. Sempere, H. Huang, X. Sun, and L. F. Nazar. A facile surface chemistry route to a stabilized lithium metal anode. *Nat. Energy*, 2:17119, 2017.

[214] R. wang, J. Yu, J. Tang, R. meng, L. F. Nazar, L. Huang, and X. Liang. Insights into dendrite suppression by alloys and the fabrication of a flexible alloy-polymer protected lithium metal anode. *Energy Storage Mater.*, 32:178–184, 2020.

[215] Q. Li, Q. Liu, X. Wang, Q. Wu, L. Fan, W. Zhang, Z. Shen, L. Wang, M. Ling, and Y. Lu. Constructing a phosphating-nitriding interface for practically used lithium metal anode. *ACS Mater. Lett.*, 2:1–8, 2020.

[216] N.W. Li, Y.-X. Yin, C.-P. Wang, and Y.-G. Guo. An artificial solid electrolyte interphase layer for stable lithium metal anodes. *Adv. Mater.*, 28:1853–1858, 2016.

[217] P. López-Aranguren, M. Reynaud, P. Głuchowski, A. Bustinza, M. Galceran, J. M. López del Amo, M. Armand, and M. Casas-Cabanas. Crystalline LiPON as a bulk-type solid electrolyte. *ACS Energy Lett.*, 6:445–450, 2021.

[218] Y. Zhu, X. He, and Y. Mo. Strategies based on nitride materials chemistry to stabilize Li metal anode. *Adv. Sci.*, 4:1600517, 2017.

[219] A. S. Westover, R. L. Sacci, and N. Dudney. Electroanalytical measurement of interphase formation at a Li metal-solid electrolyte interface. *ACS Energy Lett.*, 5:3860–3867, 2020.

[220] Z. D. Hood, X. Chen, R. L. Sacci, X. Liu, G. M. Veith, Y. Mo, N. Niu, N. J. Dudney, and M. Chi. Elucidating interfacial stability between lithium metal anode and Li phosphorus oxynitride via in situ electron microscopy. *Nano Lett.*, 21:151–157, 2021.

[221] N. J. Dudney. Thin film micro-batteries. *Electrochem. Soc. Interf.*, 17:44–48, 2008.

[222] B. Fleutot, B. Pecquenard, H. Martinez, M. Letellier, and A. Levasseur. Investigation of the local structure of LiPON thin films to better understand the role of nitrogen on their performance. *Solid State Ion.*, 186:29–36, 2011.

[223] S. Jacke, J. Song, L. Dimesso, J. Brötz, D. Becker, and W. Jaegermann. Temperature dependent phosphorous oxynitride growth for all-solid-state batteries. *J. Power Sources*, 196:6911–6914, 2011.

[224] A. C. Kazen, A. J. Pearse, C.-F. Lin, M. Noked, and G. W. Robloff. Atomic layer deposition of the solid electrolyte LiPON. *Chem. Mater.*, 27:5324–5331, 2015.

[225] X. Liang and L. F. Nazar. in-situ reactive assembly of scalable core-shell sulfurMnO_2 composite cathodes. *ACS Nano*, 10:4192–4198, 2016.

[226] Y. Kim, Y.Park, A. Choi, N.-S. Choi, J. Kim, J. Lee, J. H. Ryu, and K. T. Lee. An amorphous red phosphorus/carbon composite as a promising anode material for sodium ion batteries. *Adv. Mater.*, 25:3045–3049, 2013.

[227] T. Ramireddy, T. Xing, M. M. Rahman, Y. Chen, Q. Dutercq, D. Gunzelmanna, and A. M. Glushenkov. Phosphorus-carbon nanocomposite anodes for lithium-ion and sodium-ion batteries. *J. Mater. Chem. A*, 3(10):5572–5584, 2015.

[228] B. C. Bunker, D. R. Tallant, C. A. Balfe, R. J. Kirkpatrick, P. L. Turner, and M. R. Reidmeyer. Structure of phosphorus oxynitride glasses. *J. Am. Ceram. Soc.*, 70:675–681, 1987.

[229] T. Pichonat, C. Lethien, N. Tiereclin, S. Godey, E. Pichonat, P. Roussel, M. Colmont, and P. A. Rolland. Further studies on the lithium phosphorus oxynitride solid electrolyte. *Mater. Chem. Phys.*, 123:231–235, 2010.

[230] N. Mascaraque, A. Durán, F. Muñoz, and G. Tricot. Structural Features of LiPON Glasses Determined by 1D and 2D^{31}P MAS NMR. *Int. J. Appl. Glass Sci.*, 7:69–79, 2016.

[231] B. Fleutot, B. Pecquenard, H. Martinez, and A. Levasseur. Thorough study of the local structure of LiPON thin films to better understand the influence of a solder-reflow type thermal treatment on their performances. *Solid State Ion.*, 206:72–77, 2012.

[232] B. Wang, J. Liu, Q. Sun, R. Li, T.-K. Sham, and X. Sun. Atomic layer deposition of lithium phosphates as solid-state electrolytes for all-solid-state microbatteries. *Nanotechnology*, 25:504007, 2014.

[233] S. S. Zhang and J. A. Read. A new direction for the performance improvement of rechargeable lithium/sulfur batteries. *J. Power Sources*, 200:77–82, 2012.

[234] H. Tang, W. Li, L. Pan, C. P. Cullen, Y. Liu, A. Pakdel, D. Long, J. Yang, N. McEvoy, G. S. Duesberg, V. Nicolosi, and C. J. Zhang. in-situ formed protective barrier enabled by sulfur@titanium carbide (MXene) ink for achieving high-capacity, long lifetime Li-S batteries. *Adv. Sci.*, 5:1800502, 2018.

[235] X. Ge, C. Li, Z. Li, and L. Yin. Tannic acid tuned metal-organic framework as a high-efficiency chemical anchor of polysulfide for lithium-sulfur batteries. *Electrochim. Acta*, 281:700–709, 2018.

[236] T. Yang, K. Liu, R. Ren, J. Zhang, X. Zheng, C. Wang, and M. Chen. Uniform growth of Li_2S promoted by an organophosphorus-based mediator for high rate Li-S batteries. *Chem. Eng. J.*, 381:122685, 2020.

[237] Michael J. Wang, Eric Carmona, Arushi Gupta, Paul Albertus, and Jeff Sakamoto. Enabling "lithium-free" manufacturing of pure lithium metal solid-state batteries through in situ plating. *Nat. Commun*, 11, 2020.

[238] Yu Qiao, Kezhu Jiang, Han Deng, and Haoshen Zhou. A high-energy-density and long-life lithium-ion battery via reversible oxide-peroxide conversion. *Nat. Catal.*, 2:1035–1044, 2019.

[239] Y. Qiao, H. Deng, P. He, and H. Zhou. A 500 $W{\cdot}h{\cdot}kg^{-1}$ lithium-metal cell based on anionic redox. *Joule*, 4:1445–1458, 2020.